Universität Hamburg
DER FORSCHUNG | DER LEHRE | DER BILDUNG

Helmholtz-Zentrum hereon

Elemental mercury air–sea exchange - insights from long-term, ground-based atmospheric observations

Dissertation
zur Erlangung des Doktorgrades der Naturwissenschaften
an der Fakultät für Mathematik, Informatik und Naturwissenschaften
Fachbereich Geowissenschaften
der Universität Hamburg

vorgelegt von
Koketso Michelle Molepo
geboren am 16.09.1993 in Tzaneen, Südafrika

Hamburg, 2025

Fachbereich Geowissenschaften

Vorsitzender des
Fachpromotionsausschusses
Geowissenschaften: Prof. Dr. Hermann Held

Dekan der Fakultät MIN: Prof. Dr.-Ing. Norbert Ritter

Date of oral defense: 17.02.2026

Eidesstattliche Versicherung | Declaration on Oath

Hiermit erkläre ich an Eides statt, dass ich die vorliegende Dissertationsschrift selbst verfasst und keine anderen als die angegebenen Quellen und Hilfsmittel benutzt habe.

Sofern im Zuge der Erstellung der vorliegenden Dissertationsschrift generative Künstliche Intelligenz (gKI) basierte elektronische Hilfsmittel verwendet wurden, versichere ich, dass meine eigene Leistung im Vordergrund stand und dass eine vollständige Dokumentation aller verwendeten Hilfsmittel gemäß der Guten wissenschaftlichen Praxis vorliegt. Ich trage die Verantwortung für eventuell durch die gKI generierte fehlerhafte oder verzerrte Inhalte, fehlerhafte Referenzen, Verstöße gegen das Datenschutz- und Urheberrecht oder Plagiate.

I hereby declare and affirm that this doctoral dissertation is my own work and that I have not used any aids and sources other than those indicated.

If electronic resources based on generative artificial intelligence (gAI) were used in the course of writing this dissertation, I confirm that my own work was the main and value-adding contribution and that complete documentation of all resources used is available in accordance with good scientific practice. I am responsible for any erroneous or distorted content, incorrect references, violations of data protection and copyright law or plagiarism that may have been generated by the gAI.

Hamburg, 25.07.2025

Ort,den | City,date

Unterschrift | Signature

Abstract

Mercury (Hg) is a globally distributed pollutant due to the long atmospheric residence time of elemental mercury (Hg^0), which enables long-range transport before deposition to terrestrial and ocean surfaces. In the ocean, deposited Hg can be converted to monomethylmercury (MMHg), a highly toxic compound with severe implications for human and ecosystem health. Air–sea exchange of Hg^0 plays a pivotal role in the global Hg cycle by both supplying and removing the Hg in the ocean, thereby influencing the substrate available for methylation. Despite its significance, this exchange remains poorly constrained, due to a scarcity of direct observations and an incomplete understanding of the underlying mechanisms. This dissertation uses indirect observations, that is, ground-based atmospheric Hg^0 (Hg^0_{air}) measurements from long-term coastal monitoring sites to study Hg^0 air–sea exchange. These measurements, from Mace Head (Irish west coast), Cabo Verde Observatory (sub-tropical North Atlantic Ocean), Cape Point (southwestern tip of South Africa) and Amsterdam Island (remote Indian Ocean), are combined with back trajectory analyses as well as a diverse set of meteorological and oceanographic datasets to provide new constraints on Hg^0 air–sea exchange. Observed at all sites is a gradual increase in mean Hg^0_{air} concentration with time air masses recently spent in the Marine Boundary Layer (MBL), consistent with direct influence of ocean Hg^0 emissions. Based on this relationship, a new net global Hg^0 evasion flux of 2270 t y^{-1} (95 % confidence interval: 1600–2900 t y^{-1}) is derived, which is lower than current chemical transport model (CTM) estimates, suggesting that these models overestimate the flux. Despite evidence of ocean emissions, Hg^0_{air} concentrations at the sites exhibit weak seasonal and diurnal variability, contrasting expectations of strong environmental control by variables such as sea surface temperature (SST), wind speed and solar radiation. Unexpected negative Hg^0_{air}–SST correlations suggest that, while warmer waters may induce evasion on a local scale, the large-scale influence of SST may be minor or masked by competing processes associated with phytoplankton activity, for example Hg^0_{air} uptake and surfactant-driven evasion suppression, as well as hemispheric-scale terrestrial vegetation Hg^0_{air} uptake. Moreover, the phytoplankton-driven processes, which have been largely overlooked, may strongly influence mean interannual variability in Hg^0 air–sea exchange fluxes and resulting Hg^0_{air} concentrations in the MBL. Overall, this work demonstrates the value of long-term, ground-based Hg^0_{air} observations in constraining Hg^0 air–sea exchange and bridging knowledge gaps, while also

highlighting the need for extended measurements for a more comprehensive understanding of the global Hg cycle.

Kurzfassung

Quecksilber (Hg) ist ein weltweit verbreiteter Schadstoff, da es in elementarer Form (Hg^0) aufgrund seiner langen Verweildauer in der Atmosphäre über weite Strecken transportiert werden kann, bevor es sich auf Land- und Meeresoberflächen ablagert. Im Ozean abgelagertes Hg kann in Monomethylquecksilber (MMHg) umgewandelt werden, eine hochgiftige Verbindung, die die Gesundheit von Menschen und Ökosystemen erheblich beeinträchtigen kann. Der Austausch von Hg^0 zwischen Atmosphäre und Meer spielt eine zentrale Rolle im globalen Hg-Kreislauf, da er Hg sowohl dem Ozean zuführt als auch Hg aus dem Ozean entfernt und somit das für die Methylierung verfügbare Substrat direkt beeinflusst. Trotz seiner großen Bedeutung ist dieser Austausch nach wie vor nur unzureichend verstanden, was auf eine geringe Zahl direkter Beobachtungen und ein unvollständiges Verständnis der zugrunde liegenden Mechanismen zurückzuführen ist. Die vorliegende Dissertation nutzt indirekte Beobachtungen, das heißt bodengestützte Messungen von atmosphärischem Hg^0 (Hg^0_{air}) an Langzeitmessstationen, um den Hg^0-Austausch zwischen Atmosphäre und Meer zu untersuchen. Die in Mace Head (irische Westküste), dem Cabo Verde Observatory (subtropischer Nordatlantik), Cape Point (Südwestspitze Südafrikas) und Amsterdam Island (abgelegener Indischer Ozean) durchgeführten Messungen von Hg^0_{air} werden hierfür mit Rückwärtstrajektorien Analyse und einer Vielzahl meteorologischer und ozeanografischer Datensätze kombiniert, um neue Erkenntnisse über den Hg^0-Austausch zwischen Atmosphäre und Meer zu gewinnen. Hierbei wird an allen Messstationen ein allmählicher Anstieg der mittleren Hg^0_{air}-Konzentration festgestellt, in Abhängigkeit von der Zeit, die Luftmassen vor ihrer Ankunft in der marinen Grenzschicht (MBL) verbracht hatten, was auf einen direkten Einfluss ozeanischer Hg^0-Emissionen auf die gemessenen atmosphärischen Konzentrationen hinweist. Auf Grundlage dieser Beziehung wird ein neuer globaler Netto- Hg^0-Emissionsfluss aus dem Ozean in die Atmosphäre von 2270 t a^{-1} (95 %-Konfidenzintervall: 1600–2900 t a^{-1}) abgeleitet. Dieser Fluss liegt unter den Schätzungen aktueller chemischer Transportmodelle (CTM), was darauf hindeutet, dass diese den Austausch möglicherweise überschätzen. Trotz klarer Hinweise auf einen direkten Bezug zu ozeanischen Emissionen weisen die Hg^0_{air}-Konzentrationen an allen untersuchten Standorten eine schwache saisonale und diurnale Variabilität auf. Dies ist nicht im Einklang mit der bislang angenommenen starken Umweltkontrolle durch Parameter wie Meeresoberflächentemperatur (SST),

Windgeschwindigkeit und Sonneneinstrahlung. Unerwartete negative Korrelationen zwischen Hg^0_{air} und SST deuten darauf hin, dass wärmere Gewässer lokal zwar erhöhte Emissionen verursachen könnten, der überregionale Einfluss der SST jedoch gering ist. Eine weitere Erklärung ist, dass eine Beziehung zwischen Hg^0_{air} und der SST durch konkurrierende Prozesse, wie der Hg-Aufnahme durch Phytoplankton, eine durch Tenside bedingte Unterdrückung des Ozean-Atmosphäre-Austausches oder die großräumige Hg^0_{air}-Aufnahme von terrestrischer Vegetation, maskiert sein könnte. Darüber hinaus könnten die durch Phytoplankton gesteuerten Prozesse, die bislang weitgehend übersehen wurden, die mittlere interannuelle Variabilität der Hg^0-Austauschflüsse zwischen Atmosphäre und Ozean sowie die resultierenden Hg^0_{air}-Konzentrationen in der MBL stark beeinflussen. Insgesamt zeigt die vorliegende Arbeit den großen Wert langfristiger, bodengestützter Hg^0_{air}-Beobachtungen für die Abschätzung des Hg^0-Austauschs zwischen Atmosphäre und Ozean sowie für das Schließen bestehender Wissenslücken. Zugleich unterstreicht sie die Notwendigkeit weiterer Messungen für ein umfassenderes Verständnis des globalen Hg-Kreislaufs.

Table of contents

List of frequently used acronyms and abbreviations

Acronym/Abbreviation	Definition
CPBL	Continental Planetary Boundary Layer
CTM	Chemical Transport Model
DGM	Dissolved Gaseous Mercury (Hg^0_{aq} + DMHg)
DMHg	Dimethylmercury
GMOS	Global Mercury Observation System
Hg	Mercury
Hg^0	Gaseous Elemental Mercury
Hg^0_{air}	Atmospheric Gaseous Elemental Mercury (vs Hg^0 in seawater)
Hg^0_{aq}	Dissolved Gaseous Elemental Mercury (vs Hg^0 in the atmosphere)
Hg^{II}	Gaseous Oxidised Mercury
HYSPLIT	Hybrid Single-Particle Lagrangian Integrated Trajectory
LFT	Lower Free Troposphere
MBL	Marine Boundary Layer
MMHg	Monomethylmercury
NDVI	Normalised Difference Vegetation Index
NH	Northern Hemisphere
PBL	Planetary Boundary Layer
^{222}Rn	Radon
SH	Southern Hemisphere
SST	Sea Surface Temperature
TGM	Total Gaseous Mercury (Hg^0 + Hg^{II} in the atmosphere)

Chapter 1 – Introduction

1.1 Motivation

1.1.1 Mercury as a global pollutant

Mercury (Hg) is a naturally occurring element that is present in the Earth's crust and released into the environment by processes such as volcanic eruptions and rock weathering (Ariya et al., 2015; AMAP/UNEP 2018). For centuries, however, humans have exacerbated the release of Hg through activities such as mining and fossil-fuel combustion, perturbing its natural cycle (Sunderland and Mason, 2007; Amos et al., 2013; Lamborg et al., 2014; Zhang et al., 2014; Streets et al., 2017; Outridge et al., 2018; Li et al., 2020; Sonke et al., 2023). Due to its toxicity, atmospheric long-range transport and its persistence in the environment, Hg is now recognised globally as a pollutant of major concern (Ariya et al., 2015; AMAP/UNEP, 2018; Budnik and Castelyn, 2019; Al-Sulaiti et al., 2022; Basu et al., 2023). This recognition has led to international regulatory efforts, most notably the Minamata Convention on Mercury, which aim to reduce anthropogenic Hg emissions and mitigate the environmental and human health impacts of Hg pollution.

On a global scale, most of the Hg released into the environment is emitted to the atmosphere, with total emissions estimated at ~ 8000–12000 t y^{-1} (Horowitz et al., 2017; Outridge et al., 2018; Shah et al., 2021; Zhang et al., 2023). These emissions are primarily in the form of gaseous elemental Hg (Hg^0), which is highly volatile, sparingly soluble and relatively inert (Horowitz et al., 2017). As a result, Hg^0 has a long atmospheric residence time, estimated at around several months to a year (e.g., Horowitz et al., 2017; Saiz-Lopez et al., 2018; Shah et al., 2021; Zhang et al., 2023). Due to this long atmospheric lifetime, it is transported thousands of kilometres around the globe (Yin et al., 2018; Horowitz et al., 2017; Koenig et al., 2022), reaching even remote areas far from anthropogenic sources (Travnikov 2005; Durnford et al., 2010; Koenig et al., 2022).

While in the atmosphere Hg^0 is present in very low concentrations[1] and is not directly harmful (Holloway and Littlefield, 2011), some of it is gradually oxidised to divalent Hg (Hg^{II}), which is more soluble and readily deposited to terrestrial and aquatic surfaces (Horowitz et al., 2017; Shah et al., 2021). In aquatic environments, some of this Hg^{II} is converted to monomethylmercury (MMHg), a highly toxic compound (Driscoll et al., 2013; Lehnherr, 2014; Zilloux, 2015). Although, on a global scale, MMHg constitutes only a small fraction of the Hg in the aquatic environment (Mason and Fitzerald, 1993; Bowman et al., 2014), it bioaccumulates in aquatic organisms and biomagnifies, reaching very high concentrations in piscivorous fish and other high trophic level species (Díez, 2009; Driscol et al., 2013; Lehnherr, 2014; Zillioux, 2015). Humans are primarily exposed to MMHg through consumption of contaminated marine fish and other seafood (Mason et al., 2012; Driscoll et al., 2013; Zillioux, 2015; Al-Sulaiti et al., 2022). Once ingested, MMHg is absorbed into the bloodstream and readily crosses both the blood-brain and placental barriers (Díez, 2009; Zillioux, 2015; Al-Sulaiti et al., 2022), with major effects including neurotoxicity in adults and developmental toxicity in foetuses exposed during pregnancy (Díez, 2009; Zillioux, 2015).

The Minamata Bay[2] tragedy in Japan is perhaps the most striking example of the dangers of MMHg. Between 1951 and 1963, a chemical factory in the city of Minamata discharged substantial amounts of MMHg into the sea, resulting in severe poisoning among the local population who consumed contaminated fish and shellfish (Takeuchi et al., 1962; Díez, 2009; Zillioux, 2015). Thousands of residents developed a neurological syndrome, now referred to as Minamata disease, characterised by a range of symptoms including sensory disorders, paralysis, coma and even death (Takeuchi et al., 1962). This incident highlighted the severe consequences of environmental Hg contamination and was instrumental in raising global awareness about the need for stringent Hg regulation.

Another major issue concerning Hg is its persistence in the biosphere, driven by a continuous cycle of deposition and re-emission between the atmosphere and surface reservoirs. In terrestrial and aquatic environments, deposited Hg^{II} can be reduced back to Hg^0, which is then re-emitted to the atmosphere. Burial in subsurface soils and in ocean and lake sediments serves as the only long-term sink for Hg, but these processes take millennia (Cossa et al., 2011; Amos

[1] The global mean atmospheric Hg^0 concentration is in the range of 1–2 ng m^{-3} (e.g., Sprovieri et al., 2016).
[2] The Minamata Convention on Mercury was aptly named after Minamata, Japan.

et al., 2013 and references therein; AMAP/UNEP, 2018). As a result, "legacy emissions", with sources dating back to the Spanish colonial period (~ 1520–1850) and the North American Gold Rush (~1850–1920) (Amos et al., 2013; Outridge et al., 2018 and references therein), continue to influence present-day Hg concentrations.

Since the 1980s, various emission control measures have been gradually implemented to tackle Hg pollution, such as the ban of its usage in batteries and thermometers (e.g., US EPA, 1997; OECD, 1995). While these measures have led to declines in anthropogenic emissions in the developed world, emissions from some developing countries have increased (Zhang et al., 2016; Streets et al., 2011, 2017).

To address Hg pollution on a global scale, the Minamata Convention on Mercury was adopted in 2013 and entered into force in 2017. Signed by nearly 130 countries[3], the Convention aims to "protect human health and the environment from the adverse effects of mercury", and commits its member states to control, and where feasible, reduce their anthropogenic Hg emissions (https://minamataconvention.org/en; last access: June 2025). Moreover, to evaluate the effectiveness of emission reduction strategies and predict their environmental impacts, the Convention stresses the need for research and monitoring of Hg, and calls for an improved understanding of the global Hg biogeochemical cycle (Outridge et al., 2018).

The global Hg cycle is complex, involving an intricate set of physical, chemical and biological processes, where Hg is converted between various forms and exchanged between different environmental compartments until it is eventually removed by burial in sediments and subsurface soils (see for instance Hg cycling in the marine environment in Figure 1). In response to the call for improved understanding, this dissertation investigates Hg^0 air–sea exchange, a crucial component of global Hg cycling that remains poorly constrained due to limited observational data.

1.1.2 Hg^0 air–sea exchange, and its role in global Hg cycling

Hg^0 air–sea exchange refers to the bidirectional transfer of this gas between the atmosphere and the surface ocean (Figure 1). It involves Hg^0 emission (that is, evasion) to the atmosphere

[3] 128 countries, as of June 2025 (https://minamataconvention.org/en/parties; last access: June 2025).

and dry deposition[4] (i.e., invasion, or ocean uptake) to the surface ocean. This exchange plays a pivotal role in the transport, turnover and fate of Hg in the environment.

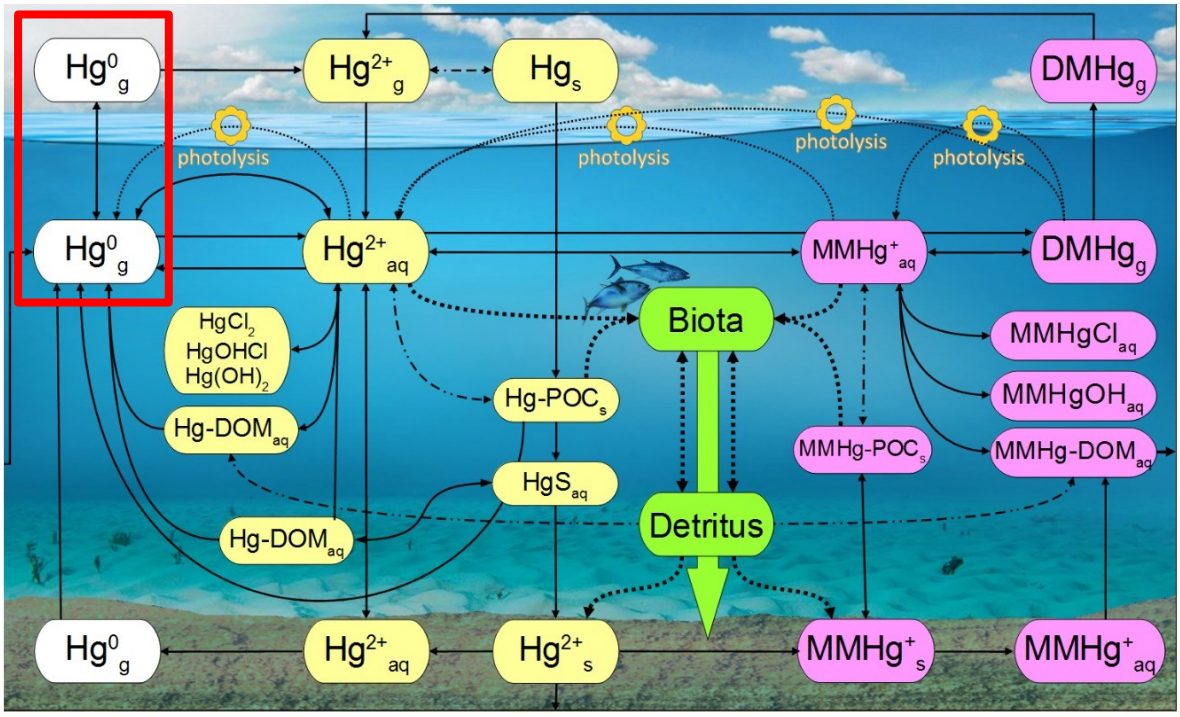

Figure 1: Conceptual model of Hg biogeochemical cycling in the marine environment, illustrating the complex processes and interconversions involved. Solid lines represent chemical reactions, fine dotted lines photolytic reactions, dash-dotted lines instantaneous partitioning whereas bold dotted lines indicate bioaccumulation and releases from biota into the dissolved phase. Different Hg forms are distinguished by colour coding: white for elemental, yellow for inorganic oxidised, pink for methylated and green for biotic, and species are labelled according to phase: "g" for gas, "aq" for dissolved and "s" for solid. Hg^0 air–sea exchange, the focus of this dissertation, is denoted by the red box. (Adaptation from Bieser et al. (2023), under CC BY 4.0; https://creativecommons.org/licenses/by/4.0/).

On a global scale, most of the Hg (Hg^0, as well as Hg^{II}, which in the atmosphere can originate from Hg^0 oxidation) entering the ocean derives from atmospheric deposition (Strode et al., 2007; Mason et al., 2012; Horowitz et al., 2017; Shah et al., 2021; Zhang et al., 2023). As such,

[4] As opposed to wet deposition, where Hg is dissolved in water droplets and removed from the atmosphere via precipitation, dry deposition involves direct transfer from the atmosphere to the surface without precipitation, driven by diffusion. Due to its low solubility and high volatility, Hg^0 is largely not involved in wet deposition.

atmospheric deposition significantly influences the distribution of marine Hg (Strode et al., 2007). At the same time, aqueous Hg^{II} can be reduced (back) to Hg^0, which is (re-)emitted to the atmosphere. Through this deposition–re-emission cycle, ocean emissions contribute to the long-range transport of Hg and to its persistence in the environment (Hedgecock and Pirrone, 2004; Strode et al., 2007; Amos et al., 2013). On the other hand, reduction of aqueous Hg^{II} to Hg^0 and its subsequent evasion decreases the Hg^{II} available for methylation (i.e., conversion to MMHg) and its eventual bioaccumulation in marine biota.

1.1.3 Challenges in accurately characterising Hg^0 air–sea exchange, and the importance of long-term monitoring

Despite its significant role in the global Hg biogeochemical cycle, Hg^0 air–sea exchange remains poorly constrained, due to a scarcity in direct observations and, in turn, an incomplete understanding of the mechanisms driving this process. Most of our knowledge on Hg^0 air–sea exchange stems from short-term, ship-based measurements performed during sampling campaigns (see Table 3 and Table 4 in Chapter 3, for example). While these measurements are immensely valuable, they only provide snapshots in time. Moreover, most sampling campaigns have been conducted in the northern hemisphere, with a critical lack of data from the southern hemisphere (see, for instance, Figure 7 in Dastoor et al., 2025). Global (e.g., Soerensen et al., 2010a; Tang et al., 2023) and semi-global[5] (e.g., Temme et al., 2003; Kuss et al., 2011) campaigns offer a wider spatial coverage, but these are rare, and they also suffer the limitation of only a few measurements made over each sampled location.

The global ocean is highly dynamic, with large spatio–temporal variability in parameters such as turbulence, sea surface temperature, biological activity, presence of sea ice and water mass mixing. These factors influence Hg^0 air–sea exchange, leading to a high variability in fluxes (see discussion on how these factors potentially influence air–sea Hg^0 exchange in Section 2.2, Chapter 2). Accurately capturing this variability and making reliable large-scale estimates requires continuous, long-term measurements. Yet, most direct measurements[6] to date span only a few days to a few weeks, requiring aggregation of data from different campaigns to infer large-scale patterns (e.g., Soerensen et al., 2012). However, measurements from different

[5] This is referring to sampling campaigns covering a wide ocean basin, for instance, both the North and South Atlantic oceans.
[6] That is, in situ flux as well as atmospheric and aqueous Hg^0 concentration measurements, along with relevant meteorological and oceanic variables, needed to examine Hg^0 dynamics at the air–sea interface.

campaigns are conducted with non-uniform standard operating procedures (Slemr et al., 2015), which limits comparability and hampers efforts to combine the datasets. Currently, there is no systematic monitoring of Hg^0 air–sea exchange fluxes (Dastoor et al., 2025), and this lack of repeated, long-term observations remains a major barrier for fully characterising Hg^0 air–sea exchange.

Chemical transport models (CTMs) help bridge the spatio–temporal gaps in observational data, barring computational limits. However, the accuracy of these models is also reliant on empirical input, for example the Hg^0 air–sea transfer velocity (see discussion in Section 2.3.2, Chapter 2), which remains a major source of uncertainty in model-based global flux estimates (Zhang et al., 2019). Models also require observational data for validation, which are sparse.

Due to these limitations in direct measurements, global Hg^0 air–sea exchange flux estimates remain highly uncertain, with recent model-based estimates of net global Hg^0 evasion flux ranging from 2800 to 4000 Hg^0 t y^{-1} (Horowitz et al., 2017; Shah et al., 2021; Zhang et al., 2023). The scarcity of observations has also limited our understanding of how different environmental parameters influence Hg^0 air–sea exchange on large temporal and spatial scales. These gaps hamper efforts to fully characterise the global Hg biogeochemical cycle and to predict Hg budgets, for instance, assessing the extent to which evasion reduces the Hg^{II} substrate for methylation, or how oceanic Hg levels respond to declining anthropogenic emissions under the Minamata Convention (Mason et al., 2012; Soerensen et al., 2013; Jiskra et al., 2021).

Long-term monitoring of atmospheric Hg^0 from ground-based sites has been instrumental in advancing our understanding of the global Hg cycle. Continuous records spanning months to decades, such as those from GMOS (Sprovieri et al., 2010, 2016) or AMNET[7] (Lan et al., 2012; Gay, 2013), have been widely used to discern Hg sources, sinks, transport pathways and spatio–temporal patterns in the terrestrial environment and the free troposphere (e.g., Sprovieri et al., 2010, 2016; Angot et al., 2014, Jiskra et al., 2018; Koenig et al., 2021, 2022, 2023). These measurements have also been applied to understand long-term trends (e.g., Marumoto et al., 2019; Custódio et al., 2022; Feng et al., 2024) and derive fluxes (e.g., Slemr et al., 2013) related to terrestrial–atmosphere interactions, contributing to knowledge on global Hg cycling.

[7] GMOS: Global Mercury Observation System; AMNET: (North American) Atmospheric Monitoring Network.

Of these ground-based sites, some stations sample predominantly marine air masses. In this way, they provide a valuable opportunity to study Hg^0 dynamics at the air–sea interface and constrain exchange processes. Moreover, their extended datasets enable analysis of atmospheric Hg^0 variability in the Marine Boundary Layer (MBL) across different temporal scales, offering insights into different environmental controls on concentrations and, consequently, on exchange fluxes. Despite their potential, very few studies (e.g., Carbone et al., 2016; Bieser et al., 2020) have leveraged these long-term datasets for comprehensive analyses of Hg^0 air–sea exchange.

1.2 Research goals

The main aim of this dissertation is to improve understanding of Hg^0 air–sea exchange using long-term, ground-based atmospheric Hg^0 observations. Measurements from four marine sites are applied in the original research studies: Mace Head on the west coast of Ireland, Cabo Verde Observatory in the subtropical North Atlantic, Cape Point on the southwestern tip of South Africa and Amsterdam Island in the remote Indian Ocean (see Figure 3 in Chapter 3 for the locations of the sites). With these datasets, the objectives are to:

i. Assess the influence of Hg^0 air–sea exchange on observed atmospheric Hg^0 concentrations.
ii. Constrain the net global Hg^0 air–sea exchange flux.
iii. Understand the influence of different environmental drivers on Hg^0 air–sea exchange.

It is important to note here that this work does not propose ground-based Hg^0 measurements as a substitute for direct observations at the air–sea interface. Rather, the goal is to gain new, additional insights from extended records; insights that may not be accessible with (direct) measurements from short-term sampling campaigns.

1.3 Document structure

The dissertation consists of five chapters. Following this Introduction:

- Chapter 2 presents scientific background on Hg^0 air–sea exchange, while also highlighting existing gaps and uncertainties in current knowledge. In doing so, the chapter contextualises the importance of the research presented in Chapters 3 and 4.
- Chapters 3 and 4 present each a stand-alone chapter of original research led by the Ph.D. candidate.
- Chapter 5 summarises the key findings of the dissertation, discusses their implications for global Hg cycling, and provides an outlook for future research.

Chapter 2 – Background

This chapter provides the scientific background necessary to understand Hg^0 air–sea exchange, its role in the global Hg biogeochemical cycle and the environmental parameters that govern this process. It also highlights existing gaps and uncertainties in current knowledge. Section 2.1 introduces the primary Hg species in the atmosphere and the oceans, along with their sources and transformations. While the focus of the dissertation is Hg^0, it is essential to introduce all major forms of Hg in the two compartments, as they are connected through interconversion, and most importantly, are all linked to the toxic MMHg (Figure 1).

2.1 Hg in the atmosphere and the oceans: sources, species, transformations and exchange

2.1.1 Hg in the atmosphere

In the atmosphere, Hg originates from both natural as well as anthropogenic sources. Natural sources include emissions from volcanic eruptions, wildfires, marine and fresh aquatic environments, soils, vegetation and geothermal activity (Ariya et al., 2015; AMAP/UNEP 2018). Anthropogenic emissions emanate from activities such as artisanal and small-scale gold mining, fossil-fuel combustion, steel production, metal smelting, cement production and waste incineration (Ariya et al., 2015; AMAP/UNEP 2018). Although both types contribute to the atmospheric Hg load, anthropogenic emissions have driven a ~ 5.5–7.6-fold increase in atmospheric Hg levels relative to pre-industrial concentrations (Amos et al., 2013; Zhang et al., 2014).

Atmospheric Hg exists in three main forms (or species), which differ in their physicochemical properties: gaseous elemental mercury (Hg^0 or GEM), gaseous oxidised mercury (Hg^{II} or GOM; also denoted reactive gaseous mercury, RGM) and particle-bound mercury (Hg_p or PBM).

Hg^0

Hg^0 is a monatomic gas and the dominant atmospheric Hg species, comprising over 98 % of the total atmospheric Hg load (e.g., Yin et al., 2018; Wang et al., 2019; Horowitz et al., 2017). It is the primary Hg form in both natural and anthropogenic emissions (Horowitz et al., 2017;

Streets et al., 2017). Due to its high volatility, low water solubility and low chemical reactivity, Hg^0 is largely unaffected by wet deposition (Horowitz et al., 2017), enabling it a relatively long atmospheric residence time (~ several months up to a year; Horowitz et al., 2017; Saiz-Lopez et al., 2018; Shah et al., 2021). Removal of Hg^0 from the atmosphere is mainly through dry deposition to land and ocean surfaces[8] (Horowitz et al., 2017; Jiskra et al., 2021; Zhou and Obrist, 2021; Feinberg et al., 2022; Zhang et al., 2023), as well as oxidation to Hg^{II}, with atomic bromine (Br) and hydroxyl radicals (OH) thought to be the dominant oxidants (e.g., Horowitz et al., 2017; Shah et al., 2021; Castro et al., 2022).

Hg^{II}

This species comprises various gaseous oxidised divalent Hg compounds derived primarily from anthropogenic emissions[9] as well as oxidation of Hg^0 in the atmosphere. The exact speciation of atmospheric Hg^{II} is unclear (Hedgecock and Pirrone, 2001; Shah et al., 2021), although gas-phase $HgCl_2$ and aqueous-phase Hg-chloride complexes are believed to be the primary species (e.g., Shah et al., 2021). Unlike Hg^0, Hg^{II} is more water soluble and efficiently removed from the atmosphere by wet and dry deposition (although it can also be reduced back to Hg^0; Holmes et al., 2010; Horowitz et al., 2017; Shah et al., 2021). As such, compared to Hg^0, Hg^{II} has a much shorter atmospheric residence time, ranging from hours to days (Hedgecock and Pirrone, 2001; Driscoll et al., 2013; Horowitz et al., 2017; Yin et al., 2018), and tends to be deposited locally or regionally (Hedgecock and Pirrone, 2001; Driscoll et al., 2013).

Hg_p

Hg_p consists of Hg adsorbed onto solid and/or liquid particles in the atmosphere. These particles can be chemically or physically homogeneous or heterogeneous (Ariya et al., 2015), with sizes ranging from submicrometres to a few micrometres (Ariya et al., 2015). In addition to direct emissions[9], Hg_p can also form in situ when the gaseous Hg species (Hg^{II} mainly) adhere to suspended particles in the atmosphere (Styszko et al., 2015; Das et al., 2016; Lyman et al., 2020). As with Hg^{II}, Hg_p has a relatively short atmospheric residence time (hours to days) and is locally or regionally deposited (Driscoll et al., 2013; Yin et al., 2018).

[8] Dry deposition to land surfaces occurs primarily via vegetation uptake, with recent estimates of the vegetation sink at around 2300 Hg^0 t y^{-1} (Zhou and Obrist, 2021; Feinberg et al., 2022). The global ocean is considered a net source of Hg^0 to the atmosphere; nevertheless, gross estimates of ocean Hg^0 uptake are in the range of 1700–3300 Hg^0 t y^{-1} (Horowitz et al., 2017; Shah et al., 2019; Zhang et al., 2023).

[9] While atmospheric Hg^{II} and Hg_p are primarily emitted from anthropogenic sources, natural sources such as volcanic eruptions and wildfires also contribute to their presence in the atmosphere (Pyle and Mather, 2003; Friedli et al., 2009).

In the atmospheric reservoir, the sum of Hg^0 and Hg^{II} is referred to as total gaseous mercury (TGM), that of Hg^{II} and Hg_p as reactive mercury (RM), and that of all three species as total mercury (TM).

Recent estimates place the global total tropospheric Hg burden at around 3800–4000 t (e.g., Horowitz et al., 2017; Shah et al., 2021; Zhang et al., 2023), with annual emissions to the atmosphere estimated at roughly 8000–12000 t y^{-1} (Horowitz et al., 2017; Outridge et al., 2018; Shah et al., 2021; Zhang et al., 2023). While the exact contribution from different sources is highly uncertain, net annual oceanic Hg^0 emissions are thought to make up about one-third of the global total, similar in magnitude to primary anthropogenic emissions (Horowitz et al., 2017; Outridge et al., 2018; Shah et al., 2021; Zhang et al., 2023). This highlights the importance of ocean Hg^0 emissions in sustaining the atmospheric Hg reservoir, the main pathway for global Hg distribution, and the need for accurate estimates of these emissions in global Hg budgets.

2.1.2 Hg in the ocean

The majority of Hg entering the ocean is derived from atmospheric deposition (Strode et al., 2007; Sunderland and Mason, 2007; Soerensen et al., 2010b; Mason et al., 2012; Horowitz et al., 2017; Shah et al., 2021). This input includes both wet and dry deposition of Hg^{II}, as well as dry deposition of Hg^0. Earlier studies suggested that Hg^{II} deposition dominates, with contributions in the ratio of (Hg^0:Hg^{II}) 1:2.7 (Horowitz et al., 2017)[10] to 1:2.0 (Shah et al., 2019)[11], whereas more recent work suggests a larger contribution from Hg^0 invasion, with ratios of 1:1.5 (Zhang et al., 2023)[12] and even 1:1 (Jiskra et al., 2021)[13]. Riverine discharge, groundwater, underwater volcanoes, mid-ocean ridges and hydrothermal vents also contribute to marine Hg, but their global-scale input is minor compared to atmospheric deposition (Mason et al., 2012; AMAP/UNEP, 2018; Torres-Rodriguez et al., 2024).

[10] Horowitz et al. (2017): Model-estimated gross atmospheric deposition to the ocean: 1700 t y^{-1} Hg^0 and 4600 ty^{-1} Hg^{II}.
[11] Shah et al. (2019): Model-estimated gross atmospheric deposition ocean: 2000 t y^{-1} Hg^0 and 3900 ty^{-1} Hg^{II}.
[12] Zhang et al. (2023): Model-estimated estimated gross atmospheric deposition to the ocean: 3270 t y^{-1} Hg^0 and 4860 ty^{-1} Hg^{II}.
[13] Jiskra et al. (2021): Constraint based on marine Hg stable isotope observations.

In seawater, Hg is present in four main chemical species, which interconvert via complex biotic and abiotic processes: monomethylmercury (MMHg), dimethylmercury (DMHg), aqueous divalent mercury (or mercuric ion; Hg^{II}) as well as dissolved gaseous elemental mercury (Hg^0) (Strode et al., 2007; Kotnik et al., 2007; Bowman et al., 2014; Lamborg et al., 2014).

MMHg

MMHg is an organo-metallic compound produced primarily through microbial methylation of dissolved Hg^{II} in sediments and deep anoxic waters (Mason and Fitzgerald, 1993; Zillioux, 2015 and references therein; Lehnherr, 2014 and references therein; Baumann et al., 2019; Al-Sulaiti et al., 2022). In surface waters, MMHg is mainly derived from diffusion and upwelling from deeper water (Mason and Fitzgerald, 1993; Adams et al., 2024). Due to its toxicity and capability for bioaccumulation and biomagnification, MMHg is the Hg species of greatest concern.

DMHg

DMHg, which is a gas, is thought to form from degradation of MMHg (Soerensen et al., 2016), although microbial methylation of Hg^{II} is also considered to be a formation pathway (Baumann et al., 2019). In surface waters, DMHg readily evaporates to the atmosphere (Soerensen et al. 2016), where it quickly degrades (in the presence of sunlight) to MMHg and is deposited back to the ocean (Mason et al., 1995; Soerensen et al., 2016; Nerentorp Mastromonaco et al., 2017). Unlike MMHg, DMHg is not believed to bioaccumulate (Mason et al., 1996; Baumann et al., 2019).

Hg^{II}

Apart from atmospheric deposition, aqueous Hg^{II} is derived from microbial and abiotic (photochemical) demethylation of MMHg (Mason and Fitzerald, 1993; Lehnherr, 2014 and references therein). Hg^{II} is the principal substrate for both methylation and reduction reactions in marine waters.

Hg^0

In addition to dry deposition, Hg^0 in seawater originates from both biotic and photochemical conversion of aqueous Hg^{II} as well as MMHg (Kim et al., 2016; Lee and Fisher et al., 2018). Due to its low solubility, Hg^0 readily evades (back) to the atmosphere, although some may be

(re)oxidised to Hg^{II} or bind to suspended particulate matter (Wang et al., 2015). This reduction of Hg^{II} to Hg^0 and its subsequent evasion lowers the pool of Hg^{II} available for methylation to MMHg. Along with DMHg, Hg^0 constitutes the operationally defined dissolved gaseous mercury (DGM). Except in upwelling regions (Adams et al., 2024), DGM in surface waters comprises primarily of Hg^0, with very negligible contributions from DMHg, which is found mainly in deeper waters (Mason and Fitzerald, 1993; Horvat et al., 2003; Kotnik et al., 2007; Cossa et al., 2011; Bowman et al., 2015, 2016; Bratkič et al., 2016).

As with the atmospheric reservoir, Hg concentrations in the ocean have been drastically elevated by human activities. For example, Outridge et al. (2018) estimated that anthropogenic increases to the atmospheric Hg load[14] have resulted in a 4-fold increase in atmospheric deposition rates, which has in turn increased marine surface water Hg concentrations an average 3.3-fold. A similar estimate, 3.5-fold increase in surface water concentrations due to anthropogenic activities, was derived by Lamborg et al. (2014) using direct oceanographic measurements.

2.2. Factors that influence Hg^0 air–sea exchange

While the factors that govern Hg^0 air–sea exchange are complex and not fully understood, several parameters have been identified as key drivers. This section summarises these drivers, namely, the air–sea Hg^0 concentration gradient, surface wind speed, solar radiation, sea surface temperature (SST) and microbial activity.

2.2.1 Hg^0 concentration gradient and seawater Hg^0 saturation

Hg^0 air–sea exchange occurs by diffusion. As such, the direction and magnitude of net exchange is strongly dependent on the Hg^0 concentration gradient across the air–sea interface, normalised by the Henry's law constant (Zhang et al., 2019). This gradient is expressed as a degree of saturation of surface seawater (relative to the overlaying air), *S* (in %), calculated as:

$$S = \left(\frac{Hg^0{}_{aq} \times H'}{Hg^0{}_{air}} \right) \times 100, \qquad (2.1)$$

[14] Referring to a 5.5-fold increase in the atmospheric Hg load relative to natural levels.

where Hg^0_{aq} and Hg^0_{air} are the Hg^0 concentrations in surface seawater and air, respectively, and H' is the dimensionless Henry's law constant. Alternatively, S is derived from:

$$S = \left(\frac{Hg^0_{eq}}{Hg^0_{air}}\right) \times 100, \quad (2.2)$$

where Hg^0_{eq} is the surface seawater Hg^0 concentration at equilibrium with the overlaying air. The Henry's law constant represents the equilibrium partitioning of Hg^0 between water and air and is defined as the equilibrium vapour pressure over the molar fraction in water (Gårdfeldt et al., 2003; Ariya et al., 2015). It varies with salinity and water temperature and typically decreases with increasing salinity and temperature (Andersson et al., 2008a). Various parameterisations have been derived to represent H', with the most commonly applied formulation (in Hg^0 air–sea exchange research) being that from Andersson et al. (2008a)[15], which uses SST:

$$H' = e^{\left(\frac{-2404.3}{T} + 6.92\right)}, \quad (2.3)$$

where T is the SST.

When surface seawater is supersaturated ($S > 100$ %), evasion may occur; when it is undersaturated ($S < 100$ %), invasion may take place. In situ measurements suggest that surface oceans are largely supersaturated in Hg^0 relative to the atmosphere (e.g., Andersson et al., 2008c; Wängberg et al., 2001; Gårdfeldt et al., 2003; Wang et al., 2017; Wang et al., 2019; Lamborg et al., 2021; Osterwalder et al., 2021), and hence, on a global scale, net Hg^0 exchange is to the atmosphere.

However, supersaturation does not necessarily mean (high rates of) evasion. The rate of exchange (in either direction) is also strongly dependent on sea surface conditions, such as

[15] The Henry's law derivation from Andersson et al. (2008a) has been widely used in Hg^0 air–sea exchange studies, including by Kuss et al. (2011); Tseng et al. (2012); Soerensen et al. (2014); Nerentorp Mastromonaco et al. (2017); Wang et al. (2017); Zhang et al. (2019); Chen et al. (2020); Li et al. (2024) and many others.

wind-driven turbulence, and is also affected by the presence of surfactants in the sea surface microlayer (Li et al., 2024) or sea ice (Andersson et al., 2008b; DiMento et al., 2019).

2.2.2 Surface wind speed

Surface wind speed, as noted above, is a critical driver of air–sea gas exchange. Strong winds generate turbulence, enhancing breaking waves that form bubbles. Bubbles facilitate gas exchange by increasing the effective surface area at the air–sea interface (Wanninkhof et al., 2009). Moreover, strong winds promote vertical mixing between surface and subsurface waters, which can replenish surface Hg^{II}, providing additional substrate for reduction to Hg^0 (Soerensen et al., 2010b, 2013; Floreani et al., 2019).

As the primary driver of turbulence in the upper ocean (Li et al., 2024), wind speed is widely used to parameterise air–sea gas transfer velocity (e.g., Liss and Merlivat, 1986; Wanninkhof 1992; Wanninkhof and McGillis, 1999; Nightingale et al., 2000; McGillis et al., 2001). This wind-speed-based parameterisation of the air–sea gas transfer velocity is discussed further in Section 2.3 in this chapter, which reviews approaches used to estimate air–sea Hg^0 exchange fluxes.

2.2.3 Solar radiation

Solar radiation drives the abiotic conversion of Hg^{II} to Hg^0 (e.g., Kim et al., 2016). However, the scale at which Hg^0 photoproduction is relevant is unclear. Coastal and near coastal in situ studies report distinct diurnal cycles in DGM concentrations and evasion fluxes that correlate to solar radiation (e.g., Lanzillotta and Ferrara, 2001; Gårdfeldt et al., 2003; Andersson et al., 2007; Floreani et al., 2019), whereas observations of atmospheric Hg^0 concentration over the open ocean show no significant diurnal patterns (e.g., Soerensen et al., 2010a; Wang et al., 2017; Wang et al., 2019).

2.2.4 Microbial activity

Microbial activity influences Hg^0 air–sea exchange through several complex and potentially contrasting mechanisms. As already highlighted, microbial activity contributes to reduction of

Hg^{II} to Hg^0 (Grégoire and Poulain, 2014 and references therein; Kim et al., 2016; Lee and Fisher 2018; Liang et al., 2022), which would promote evasion. Conversely, recent experimental work suggests that phytoplankton may also sequester atmospheric Hg^0, acting as a sink (Santos et al., 2024). In addition, surface-active organic matter (surfactants), primarily derived from phytoplankton exudates and degradation products, accumulate in the sea surface microlayer, where they form a physico–chemical barrier and alter sea surface turbulence and wave dynamics, the effects of which can suppress air–sea gas exchange (Tsai and Liu 2003; Pereira et al., 2018; Li et al., 2024). Overall, the net influence of ocean primary productivity on Hg^0 air–sea exchange is unclear.

2.2.5 SST

SST influences Hg^0 air–sea exchange in three main ways, all of which promote evasion. Warmer waters (i) increase the diffusivity of Hg^0 in seawater, (ii) decrease its solubility and (iii) stimulate the microbial conversion of Hg^{II} (as well MMHg) to Hg^0 (Mason et al., 1993; Soerensen et al., 2013; Lee and Fisher, 2018).

Taken together, these factors underscore the complexity of Hg^0 air–sea exchange. Laboratory and field experiments help isolate specific mechanisms and understand their individual influence, but their impact at large spatial and temporal scales in the natural environment is unclear. Moreover, some of these processes respond similarly to environmental controls (such as radiation, which, itself also influences air–sea exchange) but exert opposing effects (e.g., production vs sequestration of Hg^0 by phytoplankton), potentially masking or even cancelling each other out. As such, understanding the net effects of these processes remains a key challenge in quantifying Hg^0 air–sea exchange on a large scale.

2.3 Estimation of the Hg^0 air–sea exchange fluxes

A crucial step towards a comprehensive understanding of the global Hg cycling is accurately quantifying the fluxes between different environmental compartments. For Hg^0 air–sea

exchange, two main approaches[16] are widely applied, (i) (dynamic) flux chamber techniques and (ii) the gas exchange model, each with its own advantages and disadvantages.

2.3.1 Flux chamber technique

The flux chamber technique is a relatively simple method for directly measuring Hg^0 air–sea exchange fluxes. As described by previous studies, Bagnato et al. (2013) and Floreani et al. (2019), for instance, measurements are performed on a small, floating rectangular chamber, typically made of plexiglass. The chamber is open at the bottom and closed at the top, allowing diffusion of Hg^0 from the confined sea surface, and submerged into the sea about halfway along its length, preventing entry of outside air. External air, of which the Hg^0 concentration is first measured, flows into the chamber via an inlet at a controlled flow rate. Fans installed in the chamber allow the air inside to homogenise. Air then flows out of the chamber via an outlet and its Hg^0 concentration is measured. The Hg^0 air–sea exchange flux, F, is then calculated as:

$$F = \frac{Q \times (C_o - C_i)}{A}, \qquad (2.4)$$

where C_o and Ci are the Hg^0 concentrations of the air exiting and entering the chamber, respectively, Q is the flow rate of air through the chamber and A is sea surface area covered by the chamber, that is, the surface area of the bottom of the chamber.

This technique is commonly applied in coastal waters (e.g., Gårdfeldt et al., 2003; Bagnato et al., 2013; Floreani et al., 2019), but has also been adapted for the open ocean, during ship-board sampling campaigns, where the incoming air has to be filtered to eliminate the impact of shipborne Hg emissions (e.g., Kalinchuk et al., 2021, 2023).

While the flux chamber technique is relatively simple, a major drawback is that it creates a microenvironment, altering gas exchange and environmental conditions (such as incident solar radiation and wind speed), which may bias fluxes estimates (Wängberg et al., 2001; Andersson et al., 2007). However, it is suggested that the relatively short sampling times (typically 10 mins or less; e.g, Gårdfeldt et al., 2003; Bagnato et al., 2013; Floreani et al., 2023) minimise

[16] Other methods exist, such as micro-meteorological techniques (e.g., Osterwalder et al., 2021); however, these methods have not been extensively applied for Hg^0 air–sea exchange. Therefore, these other methods have been omitted from the discussion.

the effects on the environmental conditions. This, on the other hand, makes the technique rather tedious, as the chamber needs frequent redeployment. Another disadvantage with this method is that it can only be performed under calm conditions, such as low wind speed, absence of waves and low humidity (Gårdfeldt et al., 2003; Bagnato et al., 2013; Floreani et al., 2019), making it difficult to assess their influence on measured Hg^0 air–sea fluxes (Wängberg et al., 2001).

2.3.2 Gas exchange model

The gas exchange model (also referred to as the thin film gas exchange model) is widely used in both field studies and Chemical transport models (CTMs) to estimate Hg^0 air–sea exchange fluxes. The model calculates the flux based on the Hg^0 concentration gradient across the air–sea interface as well as environmental parameters such as wind speed and SST. The flux, F, is expressed as:

$$F = k_w \left(Hg^0{}_{aq} - \frac{Hg^0{}_{air}}{H'} \right), \quad (2.5)$$

where k_w is the gas transfer velocity, parameterised as a function of surface wind speed, Hg^0_{aq} and Hg^0_{air} are the Hg^0 concentrations in surface seawater and in air, respectively, and H' is the dimensionless Henry's law constant, typically parametrised as a function of SST (as described in Section 2.2.1).

Currently, there is a lack of direct measurements of Hg^0 transfer velocity, which is a major source of uncertainty for global-scale flux estimates (Zhang et al., 2019; Osterwalder et al., 2021; Li et al., 2024). Only one known study, Osterwalder et al. (2021), has derived the transfer velocity from direct Hg^0 measurements, using micro-meteorological methods. Even then, the derivation is based on a very small sample (see Figure 2). Parameterisations of k_w applied in Hg^0 air–sea exchange models are based on in situ measurements of other trace gases, such as CO_2 and dimethyl sulfide (e.g., Wanninkhof, 1992; McGillis et al., 2001; Nightingale et al., 2000). The parameterisations use wind speed, the primary driver of turbulence, in either linear, quadratic or cubic form (see Table 1). Widely used k_w formulations in Hg^0 air–sea exchange research include those from Liss and Merlivat (1986), Wanninkhof (1992), Wanninkhof and McGillis (1999), Nightingale et al. (2000) and McGillis et al. (2001) (Table 1), with the

formulation from Nightingale et al. (2000) being the most preferred (e.g., Andersson et al., 2007, 2008b; Kuss et al., 2011; Soerensen et al., 2010b, 2013; Mason et al., 2017; Zhang et al., 2019; Li et al., 2024).

However, gases of different solubility respond differently to the processes that drive fluxes, which makes it problematic to apply a single wind speed function for all gases (Osterwalder et al., 2021). Moreover, comparison of the various k_w parameterisations shows considerable variability in estimated fluxes, with the differences especially large at high wind speeds (see Figure 2). As such, current global Hg^0 flux estimates from CTMs (2800–4000 Hg^0 t y^{-1} net global evasion; Horowitz et al., 2017; Shah et al., 2021; Zhang et al., 2023) are highly sensitive to the k_w parametrisation applied.

Table 1: The most commonly applied paramerisations for k_w, the gas transfer velocity. In the table, U_{10} is 10 m wind speed, while Sc_{Hg} and Sc_{CO2} are the Schmidt numbers[17] of elemental Hg and CO_2, respectively.

Parameterisation scheme	Equation
Liss and Merlivat (1986)	$U10 < 3.6$ m s^{-1}: $0.17U_{10}(Sc_{Hg}/Sc_{CO2})^{-0.67}$
	3.6 m $s^{-1} < U10 < 13$ m s^{-1}: $(2.8U_{10} - 9.6)(Sc_{Hg}/Sc_{CO2})^{-0.5}$
	$U10 > 13$ m s^{-1}: $(5.9U_{10}^2 - 49.3)(Sc_{Hg}/Sc_{CO2})^{-0.5}$
Wanninkhof (1992)	$0.31U_{10}^2 (ScHg/Sc_{CO2})^{-0.5}$
Wanninkhof and McGillis (1999)	$0.0283U_{10}^3 (Sc_{Hg}/Sc_{CO2})^{-0.5}$
Nightingale et al. (2000)	$(0.333U_{10} + 0.22U_{10}^2)(Sc_{Hg}/Sc_{CO2})^{-0.5}$
McGillis et al. (2001)	$(3.3 + 0.026\ U_{10}^3)(Sc_{Hg}/Sc_{CO2})^{-0.5}$

2.4 Chapter conclusion

In summary, Hg^0 air–sea exchange is a complex process influenced by a range of environmental factors including wind speed, solar radiation, SST and microbial activity. A key challenge remains in understanding the net effect of these factors in the natural environmental and at large temporal and spatial scales, due to scarce measurements. Further uncertainty arises from reliance (of global-model based air–sea exchange estimates) on gas transfer velocities developed for other gases. These uncertainties propagate into global model estimates, hindering

[17] The Schmidt number (Sc) represents the ratio of kinematic viscosity of water and the diffusivity of a gas and depends on water temperature and salinity. k_w is typically scaled to the Schmidt number of CO_2, where a Sc_{CO2} value of 600 or 660 is used. Unlike CO_2, no fixed value for Sc_{Hg} is available, and it is empirically derived.

efforts to constrain the global Hg cycle. Addressing these uncertainties is essential for improving global Hg budgets and assessing the effectiveness of regulatory policies.

In the next two chapters, this dissertation addresses these challenges by utilising indirect measurements, that is, atmospheric Hg^0 observations from long-term, ground-based monitoring sites to study Hg^0 air–sea exchange. It explores the influence of different environmental parameters the exchange across various temporal scales and evaluates their net effect. Furthermore, a novel approach is applied to constrain the net global ocean Hg^0 evasion flux, independent of k_w parameterisations, with the aim of reducing the uncertainties associated with traditional gas exchange model estimates.

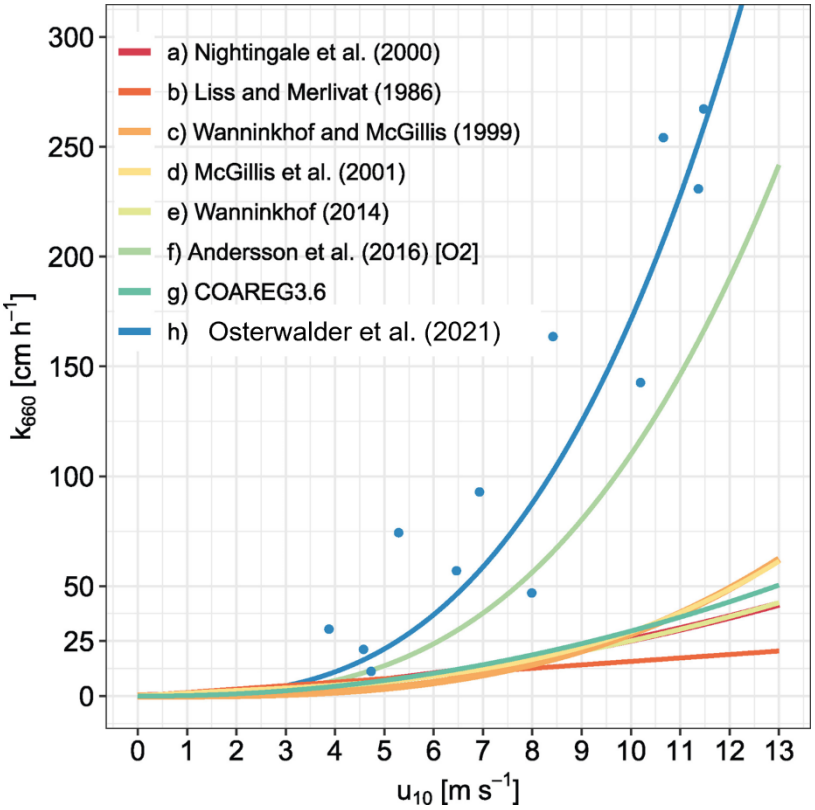

Figure 2: Parameterisations of the transfer velocity as a function of 10 m wind speed, normalized to a Schmidt number of 660 (20° C for CO_2 in seawater). The derivations by Nightingale et al. (2000), Liss and Merlivat (1986), Wanninkhof and McGillis (1999), McGillis et al. (2001) and Wanninkhof (2014) are based on CO_2 and dimethyl sulfide measurements, and are listed in Table 1. The derivation from Andersson et al. (2016) is based on eddy co-variance with oxygen, the COAREG3.6 is based on Coupled Ocean-

Atmosphere Response Experiment flux algorithm with CO_2 (Fairall et al., 2011). Osterwalder et al. (2021) shows the cubic fit ($k = 0.18\ u_{10}$) of measured transfer velocities of Hg^0 based on relaxed eddy accumulation Hg^0 emission measurements (blue dots). (Adaptation from Osterwalder et al. (2021), under CC BY 4.0; https://creativecommons.org/licenses/by/4.0/).

Chapter 3 – Constraining elemental mercury air–sea exchange using long-term ground-based observations

This chapter is based on the following paper, which has been accepted for publication in Atmospheric Chemistry and Physics:

Molepo, K. M., Bieser, J., Koenig, A. M., Hedgecock, I. M., Ebinghaus, R., Dommergue, A., Magand, O., Angot, H., Travnikov, O., Martin, L., Labuschagne, C., Read, K., and Bertrand, Y.: Constraining elemental mercury air–sea exchange using long-term ground-based observations, *EGUsphere [preprint]*, https://doi.org/10.5194/egusphere-2024-3722, 2024.

Abstract

Air–sea exchange of gaseous elemental mercury (Hg^0) is a major component of the global mercury (Hg) biogeochemical cycle but remains poorly understood due to sparse in situ measurements. Here, we used long-term atmospheric Hg^0 (Hg^0_{air}) observations combined with air mass back trajectories at four ground-based monitoring sites to study Hg^0 air–sea exchange. The trajectories showed that all four sites sample mainly marine air masses. At all sites, we observed a gradual increase in mean Hg^0_{air} concentration with air mass recent residence time in the Marine Boundary Layer (MBL), followed by a steady state. The pattern is consistent with the thin film gas exchange model, which predicts net Hg^0 emissions from the surface ocean until the Hg^0_{air} concentration normalised by Henry's law constant matches the surface ocean dissolved Hg^0 (Hg^0_{aq}) concentration. This provides strong evidence that ocean Hg^0 emissions directly influence Hg^0_{air} concentrations at these sites. Using the observed relationship between Hg^0_{air} concentrations and air mass recent MBL residence time, we estimated mean surface ocean Hg^0_{aq} concentrations of 4–7 pg L^{-1} for the North Atlantic and Arctic oceans (AA) and 4 pg L^{-1} for the Southern, South Atlantic and south Indian oceans (SSI). Estimated ocean Hg^0 emission fluxes ranged between 0.57–0.86 and 0.60–0.87 ng m^{-2} h^{-1} for the AA and SSI, respectively, with a global extrapolated mean flux of around 2270 t y^{-1} (1600–

2900 t y^{-1}). This study demonstrates the applicability of long-term, ground-based Hg^0_{air} observations in constraining Hg^0 air–sea exchange.

3.1 Introduction

Mercury (Hg), a ubiquitous element in the environment, has gained widespread attention due to its adverse effects on human health and ecosystems (AMAP/UNEP, 2018; Budnik and Castelyn, 2019; Al-Sulaiti et al., 2022; Basu et al., 2023). While naturally occurring in the Earth's crust and released by natural processes, anthropogenic activities have dramatically increased the amount of Hg emitted into the environment (Sunderland and Mason, 2007; Amos et al., 2013; Lamborg et al., 2014; Zhang et al., 2014; Streets et al., 2017; Li et al., 2020; Sonke et al., 2023). Consequently, Hg has become a persistent global pollutant.

The elemental form of Hg (Hg^0) is particularly important. Owing to its chemical inertness and low water solubility, once emitted, Hg^0 stays in the atmosphere for several months to a year (Horowitz et al., 2017; Saiz-Lopez et al., 2018; Shah et al., 2021), allowing it to travel thousands of kilometres across the globe, impacting even remote areas (Travnikov 2005; Durnford et al., 2010; Koenig et al., 2022). Although in the atmosphere Hg^0 exists in low concentrations with no direct harmful effects (Holloway and Littlefield, 2011), a portion of the atmospheric Hg^0 is gradually oxidised to more soluble divalent Hg compounds (Hg^{II}) that are readily deposited to surface reservoirs (Horowitz et al., 2017; Saiz-Lopez et al., 2018; Shah et al., 2021). In aquatic environments, some of this deposited Hg^{II} is converted to methylmercury (Lehnherr, 2014), a highly toxic compound that bioaccumulates and biomagnifies up the food chain (Lehnherr, 2014), posing serious health risks to humans through the consumption of seafood (Driscoll et al., 2013; Zillioux, 2015; AMAP/UNEP, 2018; Al-Sulaiti et al., 2022).

The exchange of Hg^0 between the atmosphere and the oceans plays a crucial role in the cycling of Hg in the environment. Atmospheric deposition, being the dominant source of Hg (Hg^0, as well as Hg^{II}) entering the ocean (Horowitz et al., 2017; AMAP/UNEP, 2018; Zhang et al., 2019, 2023; Jiskra et al., 2021; Shah et al., 2021), strongly influences the distribution of aqueous Hg (Strode et al., 2007; Kuss et al., 2011; Soerensen et al., 2014). On the other hand, most of the deposited Hg is eventually re-emitted back to the atmosphere, with ocean emissions constituting about one-third of the total annual Hg released to the atmosphere (Horowitz et al.,

2017; AMAP/UNEP, 2018; Zhang et al., 2019; Shah et al., 2021). Through this "multihop" mechanism (Hedgecock and Pirrone, 2004), where atmospheric Hg is deposited to the ocean and the ocean re-emits it back to the atmosphere (as Hg^0), ocean emissions contribute to the long-range transport of Hg^0 and extend the lifetime of Hg actively cycling in the environment (Strode et al., 2007; Amos et al., 2013). Conversely, reduction of dissolved Hg^{II} to Hg^0 in the water column and its subsequent evasion decreases the Hg^{II} reservoir available for conversion to methylmercury (Lehnherr, 2014). Evidently, accurately characterising Hg^0 air–sea exchange is critical.

Our understanding of Hg^0 air–sea exchange and cycling in the Marine Boundary Layer (MBL) mainly derives from in situ measurements performed during ship-board sampling campaigns (e.g., Gårdfeldt et al., 2003; Andersson et al., 2007, 2008b, 2011; Kuss et al., 2011; Soerensen et al., 2013, 2014; Mason et al., 2017; Nerentorp Mastromonaco et al., 2017; Wang et al., 2017; Wang et al., 2019). These observations, comprising of simultaneous measurements of Hg^0 in air (Hg^0_{air}) and in surface seawater (Hg^0_{aq}), along with variables such as sea surface temperature (SST) and wind speed, have been instrumental in discerning the spatio–temporal variability of Hg^0 at the air–sea interface, estimating Hg^0 air–sea exchange fluxes, as well as understanding the factors driving these processes. However, these measurements are sparse, covering only short periods (typically a few days to a few weeks), and are predominantly performed in the northern hemisphere. Chemical transport models can provide insights beyond the spatio–temporal limitations of in situ measurements, but they are also limited by the sparsity in direct measurements, such as for validating air–sea exchange parameterisations applied in the models (e.g., Zhang et al., 2019). As a result, many aspects of Hg^0 dynamics at the air–sea interface remain poorly understood.

Some ground-based monitoring sites sample air masses with extended ocean exposure, offering a valuable opportunity to study Hg^0 cycling at the air–sea interface. Moreover, many of these sites have continuous Hg^0_{air} records spanning several years (e.g., Sprovieri et al., 2016). Despite their potential, their application for extensive analyses of Hg^0 air–sea exchange remains underexplored, with studies primarily using them for model validation (e.g., Soerensen et al., 2010b) or for complementing ship-based measurements (e.g., Gårdfeldt et al., 2003; Sommar et al., 2010).

In this study, we analyse Hg^0_{air} observations from four ground-based monitoring sites to study Hg^0 air–sea exchange. We use measurements from the longest continuous monitoring sites in the northern hemisphere (NH) and southern hemisphere (SH), Mace Head and Cape Point, respectively, as well as from the sub-tropical North Atlantic site Cabo Verde Observatory and the remote southern Indian Ocean site Amsterdam Island. The observations are combined with air mass back trajectories to gain insights into the sources and travel paths of air masses sampled at the sites. The results from this study will contribute towards an improved understanding of Hg^0 air–sea exchange.

3.2 Data and methods

3.2.1 Observations

3.2.1.1 Site descriptions

We used observations from four monitoring sites, namely, Mace Head, Cabo Verde Observatory, Cape Point and Amsterdam Island (Figure 3). Below is a brief description of each site.

Mace Head

Mace Head (53°20′ N, 9°54′ W) is located in County Galway on the west coast of Ireland (Ebinghaus et al., 2011). It is exposed to the North Atlantic Ocean with a wide clean sector between 180° and 300° (Ebinghaus et al., 2011), ideally situated to study atmospheric composition under northern hemispheric background conditions but also under regionally polluted European continental conditions, when air masses originate from an easterly direction (Ebinghaus et al., 2011). On average, over 50 % of air masses that arrive at Mace Head are within the clean sector, having recently travelled thousands of kilometres across the North Atlantic Ocean (Ebinghaus et al., 2011). The climate at Mace Head is mild and moist (www.macehead.org, last access: June 2022), with an average air temperature of about 10 °C, generally high relative humidity (80–85 %) and an annual rainfall of approximately 1200 mm. Air sampling at the site is performed from two towers (10 m and 22 m high) located 100 m from the shoreline and 50 m from the high-water mark. There are no industrial activities that could influence the measurements at Mace Head (Ebinghaus et al., 2011), with the nearest major urban area, Galway city, situated about 90 km east of the station (Ebinghaus et al., 2011).

Mace Head is operated by the Atmospheric Science Research Group at the National University of Ireland, Galway (Kock et al., 2005), and is part of multiple international research networks, including the Global Mercury Observation System (GMOS) and the Global Atmosphere Watch (GAW) of the World Meteorological Organisation (WMO).

Cabo Verde Observatory

Cabo Verde Observatory (16°51′ N, 24°52′ W) lies on the northeast side of São Vicente (Read et al., 2017), one of ten islands in the Cabo Verde archipelago in the North Atlantic Ocean (Read et al., 2017). The site is characterised by a warm and dry climate, with a mean annual air temperature of 24 ± 2 °C and annual rainfall below 200 mm, most of which occurs in the rainy season of July–November (Read et al., 2017). The observatory receives mostly (about 95 % of the time) air masses from the northeasterly trade winds, which have typically travelled for five days over the ocean (Read et al., 2017), providing the opportunity to study clean marine air (Carpenter et al., 2010; Read et al., 2017). Air sampling at Cabo Verde Observatory is performed 50 m from the coastline at 10 m above sea level (Carpenter et al., 2010). The observatory is operated as a multilateral project between the United Kingdom, Germany and the Republic of Cabo Verde (Read et al., 2017), and is also part of both the GMOS and WMO-GAW network of sites (Carpenter et al., 2010; Sprovieri et al., 2016; Read et al., 2017).

Cape Point

Cape Point (34°21′ S, 18°29′ E) is located on the southern tip of the Cape Peninsula, about 60 km south of Cape Town, South Africa (Martin et al., 2017). It is situated within the Cape Point National Park, on a coastal cliff 230 m above sea level (Brunke et al., 2004; Martin et al., 2017). The site has a Mediterranean-type climate, characterised by moderate temperatures, dry summers and increased precipitation during winter (Brunke et al., 2004). The prevailing wind direction at Cape Point is from the southeast to southwest, and thus most air masses advected to the site are clean marine air from the Southern Ocean (Brunke et al., 2004). On average, over 50 % of the air masses reaching Cape Point originate from this clean oceanic sector, having recently travelled thousands of kilometres across the southern oceanic regions (Labuschagne et al., 2018). Nevertheless, the site occasionally experiences air masses from the north to northeast, mainly in winter, that are influenced by anthropogenic emissions from the greater Cape Town area and/or by other continental sources (Brunke et al., 2010). Cape Point is

operated by the South African Weather Service (SAWS) and is also part of the GMOS and WMO-GAW networks (Martin et al., 2017; Slemr et al., 2020).

Amsterdam Island

Amsterdam Island (37°48′ S, 77°34′ E) is a small subtropical island (55 km^2) in the southern Indian Ocean, located about 3400 km and 5000 km downwind of Madagascar and South Africa, respectively (Angot et al., 2014; Slemr et al., 2015, 2020; Li et al., 2023; Magand et al., 2023; Tassone et al., 2023). The atmospheric monitoring station is situated at Pointe Bénédicte at the northwest end of the island at an altitude of 70 m above sea level (Angot et al., 2014; Magand et al., 2023). Air sampling and monitoring at the Pointe Bénédicte station is performed from different heights depending on the pollutant studied, with atmospheric Hg being sampled at 6 m above ground level. The site has an oceanic climate with mild temperatures (ranging between 11 and 17 °C over the year), high relative humidity (65 to 85 %) and frequent presence of clouds and abundant rainfall (total annual average between ~800 mm and ~1300 mm from the last decades) (Miller et al., 1993; Angot et al., 2014; Tassone et al., 2023). The dominant surface wind direction at Amsterdam Island is westerly and northwesterly, and wind speeds are comparatively high throughout the year (with an annual average of 7.6 m s^{-1}; Miller et al., 1993), peaking in austral winter (Baboukas et al., 2004; Li et al., 2023). The island is largely free of human disturbance. The only possible, but very rare, local source of pollution may emanate from the 20–40 scientific research and technical crew in Martin-de-Viviès life base 2 kilometres downwind of the Pointe Bénédicte station. Amsterdam Island is running under administration of Terres Australes et Antarctiques Françaises (TAAF), the French Southern and Antarctic Lands, and is scientifically operated by the French Polar Institute (IPEV) research programs, all year round. The monitoring station is part of the French national monitoring system, the Integrated Carbon Observation System, ICOS-France Atmosphère for the long-term observation of greenhouse gases (El Yazidi et al., 2018; Magand et al., 2023). As with Mace Head, Cabo Verde Observatory and Cape Point, the Pointe Bénédicte station in Amsterdam Island is part of the GMOS network and is also labelled as a WMO-GAW site (Angot et al., 2014; Slemr et al., 2015, 2020; Magand et al., 2023).

3.2.1.2 Atmospheric Hg measurements

Atmospheric Hg has been measured since September 1995, December 2011, March 2007 and January 2012 at Mace Head, Cabo Verde Observatory, Cape Point and Amsterdam Island, respectively, using Tekran 2537 A/B model analysers (Tekran Inc., Toronto, Canada; Ebinghaus et al., 2002; Read et al., 2017; Slemr et al., 2020; Magand et al., 2023). The analysers are based on Hg enrichment on a gold cartridge, followed by thermal desorption and detection by cold vapour atomic fluorescence spectroscopy (CVAFS) at 253.7 nm (Fitzgerald and Gill, 1979; Bloom and Fitzgerald, 1988). The analysers use two gold cartridges, switching between the cartridges to allow for alternating sampling and desorption, resulting in continuous sampling of the incoming air (Ebinghaus et al., 2011; Martin et al. 2017; Slemr et al., 2020; Magand et al., 2023). Concentrations are expressed in nanograms per cubic metre at standard temperature and pressure (STP) conditions (273.15 K, 1013.25 hPa) with an instrumental detection limit close to 0.1 ng m^{-3} and an Hg^0_{air} average uncertainty value of about 10% (Slemr et al., 2015).

The instruments are automatically calibrated every 25 h at Mace Head and Cape Point, every 72 h at Cabo Verde Observatory and every 69 h at Amsterdam Island using internal permeation sources (Ebinghaus et al., 2011; Read et al., 2017; Slemr et al, 2020; Magand et al., 2023). The permeation sources are in turn checked (annually at Cabo Verde Observatory and Cape Point, bi-annually at Mace Head and quarterly at Amsterdam Island) by manual injections of saturated Hg vapour from a temperature-controlled vessel adapted following Dumarey et al. (1985) procedures (Ebinghaus et al., 2011; Slemr et al, 2020; Magand et al., 2023). To ensure comparable results, the Tekran analysers at all four sites are operated and calibrated under GMOS standard operating procedures (SOPs; Sprovieri et al., 2016; Martin et al., 2017; Read et al., 2017; Slemr et al., 2020). The sampling procedure, quality assurance and quality control measures in operation at the sites are detailed in several references (e.g., Ebinghaus et al., 2011; Angot et al., 2014; Sprovieri et al., 2016; Slemr et al., 2020; Magand et al., 2023).

Several studies referenced here, including some of which use the same atmospheric Hg observations as those in the present study (i.e., from the same monitoring sites), denote (the) Tekran 2537A/B measurements as total gaseous mercury (TGM; TGM = Hg^0_{air} + gaseous oxidised mercury, Hg^{II}_{air}) (e.g., Gårdfeldt et al., 2003; Temme et al., 2003; Kock et al., 2005; Xia et al., 2010; Andersson et al., 2011; Ebinghaus et al., 2011; Read et al., 2017). However,

at all four sites studied here, it has been suggested that the measurements are most likely of Hg^0_{air} rather than TGM, as Hg^{II}_{air} is easily lost to sea-salt deposits in the inlet tubing and filters of the instrument (Weigelt et al., 2015; Read et al., 2017; Slemr et al., 2020). In Amsterdam Island, between 2012 and 2015 atmospheric mercury species were measured using a Tekran Hg speciation unit (Tekran 1130/1135 models), ensuring that only Hg^0_{air} is sampled and analysed with the associated Tekran 2537A/B model. Since the uninstallation of the speciation unit at the site in 2015, the Tekran 2537A/B instrument has been deployed with a specific setup using two 0.45 µm polyethersulfone cation-exchange membranes (PES-CEM, 0.45 µm, 47 mm, Merck Millipore®) installed at the inlet of the heated line, preventing the introduction of oxidised species and ensuring that only Hg^0_{air} is measured (Magand et al., 2023). Furthermore, TGM typically comprises mostly (> 98 %) Hg^0_{air} (e.g., Soerensen et al., 2010a; Cheng et al., 2014; Yin et al., 2018; Wang et al., 2019). Therefore, we regard the Tekran 2537A/B measurements at the four sites as Hg^0_{air}, and make no distinction between TGM and Hg^0_{air}, referring to the measurements as Hg^0_{air}, when referencing the above-mentioned studies.

The record of hourly mean Hg^0_{air} observations from the four sites used in this study is presented in Figure 3. Throughout this study, the data were analysed and are presented in their local time.

3.2.1.3 ^{222}Rn measurements from Cape Point

Since 1999, atmospheric radon (^{222}Rn) has been continuously measured at Cape Point using a two flow-loop, dual-filter detector designed by the Australian Nuclear Science and Technology Organisation (ANSTO) and partially constructed locally (Brunke et al., 2004; Botha et al., 2018). The instrument operates by passing ambient air through a particulate filter into a large chamber, where the ^{222}Rn gas decays (Brunke et al., 2004). A second filter collects the ^{222}Rn decay products, which are detected by means of a screen coated with the scintillator material zinc sulphide and viewed by a photomultiplier (Brunke et al., 2004). The count rate is proportional to the ambient ^{222}Rn concentration (Brunke et al., 2004). The detector at Cape Point has been continuously developed (Brunke et al., 2004; Botha et al., 2018). In 2011, an upgraded version of the instrument was installed, incorporating system design improvements such as an automated calibration system and a delay volume, increasing the accuracy and reliability of the measurements at the site (Botha et al., 2018).

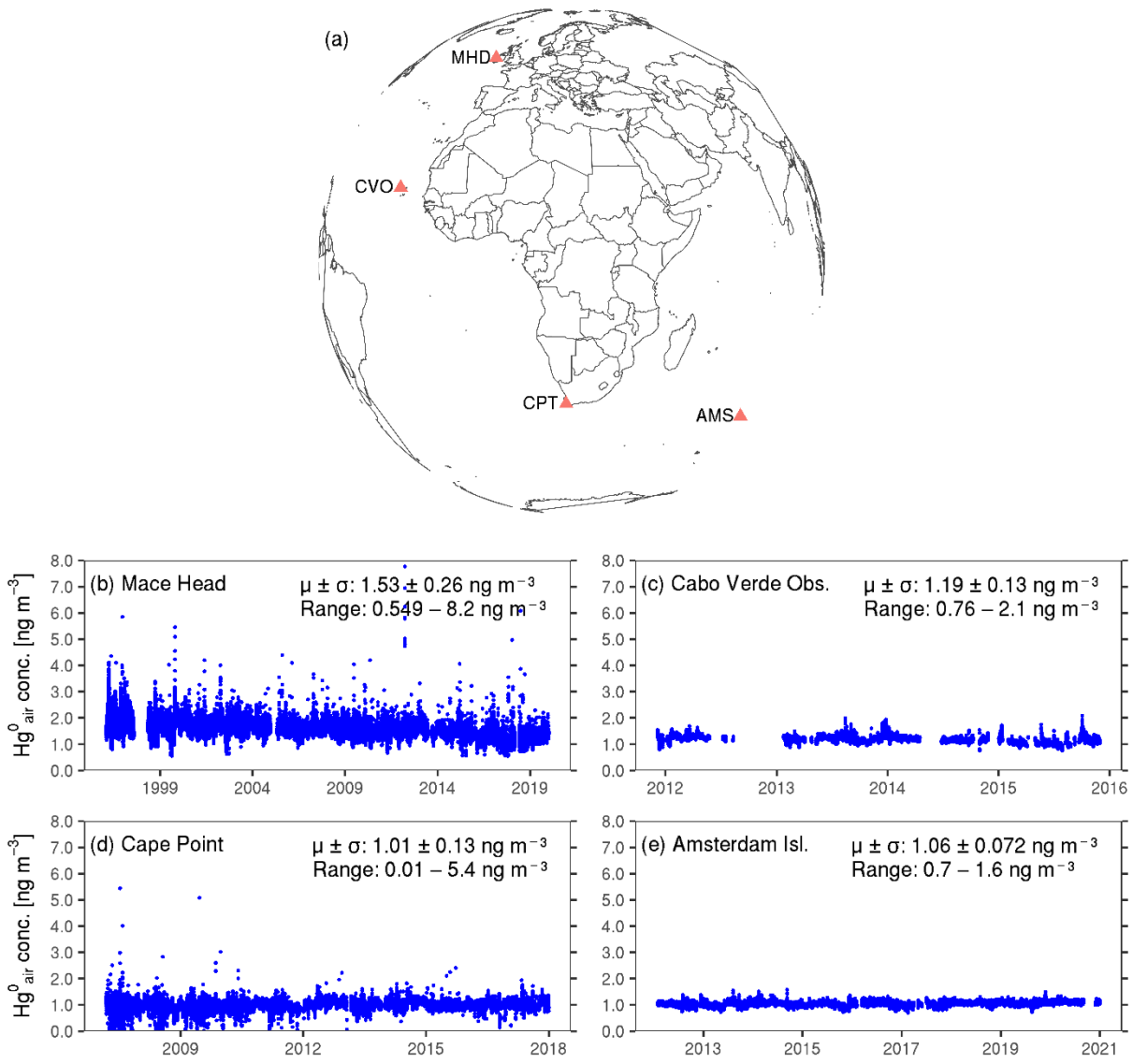

(f)

Station	Temporal coverage period	No. of data points	Perc. valid data [%]
Mace Head	2 Feb 1996–06 Jan 2020	171 399	82
Cabo Verde Obs.	5 Dec 2011–29 Dec 2015	20 894	60
Cape Point	8 Mar 2007–31 Dec 2017	83 303	88

Amsterdam Island	28 Jan 2012–31 Dec 2020	56 844	73

Figure 3: Overview of the Hg^0_{air} data used in the study. (a) Map showing the locations of the four study sites, Mace Head (MHD), Cabo Verde Observatory (CVO), Cape Point (CPT) and Amsterdam Island (AMS). (b)–(e) Hourly mean Hg^0_{air} concentrations at Mace Head, Cabo Verde Observatory, Cape Point and Amsterdam Island, respectively. The mean ± 1 standard deviation and the range of the hourly observations are shown in each panel. Note that the extent of the x-axis differs across the four sites. For better readability of the data, where the y-axis scales are adjusted to each site's data distribution, see Figure A1.1 in Appendix A. (f) Summary of the hourly mean Hg^0_{air} data coverage at the four sites, showing the temporal coverage of the observations used in the present study, the total number of hourly data points and the percentage of hourly time stamps over the coverage period with (valid or non-missing) data.

As described in detail in Botha et al. (2018), the radon detector's sample inlet is located 30 m above ground level and ^{222}Rn is measured at a resolution of 30 min and further processed to an average 1 h temporal resolution. The detector is calibrated monthly by introducing a known concentration of ^{222}Rn from a calibration source (^{226}Ra source with ^{222}Rn production rate of 2.94 Bq min^{-1}) acquired from Pylon Electronics, Inc., Canada (Brunke et al., 2004). The instrument has a lower limit of detection of 25 ± 8 mBq m^{-3}, and the hourly measurements have an uncertainty of around 15 % at 100 mBq m^{-3} and 9 % at 1000 mBq m^{-3} (Botha et al., 2018).

In this work, we use hourly ^{222}Rn data corresponding to the period of the Cape Point Hg^0 dataset (i.e., the period 8 March 2007–31 December 2017).

3.2.2 Air mass back trajectories

We applied the Hybrid Single-Particle Lagrangian Integrated Trajectory (HYSPLIT) model (Stein et al., 2015) to trace air masses arriving at the monitoring sites. For each station and hour of the day, we calculated a 144-hour (6-day) air mass back trajectory starting at 50 m above model ground level, using the National Centers for Environmental Prediction/National Center for Atmospheric Research (NCEP/NCAR) reanalysis data with a 2.5° spatial and 6-hourly temporal resolution (Kalnay et al., 1996) for model input. Each of the 144 segments of every trajectory was then assigned to one of two categories based on the underlying surface over which the segment is passing:

- *Marine* (or, *oceanic*): segments passing over an area where the bathymetric elevation is 0 m or below.

- *Terrestrial* (or, land): segments passing over an area where the bathymetric elevation is above 0 m.

The bathymetry information was obtained from the GEneral Bathymetric Chart of the Oceans Grid (GEBCO_GRID), with a 15 arc-second spatial resolution (GEBCO Compilation Group, 2020). The segments were further classified into one of two categories, according to their height in the atmosphere:

- *Boundary layer*: segments at or below the height of the planetary boundary layer (PBL).
- *Free tropospheric*: segments above the height of the PBL.

For this step, we used PBL height data from the ERA5 re-analysis product of the European Centre for Medium-Range Weather Forecasts (ECMWF; Hersbach et al., 2020), with a temporal resolution of 1 h and spatial resolution of 0.25° × 0.25°. Therefore, each of the 144 segments of every trajectory was assigned to one of four categories: marine boundary layer (MBL), free troposphere over the ocean (FT_ocean), continental planetary boundary layer (CPBL), or free troposphere over land (FT_terrestrial; see Figure A1.2 in Appendix A).

3.3 Results and discussion

3.3.1 Overview of Hg^0_{air} observations at Mace Head, Cabo Verde Observatory, Cape Point and Amsterdam Island

The record of hourly averaged Hg^0_{air} measurements at the four sites is shown in Figure 3. Over the analysis periods, the mean Hg^0_{air} concentration was 1.53 ± 0.26, 1.19 ± 0.13, 1.01 ± 0.13 and 1.06 ± 0.07 ng m^{-3} (mean ± 1 standard deviation) at Mace Head, Cabo Verde Observatory, Cape Point and Amsterdam Island, respectively. The higher mean concentration at Mace Head and, to a lesser extent, Cabo Verde Observatory compared to Cape Point and Amsterdam Island is consistent with previous studies that have reported higher Hg^0_{air} levels in the NH than in the SH (e.g., Temme et al., 2003; Soerensen et al., 2010a, 2014; Sprovieri et al., 2010, 2016; Xia et al., 2010). The inter-hemispheric gradient in Hg^0_{air} concentrations has been widely discussed in the literature and is largely attributed to the bulk burden of anthropogenic Hg emissions occurring in the NH (Temme et al., 2003; Sprovieri et al., 2010, 2016; Street et al., 2017; AMAP/UNEP, 2018).

Figure 4 shows the mean seasonal variability of Hg^0_{air} concentrations across the four sites. At Mace Head, Hg^0_{air} levels are slightly but significantly higher in winter (December to May, 1.57 ± 0.27 ng m^{-3}, n = 84 228) than in summer (June to November, averaging 1.48 ± 0.25 ng m^{-3}, n = 87 171) ($p < 2.2e^{-16}$, Mann-Whitney U-Test). As with Mace Head, concentrations at Cabo Verde Observatory are slightly but significantly higher around winter (December–May, 1.22 ± 0.12, n = 11 296) compared to summer (June–November, 1.16 ± 0.12, n = 9 598) ($p < 2.2e^{-16}$, Mann-Whitney U-Test). A similar seasonal pattern has been observed at other ground-based monitoring stations (e.g., Kock et al., 2005; Lan et al., 2012; Sprovieri et al., 2016; Jiskra et al., 2018) as well during ship-board sampling campaigns (e.g., Soerensen et al., 2010a) in the NH. Several explanations have been proposed for the northern hemispheric Hg^0_{air} seasonality, including, increased anthropogenic emissions from fossil-fuel combustion for heating in winter (Ebinghaus et al., 2002; Lan et al., 2012), higher ocean Hg^0 emissions from the North Atlantic Ocean in winter (Soerensen et al., 2010b), and more recently, increased vegetation Hg^0 uptake in summer (Jiskra et al., 2018; Feinberg et al., 2022).

Amsterdam Island shows slightly but significantly higher Hg^0_{air} concentrations around winter (June–September, 1.07 ± 0.06, n = 18 697) ($p < 2.2e^{-16}$, Mann-Whitney U-Test). Angot et al. (2014) as well as Slemr et al. (2020), who previously reported the same seasonality for the site, attributed it to long-range transport of polluted air masses from southern Africa between July and September, which coincides with the biomass-burning season in the region. Nevertheless, the observed winter peak at Amsterdam Island (in this study) corresponds to only a ~ 1 % increase from the site's overall mean concentration. Similarly, at Mace Head as well as Cabo Verde Observatory, the winter maximum (summer minimum), though significantly higher (lower) than the overall mean concentration ($p < 2.2e^{-16}$, Mann-Whitney U-Test), represents only a ~ 3 % change from the overall mean. No clear seasonality is detected at Cape Point.

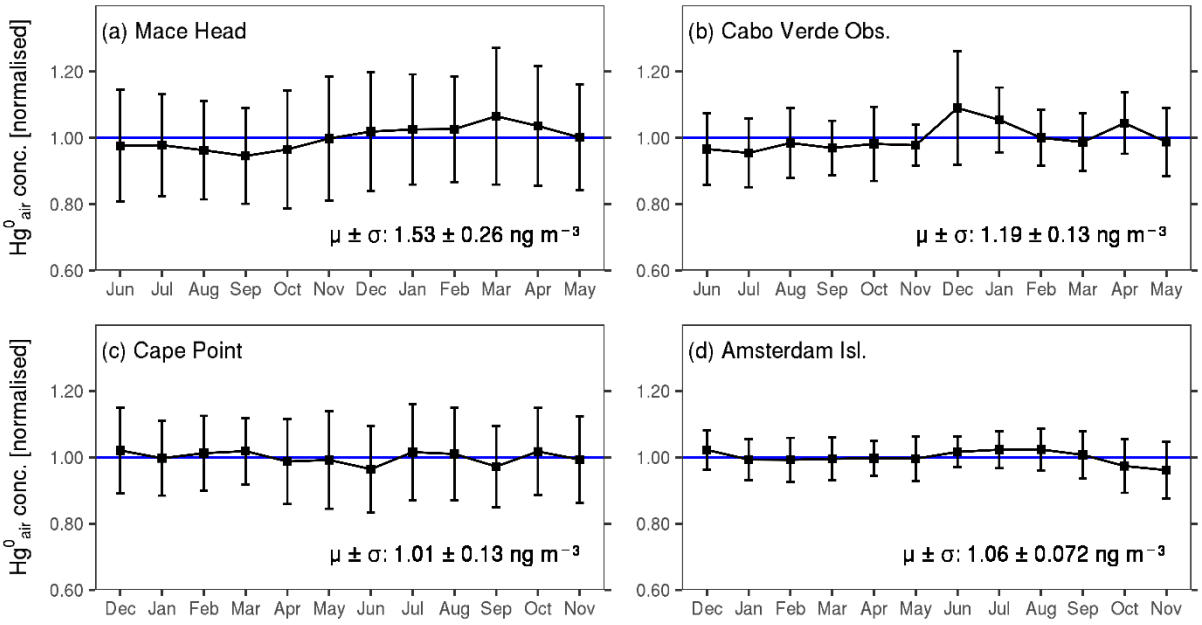

Figure 4: Normalised mean seasonal Hg^0_{air} concentrations at the four sites. The mean ± 1 standard deviation of the hourly observations is shown in each panel. The bars show one standard deviation of the monthly means. The blue horizontal line represents the normalised mean value (i.e., 1 ng m^{-3}). The months are ordered starting in June for Mace Head and Cabo Verde Observatory and in December for Cape Point and Amsterdam Island, such that the plots consistently start in summer and end in spring (of the respective hemisphere).

The diurnal variability of Hg^0_{air} at the four sites is quite weak as well, with daily mean minima and maxima values reflecting just a ~2 % change from the overall mean concentration (Figure 5). The diurnal patterns also exhibit little seasonal variation (Figure A1.3, Appendix A). Non-existent or non-significant Hg^0_{air} diurnal variations in the marine boundary layer (MBL) have also been reported in other studies (e.g, Soerensen et al., 2010a; Wang et al., 2017; Wang et al., 2019).

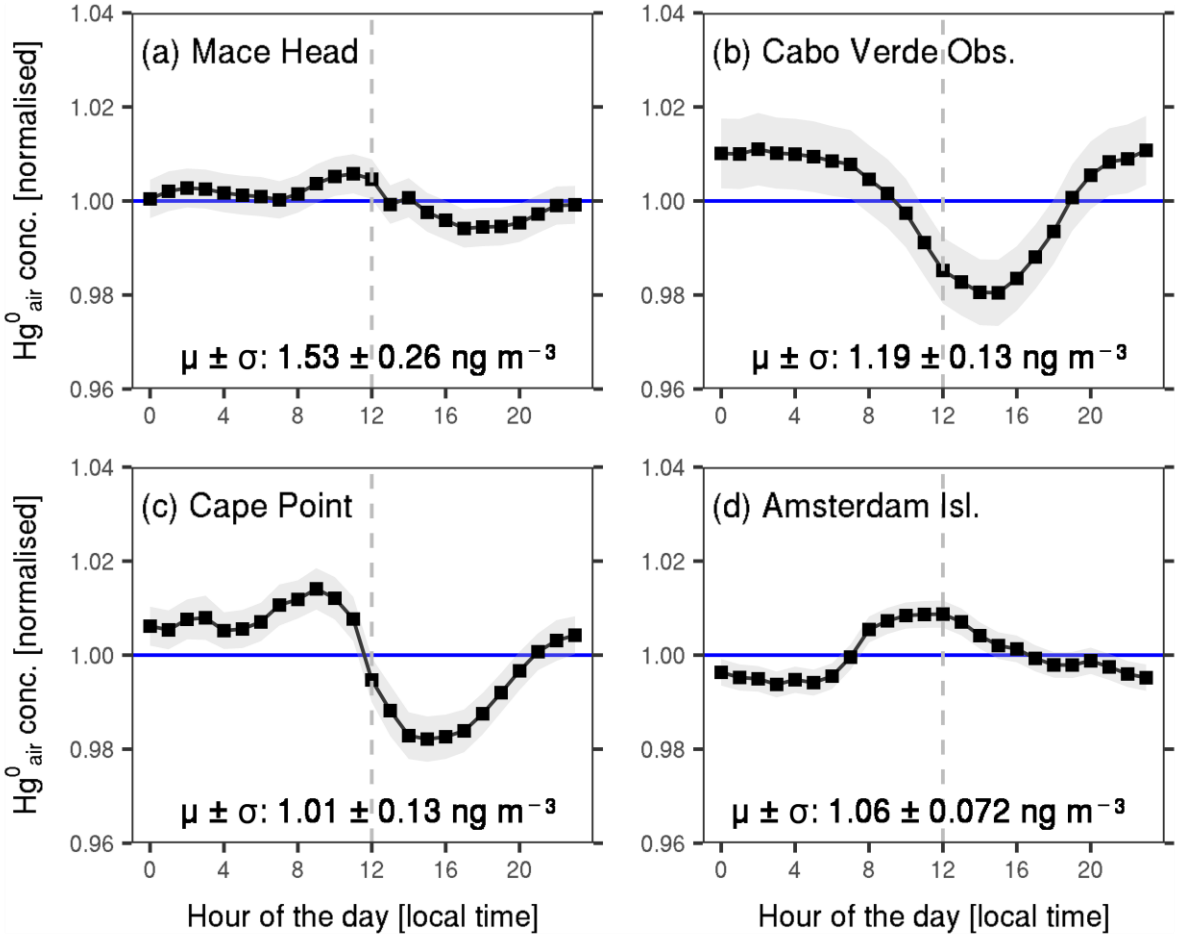

Figure 5: Normalised mean Hg^0_{air} diurnal variation at Mace Head, Cabo Verde Observatory, Cape Point and Amsterdam Island. The mean ± the standard deviation of the hourly observations is shown for each site. The shaded area shows the mean ± 2 times the standard error. The horizontal line represents the normalised mean value (i.e., 1 ng m^{-3}) and the dashed vertical line is plotted along 12:00 local time.

3.3.2 Hg^0_{air} in the MBL

A major goal of this work was to understand the dynamics of Hg^0_{air} in the MBL, especially given the weak seasonal and diurnal variability in concentrations observed at our ground-based study sites. Previous research has highlighted Hg^0 air–sea exchange as one of the key processes influencing Hg^0_{air} concentrations in the MBL (e.g., Wängberg et al., 2001; Laurier et al., 2003;

Soerensen et al., 2010a, 2010b; Carbone et al., 2016; Wang et al., 2017). In turn, Hg^0 air–sea exchange is suggested to be driven by two main factors: (i) the Hg^0 concentration gradient at the air–sea interface, and (ii) wind speed and solar radiation (e.g., Gårdfeldt et al., 2001; Wängberg et al., 2001; Laurier et al., 2003; Soerensen et al., 2010a, 2010b; 2013; Kuss et al., 2011; Wang et al., 2017). Many studies show that ocean surface waters are primarily supersaturated in Hg^0_{aq} relative to the overlaying air (e.g., Wängberg et al., 2001; Gårdfeldt et al., 2003; Andersson et al., 2011; Mason et al., 2017; Wang et al., 2017; Wang et al., 2019), creating conducive conditions for net ocean Hg^0 emission to the atmosphere. In fact, recent estimates place ocean Hg^0 evasion as the largest single net flux of Hg^0 to the atmosphere, in the range of 2800–4000 Hg^0 t y^{-1} (Horowitz et al., 2017; AMAP/UNEP, 2018; Outridge et al., 2018; Shah et al., 2021; Zhang et al., 2023). Regarding wind speed and solar radiation, both variables generally exhibit pronounced seasonal and diurnal variability. Considering these factors, it would be expected that Hg^0_{air} concentrations in the MBL also show pronounced seasonal and diurnal variability, but this is not the case.

While the four sites largely sample clean marine air, they are also occasionally affected by terrestrial sources and processes (e.g., Ebinghaus et al., 2002; Brunke et al., 2004; Slemr et al., 2013, 2020; Angot et al., 2014; Read et al., 2017; Bieser et al., 2020), albeit to varying degrees. As air masses from both the marine and terrestrial environment are sampled at the sites, this can obscure the link between observed Hg^0_{air} concentrations and the oceanic Hg^0 evasion signal. To distinguish between MBL conditions and terrestrial influences, we used the HYSPLIT back trajectories. We classified each hourly Hg^0_{air} observation at the sites into one of three categories: MBL-influenced (MBL_i), terrestrial-influenced (Terr_i) and mixed (Mixed). MBL_i was assigned to observations where 90 % or more of the (144) back trajectory segments were classified as MBL, Terr_i to those where 90 % or more of the segments were classified as CPBL, and mixed was assigned to those where neither of the first two criteria are met (see Section 3.2.2 of this chapter for the distinction between MBL- and CPBL-assigned trajectory segments). To validate the classification method, we (also) applied it to ^{222}Rn observations from Cape Point. Considering that ^{222}Rn emission by the ocean is negligible (at a rate 2 to 3 orders of magnitude lower than the terrestrial flux; Schery and Huang, 2004), and that ^{222}Rn's terrestrial source is unaffected by human activity, its consistent emission over land makes it an excellent tracer for identifying air masses of terrestrial origin over the ocean or within the troposphere for 2–3 weeks (Brunke et al., 2010; Chambers et al., 2018). The ^{222}Rn

results, presented in Figure A1.4 in Appendix A, show generally higher ^{222}Rn values for the Terr_i data compared to the MBL_i data, with a significantly larger mean concentration for the Terr_i data (3426 mBq m^{-3}, n = 56) compared to the MBL_i data (450 mBq m^{-3}, n = 30 470) ($p < 2.2e^{-16}$, Mann-Whitney U-Test). While ^{222}Rn measurements are also available at Amsterdam Island, we did not perform the above analysis for the site, as we do not expect a strong terrestrial ^{222}Rn signal, due to the remoteness of the site (which is surrounded by over 3000 km of ocean) as well as the small size of the island.

Figure A1.5 and Figure A1.6 show the seasonal and diurnal variations, respectively, for the MBL_i, Terr_i and Mixed Hg^0_{air} datasets, along with the full observations (All data) at the four sites. The summary statistics for the groups are provided in Table A1.1, Appendix A. In summary, the results show that the Hg^0_{air} observations at the sites are largely associated with air masses strongly influenced by the MBL, with little to no contribution from air masses influenced by terrestrial surfaces. The results also show little difference between the Hg^0_{air} temporal distributions (i.e., the seasonal and diurnal variations) of the full observations and the MBL_i (as well as the Mixed) data. This suggests that the weak seasonal and diurnal variations observed at the sites represent the actual MBL conditions and are not an artefact of sampling air masses from different environments.

In a recent publication, Koenig et al. (2023) analysed Hg^0_{air} observations at Maïdo Observatory, a high-altitude station (2160 m above sea level) located on La Réunion Island in the southern tropical Indian Ocean (21°4′ S, 55°48′ E). The study derived a mean lower free troposphere (LFT) Hg^0_{air} concentration of ~ 0.73 ng m^{-3}. Assuming that this value is also representative of the LFT over Cape Point and Amsterdam Island (located about 3900 and 2900 km from Maïdo observatory, respectively), the mean MBL (i.e., MBL_i) Hg^0_{air} concentrations extracted at Cape Point and Amsterdam Island (1.01 ± 0.12 and 1.06 ± 0.07 ng m^{-3}, respectively; Table A1.1) are both about 30 % larger than the LFT value from Koenig et al. (2023). In the NH, using aircraft data, Weigelt et al. (2016) reported an LFT Hg^0_{air} concentration of about 1.3 ng m^{-3} over central Europe, which is about 15 % lower than the mean MBL concentration at Mace Head (1.53 ± 0.24 ng m^{-3}). These higher MBL concentrations relative to LFT concentrations suggest net ocean Hg^0 emissions into the MBL.

A question remains, regarding the weak seasonal and diurnal variations in Hg^0_{air} concentrations in the MBL. Another recent publication, Lamborg et al. (2021), has proposed that dark reduction, rather than photoreduction, as previously believed, is responsible for most of the Hg^0_{aq} produced in the ocean and subsequently evaded to the atmosphere. Since dark reduction is less directly impacted by climatic conditions than photoreduction, this would imply constant (i.e., even under low solar radiation) Hg^0_{aq} supply to the surface ocean. This would have two implications for Hg^0 cycling at the air–sea interface. One, it would explain the weak temporal Hg^0_{air} variability in the MBL, as dark reduction would provide a relatively constant pool of Hg^0_{aq} to the surface ocean throughout the day and seasons. Secondly, and related to the first point, it would imply that the ocean is constantly emitting Hg^0 to the atmosphere.

With these considerations, we sought to investigate the influence of air mass recent residence time in the MBL on observed Hg^0_{air} concentrations. We hypothesise that, an air mass entering the MBL from the LFT carries a signature Hg^0_{air} concentration of this environment. As it travels within the MBL, there is exchange of Hg^0 between the air mass and the surface ocean. Because the ocean surface layer is typically supersaturated in Hg^0 relative to the atmosphere, there is net Hg^0 emission to the atmosphere and consequently, a gradual increase in the Hg^0 concentration of the air mass over time. Therefore, air masses which have recently spent a long time in the MBL would generally have higher Hg^0_{air} levels than those which have recently spent more time in the LFT. The results of the investigation are presented in the next section.

3.3.3 Relationship between observed Hg^0_{air} concentrations and air mass residence time in the MBL

To test our hypothesis, we used the back trajectories to study the Hg^0_{air} observations in relation to air mass recent MBL residence time. We define air mass recent MBL residence time as the number of hours that an air mass (corresponding to an hourly Hg^0_{air} observation) spent in the MBL in the last 144 hours before reaching the sampling site, that is, the number of segments of the back trajectory classified as MBL, as per our back trajectory-segment classification (described in Section 3.2.2 of this chapter). We then group together the Hg^0_{air} observations according to air mass recent MBL residence time, at an hourly resolution. Further details on the analysis are provided in Section A2, Appendix A.

Figure 6 shows mean Hg^0_{air} concentrations against air mass recent MBL residence time across the four sites. As seen in the figure, Hg^0_{air} concentrations generally increase with air mass recent MBL residence time, in agreement with our hypothesis. The observed increase exhibits an asymptotic pattern, with varying points at which a steady state (i.e., where the concentration remains mostly constant despite increasing time air masses spent in the MBL) is reached across the sites. Air masses sampled at Mace Head, Cabo Verde Observatory, Cape Point and Amsterdam Island reach a mean steady state Hg^0_{air} concentration of about 1.51 ± 0.02, 1.16 ± 0.02, 1.01 ± 0.01 and 1.06 ± 0.01 ng m^{-3} (mean ± standard deviation) at about 60, 72, 30 and 60 hours in the MBL, respectively.

The asymptotic Hg^0_{air} pattern is clearer at Cape Point and Amsterdam Island compared to Mace Head and Cabo Verde Observatory. A possible explanation for this is the contribution from anthropogenic emissions. As already mentioned, overall, anthropogenic Hg emissions are higher in the NH than in the SH. As such, it may be that, at Mace Head and Cabo Verde Observatory, the anthropogenic (emission) signal is strong enough that it obscures the relationship between Hg^0_{air} concentrations and air mass recent MBL residence time. The fact that at Mace Head and Cabo Verde Observatory the asymptotic Hg^0_{air} pattern is revealed after filtering out air masses which have had recent contact with the continental planetary boundary layer (see Section A2, Appendix A) supports this hypothesis.

Nevertheless, the observed asymptotic Hg^0_{air} increase at the sites may be partially explained by the exchange of Hg^0 between the ocean and the atmosphere. The pattern is consistent with the air–sea gas exchange model (Eq. (3.1) in Section 3.3.5), which predicts net ocean Hg^0 emissions into passing air masses until the Hg^0_{air} concentration in them normalised by the Henry's law constant matches the surface ocean Hg^0_{aq} concentration. While other processes may be involved, we are unable to discern them in this study. Concerning redox chemistry, our estimation of the rate of net chemical loss due to oxidation shows that it is two orders of magnitude lower than the rate of Hg^0 concentration change observed here (see details in Section A2, Appendix A), suggesting that the observed Hg^0_{air} concentration increase far exceeds net oxidation-driven loss. Over longer periods, net oxidation may play a more significant role in shaping Hg^0_{air} concentrations in the MBL. However, over the short time scale considered here, its impact on the observed patterns is negligible.

We also investigated seasonal variability in the observed relationship between Hg^0_{air} concentrations and air mass recent MBL residence time, however, no clear pattern emerged (Figure A1.7). Therefore, in the subsequent sections in this chapter, where we use the observed relationship to estimate surface ocean Hg^0_{aq} concentrations as well as ocean net Hg^0 emissions fluxes, seasonal analyses are not included.

3.3.4 Estimation of surface ocean Hg^0_{aq} concentrations

Assuming our findings in Section 3.3.3 can explain most of the variation in Hg^0_{air} concentrations in the MBL, we used the steady state Hg^0_{air} concentrations in air masses reaching the sites to estimate mean surface ocean Hg^0_{aq} concentrations. Based on the back trajectory footprints (see Figure 7), we assume that the estimates (both the Hg^0_{aq} concentrations, as well as the fluxes, in Section 3.3.5 below) derived from the Mace Head and Cape Verde Observatory Hg^0_{air} observations represent average conditions for the broad ocean area comprising the North Atlantic and Arctic oceans, while those derived from the Cape Point and Amsterdam Island data represent conditions for the area encompassing the Southern, South Atlantic and south Indian oceans. We apply the equation describing the air–sea exchange flux of Hg^0, F, based on the thin-film gas exchange model from Liss and Merlivat (1986):

$$F = k_w \left(Hg^0{}_{aq} - \frac{Hg^0{}_{air}}{H'} \right), \quad (3.1)$$

where k_w is the gas transfer velocity, Hg^0_{aq} and Hg^0_{air} are the surface ocean and atmospheric Hg^0 concentrations, respectively, and H' is the dimensionless Henry's law constant. Following the discussion in Section 3.3.3, for air masses that remain in the MBL long enough, we can assume that they reach steady-state conditions with the underlying ocean surface, implying an average net exchange flux of $F \approx 0$ (see the discussion on the possible effect of redox chemistry in Section A3, Appendix A). Note that this assumption does not imply a net zero air–sea exchange flux for the ocean as a whole, as unsaturated air masses continuously enter the MBL and take up Hg^0 from the surface ocean. In this case, Hg^0_{aq} is obtained with:

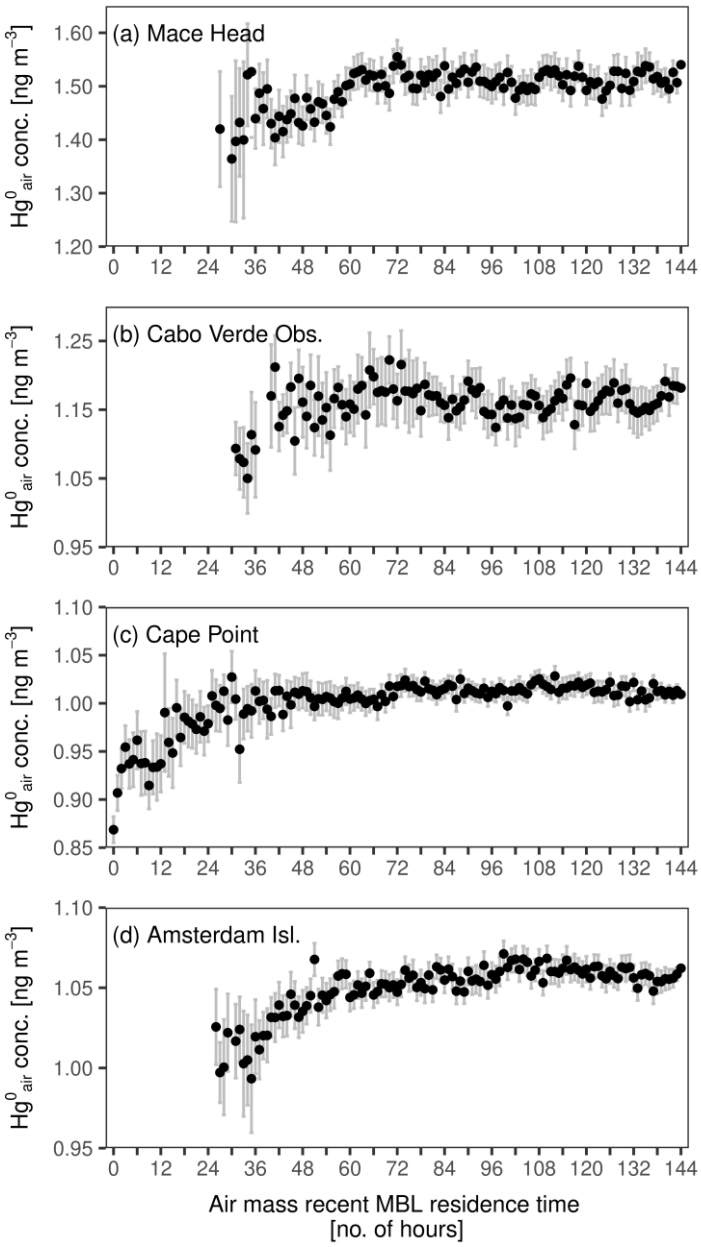

Figure 6: Mean Hg^0_{air} concentration against air mass recent MBL residence time at the four sites. The bars show 2 times the standard error of the means. Note that the y-axis differs across the four panels.

$$Hg^0_{aq} = \frac{Hg^0{}_{air(ss)}}{H'}, \quad (3.2)$$

where $Hg^0_{air(ss)}$ is the steady state Hg^0_{air} concentration. H' is calculated using the derivation from Andersson et al. (2008a),

$$H' = e^{\left(\frac{-2404.3}{T} + 6.92\right)}, \quad (3.3)$$

where T is the SST. To obtain T, we extracted hourly ERA5 SSTs (Hersbach et al., 2020) corresponding to the trajectories associated with the hourly Hg^0_{air} observations in the steady state (i.e., the observations for which air mass recent MBL residence time is greater than or equal to 60, 72, 30 and 60 hours at Mace Head, Cabo Verde Observatory, Cape Point and Amsterdam Island, respectively). More details are provided in the caption of Table 2, which summarises the $Hg^0_{air(ss)}$, T, H' and resultant mean surface ocean Hg^0_{aq} concentration for each site.

From our calculations, we derived a mean surface ocean Hg^0_{aq} concentration of 7.00 ± 0.21, 4.00 ± 0.12, 4.22 ± 0.21 and 4.74 ± 0.16 pg L^{-1} (mean ± 1 standard deviation) based on the Hg^0_{air} steady state concentration at Mace Head, Cabo Verde Observatory, Cape Point and Amsterdam Island, respectively. The higher estimate for Mace Head compared to Cape Point and Amsterdam Island is in line with elevated anthropogenic Hg emissions and resultant ocean Hg enrichment in the NH relative to the SH. The estimate for Cabo Verde Observatory is lower than that of Mace Head (and closer to that of the two SH sites). This lower Hg^0_{aq} concentration for Cabo Verde Observatory compared to Mace Head may be attributed to the much higher mean SST corresponding to the average position of the air masses sampled at the former site (294.89 ± 0.92 K at Cabo Verde Observatory compared to 284.53 ± 0.92 K at Mace Head; Table 2). While both sites receive air masses from the North Atlantic, Cabo Verde Observatory also samples tropical air masses, while Mace Head can sample polar air masses (see Figure 7). Higher SSTs enhance Hg^0_{aq} diffusivity and reduce its solubility, resulting in lower seawater concentrations.

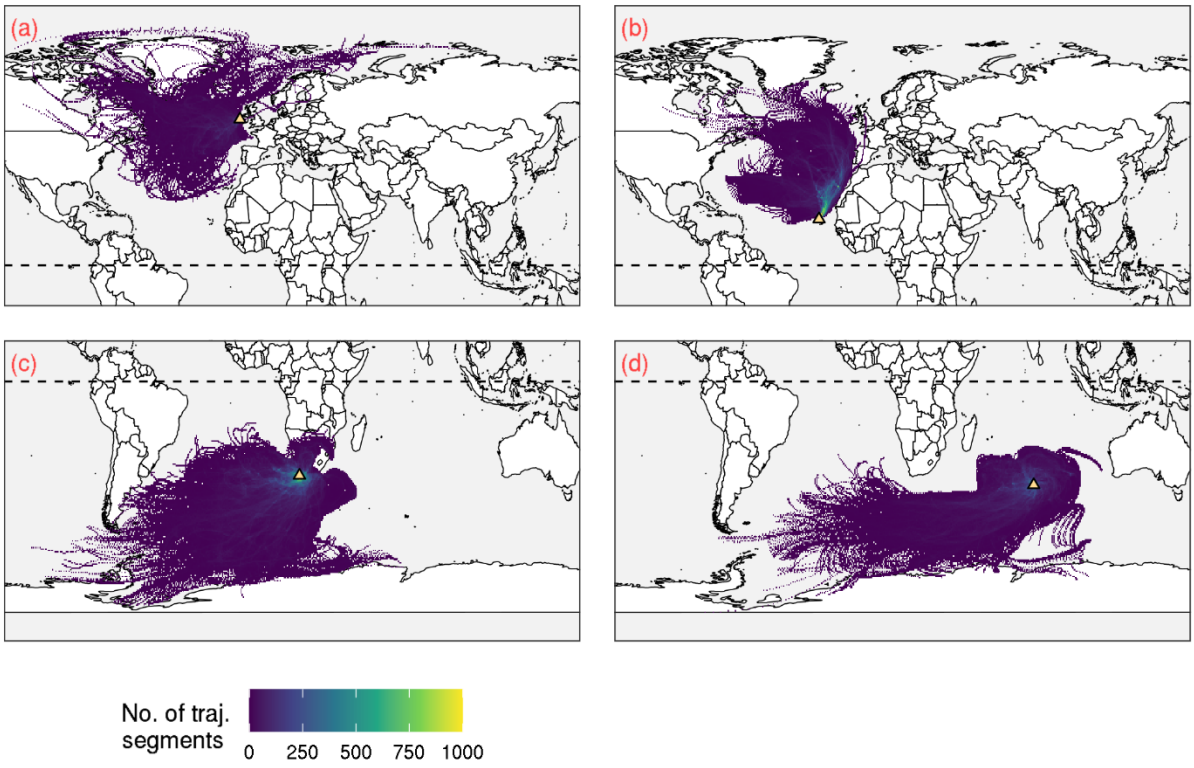

Figure 7: Back trajectory profiles illustrating the sources of air masses that arrive at (a) Mace Head, (b) Cabo Verde Observatory, (c) Cape Point and (d) Amsterdam Island. The back trajectories correspond to the data considered in deriving the profiles shown in Figure 6, and shown here is only a subset of the data, from January to December 2013. In each panel, the location of the site is illustrated by the yellow triangle, and the dotted horizontal line shows 0° latitude.

We compare our estimates to reported surface ocean concentrations in the literature obtained from direct measurements. The estimates from Mace Head and Cabo Verde Observatory are compared to values from the North Atlantic and Arctic oceans, while those from Cape Point and Amsterdam Island are compared to values from the Southern and South Atlantic oceans (no published measurements are available for the Indian Ocean, to the best of our knowledge; see Dastoor et al., 2025). We acknowledge, nevertheless, that our estimates are not directly comparable to these reported measurements for several reasons (this applies for our evasion flux estimates as well, in the next section). While the combination of measurements from multiple short-term studies can capture the full variability in surface ocean Hg^0_{aq}

concentrations, individual measurement campaigns, which typically span a few days to a few weeks (see Table 3 and Table 4, for example), primarily reflect transient conditions. In contrast, our estimates, which are derived from multi-year (Hg^0_{air}) observations, represent long-term averages. Also note that, some of the studies denote the surface water gaseous Hg measurements as dissolved gaseous mercury (DGM; e.g., Gårdfeldt et al., 2003; Wang et al., 2017), the sum of Hg^0_{aq} and dimethylmercury (DMHg). Outside of upwelling regions (Adams et al., 2024), it has been shown that surface ocean DGM concentrations comprise of mostly Hg^0_{aq}, with very minor (if any) contributions from DMHg (e.g., Mason and Fitzerald, 1993; Horvat et al., 2003; Kotnik et al., 2007; Cossa et al., 2011; Bratkič et al., 2016); therefore, we assume that the surface DGM measurements, where they are denoted as such, represent Hg^0_{aq}.

Table 2: Summary (mean ± 1 standard deviation) of steady state Hg^0_{air} (i.e., Hg^0_{air}(ss)) concentration, T, H', and resultant surface ocean Hg^0_{aq} concentration across the four sites. For each variable at each site, the mean and standard deviation are based on the mean values of the (steady state) MBL residence time bins. The mean value for each bin is the average of the individual values within the bin. For Hg^0_{air}(ss), these are the hourly Hg^0_{air} observations grouped by back trajectory recent MBL residence time. The individual T values are the mean SSTs for the trajectories corresponding to the Hg^0_{air} observations, considering only SSTs associated with segments assigned MBL. These T values are in turn used to obtain H' values, which, together with the Hg^0_{air} concentrations are used to calculate Hg^0_{aq} concentrations according to Eq. (3.2).

Site	$Hg^0_{air(ss)}$ [ng m^{-3}]	T [K]	H'	Hg^0_{aq} [pg L^{-1}]
Mace Head	1.51 ± 0.02	284.53 ± 0.92	0.217 ± 0.006	7.00 ± 0.21
Cabo Verde Obs.	1.16 ± 0.02	294.89 ± 0.92	0.291 ± 0.007	4.00 ± 0.12
Cape Point	1.01 ± 0.01	288.03 ± 1.52	0.240 ± 0.011	4.22 ± 0.21
Amsterdam Isl.	1.06 ± 0.01	285.59 ± 1.08	0.224 ± 0.007	4.74 ± 0.16

Comparison of our Hg^0_{aq} estimates to direct measurements from the literature is presented in Table 3 and Table 4 for the NH and SH sites, respectively. As seen in Table 3, there is considerable variability in reported surface ocean Hg^0_{aq} concentrations in the North Atlantic and Arctic oceans. Our Mace Head- and Cabo Verde Observatory-based estimates (7.00 ± 0.21 pg L^{-1} and 4.00 ± 0.12 pg L^{-1}, respectively), which lie on the lower end of the reported range, are comparable to the North Atlantic concentrations from Kuss et al. (2011) (in spring, mean of ~ 4–5 pg L^{-1}) and Bowman et al. (2014) (10 ± 6 pg L^{-1}), as well as the non-ice-covered Arctic Ocean concentrations from DiMento et al. (2019) (6.42 ± 6.01 pg L^{-1}), for example. The estimates are rather low compared to the values reported for the Baltic Sea by Osterwalder et al. (2021) (13.5 ± 3.5 pg L^{-1}) and Wängberg et al. (2001) (~ 17 pg L^{-1}), and especially the Irish

west coast (~ 21 pg L^{-1}; Gårdfeldt et al., 2003), the western North Atlantic (mean values ranging between ~ 18 and 39 pg L^{-1}; Soerensen et al., 2013) and the Arctic Ocean by Andersson et al. (2008b) (44.13 ± 22.06 pg L^{-1}).

The relatively high concentrations reported for the Baltic Sea, Irish west coast and western North Atlantic (from Soerensen et al., 2013), for instance, are (near-)coastal measurements and may not be representative of the open ocean. In contrast, the air masses sampled at Mace Head and Cabo Verde Observatory spent most of their time over the open ocean, and thus our Hg^0_{aq} estimates reflect open ocean conditions. Coastal waters typically exhibit higher Hg concentrations than the open ocean due to river inputs, which have a much stronger impact in the coastal zone compared to the open ocean (Andersson et al., 2008b; Soerensen et al., 2013; Amos et al., 2014). Similarly, the Arctic measurements from Andersson et al. (2008b) are also not representative of the non-ice-covered open ocean, due to the capsulating effect of sea ice, which limits air–sea exchange, leading to the accumulation of Hg^0_{aq} in seawater (Andersson et al., 2008b; DiMento et al., 2019).

For the SH, in situ Hg^0_{aq} measurements are very limited. Nevertheless, for available measurements, our Cape Point (4.22 ± 0.21 pg L^{-1}) and Amsterdam Island (4.74 ± 0.16 pg L^{-1}) estimates are somewhat comparable to the values reported in the South Atlantic mid-latitudes in autumn (8 ± 3 pg L^{-1}, Kuss et al., 2011). The estimates also compare well to the Southern Ocean measurements reported for summer (7.0 ± 6.8 pg L^{-1}) and winter (9 ± 5 pg L^{-1}) by Nerentorp Mastromonaco et al. (2017) but are low compared to the summer Southern Ocean measurements from Wang et al. (2017) (24 ± 13 pg L^{-1}). Bratkič et al. (2016) report total column DGM measurements for the South Atlantic, with values seeming around 0–10 pg L^{-1} near the surface (see Figure 6 in Bratkič et al., 2016).

3.3.5 Estimation of ocean net Hg^0 evasion fluxes

We also used the observed relationship between Hg^0_{air} concentrations and air mass recent MBL residence time to estimate ocean net Hg^0 evasion fluxes. The estimates are derived using a simplified Lagrangian model describing the change in Hg^0 mixing ratio in an air parcel along a trajectory (Brasseur and Jacob, 2017). The detailed methodology is provided in Section A3, Appendix A.

Based on our calculations, we estimated a mean net evasion flux of 0.86 (95 % confidence interval, CI: 0.50–1.21), 0.56 (0.40–0.74), 0.87 (0.64–1.10) and 0.59 (0.50–0.68) ng m^{-2} h^{-1} for the oceanic airmass source regions for Mace Head, Cabo Verde Observatory, Cape Point and Amsterdam Island, respectively (Figure A3.1, Section A3). Presented in Table 3 and Table 4 are these estimates compared to reported values from the literature (calculated using in situ measurements of Hg^0_{air} and surface ocean Hg^0_{aq} concentrations) for the NH and SH sites, respectively.

As with the Hg^0_{aq} concentrations, there is a large variability in reported flux estimates in the North Atlantic and Arctic oceans, with mean evasion fluxes ranging from 0 to around 7 ng m^{-2} h^{-1}. Our Mace Head- and Cabo Verde Observatory-based estimates are comparable to values such as those reported for the Baltic Sea in winter (0.83 ng m^{-2} h^{-1}; Wängberg et al., 2001) and summer (0.6 ± 06, ng m^{-2} h^{-1}; Osterwalder et al., 2021), as well as the North Atlantic mid-latitudes (0.42 ± 0.36 ng m^{-2} h^{-1}, Andersson et al., 2011). The estimates are quite low compared to reported values in Irish west coast (2.7 ng m^{-2} h^{-1}; Gårdfeldt et al., 2003) and the western North Atlantic (mean values in the range of ~ 2–7 ng m^{-2} h^{-1}; Soerensen et al., 2013).

For the SH, there are only a few flux values in the literature (Table 4). The Cape Point- and Amsterdam Island-based mean estimates from our study are within the range of Southern Ocean values reported by Nerentorp Mastromonaco et al. (2017), which show marked seasonal variability (-0.2 ± 1.3, 0.4 ± 1.5 and 1.1 ± 1.6 ng m^{-2} h^{-1} in summer, winter and spring, respectively. The estimates are lower than the Southern Ocean value from Wang et al. (2017) (1.5 ± 1.8 ng m^{-2} h^{-1}).

Table 3: Reported surface ocean Hg^0_{aq} concentrations as well as Hg^0 air–sea exchange fluxes in the North Atlantic and Arctic oceans obtained from direct measurements, and the estimates from this study based on the relationship between mean Hg^0_{air} concentrations and air mass recent MBL residence time at Mace Head and Cabo Verde Observatory. For the fluxes, positive (negative) values indicate net evasion (deposition).

Location	Time period	Hg^0_{aq} concentration [pg L^{-1}][a, b]	Hg^0 exch. flux [ng m^{-2} h^{-1}][a, c]	Reference
Baltic Sea	2–15 Jul 1997	17.6	1.58	Wängberg et al. (2001)
Baltic Sea	2–15 Mar 1998	17.4	0.83	Wängberg et al. (2001)
Irish west coast	Sep 1999	21.4	2.7	Gårdfeldt et al. (2003)
Artic Ocean	13 Jul–25 Sep 2005	44.13 ± 22.06	-	Andersson et al. (2008b)

N. Atlantic midlatitudes	Nov 2008	16 ± 4	-	Kuss et al. (2011)
N. Atlantic subtropics	Nov 2008	10 ± 2	-	Kuss et al. (2011)
N. Atlantic midlatitudes	May 2009	4 ± 1	-	Kuss et al. (2011)
N. Atlantic subtropics	May 2009	5 ± 1	-	Kuss et al. (2011)
North Atlantic	7–11 Jul 2005	11.6 ± 2.0	0.42 ± 0.36	Andersson et al. (2011)
N.W. Atlantic	17–27 Aug 2008	32.1 ± 12.0	4.3 ± 3.4	Soerensen et al. (2013)
N.W. Atlantic	21–26 Sep 2008	25.7 ± 4.0	3.0 ± 2.9	Soerensen et al. (2013)
N.W. Atlantic	24–27 Jun 2009	24.0 ± 4.0	4.7 ± 3.7	Soerensen et al. (2013)
N.W. Atlantic	31 Aug–4 Sep2009	22.3 ± 2.8	2.1 ± 0.7	Soerensen et al. (2013)
N.W. Atlantic	29 Sep–7 Oct 2009	18.1 ± 4.8	2.2 ± 1.7	Soerensen et al. (2013)
N.W. Atlantic	4–9 Aug 2009	39.3 ± 6.8	6.8 ± 5.1	Soerensen et al. (2013)
N. Atlantic	Autumn 2010, 2011	10 ± 6[d]	-	Bowman et al. (2014)
Eastern N. Atlantic	Autumn 2010, 2011	9.4 ± 6.01[d]	0.60 ± 0.67	Mason et al. (2017)
Western N. Atlantic	Autumn 2010, 2011	11 ± 7.4[d]	1.23 ± 1.56	Mason et al. (2017)
Arctic Ocean	9–12 Oct 2015	6.42 ± 6.01[e]	0.4 ± 2.8[e]	DiMento et al. (2019)
Arctic Ocean	9–12 Oct 2015	20.26 ± 19.65[f]	2.8 ± 10.43[f]	DiMento et al. (2019)
Baltic Sea	10 May–20 Jun 2017	13.5 ± 3.5	0.6 ± 0.6	Osterwalder et al. (2021)
Mace Head	Feb 1996–Jan 2020	7.00 ± 0.21	0.86 (0.50–1.21)[g]	Present study
Cabo Verde Obs.	Dec 2011–Dec 2015	4.00 ± 0.12	0.57 (0.40–0.74)[g]	Present study

[a] Mean ± standard deviation (if standard deviation given), except for our flux estimates, where we report the mean and the upper and lower bounds of the 95 % confidence interval

[b] Some concentrations reported in ng m^{-3}, fM or pM, and converted here to pg L^{-1} as follows: 1 ng m^{-3} = 1 pg L^{-1}, 1 fM = 0.20059 pg L^{-1} and 1 pM = 200.59 pg L^{-1}.

[c] Some fluxes reported in ng m^{-2} d^{-1}, pmol m^{-2} h^{-1} or pmol m^{-2} d^{-1}, and converted here to ng m^{-2} h^{-1} as follows: 1 ng m^{-2} d^{-1} = 1/24 ng m^{-2} h^{-1}, 1 pmol m^{-2} h^{-1} = 0.20059 ng m^{-2} h^{-1} and 1 pmol m^{-2} d^{-1} = 0.20059/24 ng m^{-2} h^{-1}.

[d] Values from the same sampling campaign.

[e] Value in ice-free open waters; [f] value in contiguous ice-covered waters.

[g] Mean and the upper and lower bounds of the 95 % confidence interval of the mean.

Table 4: Similar Table 3, but for reported values in the South Atlantic and Southern oceans, and estimates from this study for Cape Point and Amsterdam Island. Here, all reported Hg^0_{aq} concentrations are surface ocean values except those marked with *, which are total column concentrations. For the fluxes, positive (negative) values indicate net evasion (deposition).

Location	Time period	Hg^0_{aq} conc. [pg L^{-1}][a, b]	Hg^0 exch. flux [ng m^{-2} h^{-1}][a]	Reference
S. Atlantic subtropics	Apr 2009	9 ± 2	-	Kuss et al. (2011)
S. Atlantic midlat.	Apr 2009	8 ± 3	-	Kuss et al. (2011)

S. Atlantic	24 Dec 2011–27 Jan 2012	45 ± 29*	-	Bratkič et al. (2016)
Southern Ocean	8 Jun–12 Aug 2013	9 ± 5	0.4 ± 1.5	N-Mastromonaco et al. (2017)
Southern Ocean	14 Aug–16 Oct 2013	12 ± 7	1.1 ± 1.6	N-Mastromonaco et al. (2017)
Southern Ocean	8 Dec 2010–14 Jan 2011	7 ± 6.8	-0.2 ± 1.3	N-Mastromonaco et al. (2017)
Southern Ocean	13 Dec 2014–1 Feb 2015	24 ± 13	1.5 ± 1.8	Wang et al. (2017)
Cape Point	Mar 2007–Dec 2017	4.22 ± 0.21	0.87 (0.64–1.10)[c]	Present study
Amsterdam Island	Jan 2012–Dec 2020	4.74 ± 0.16	0.60 (0.50–0.68)[c]	Present study

[a] Mean ± standard deviation (if standard deviation given), except for our flux estimates, where we report the mean and the upper and lower bounds of the 95 % confidence interval.

[b] Some concentrations reported in ng m^{-3} and converted here to pg L^{-1} as follows: 1 ng m^{-3} = 1 pg L^{-1}.

[c] Mean and the upper and lower bounds of the 95 % confidence interval of the mean.

3.3.6 Global extrapolation

By extrapolation of our site-specific flux results, we estimated a global mean evasion flux. For this, we assume that the mean of our Mace Head- and Cabo Verde Observatory-based estimates, 0.71 ng m^{-2} h^{-1} (95 % CI: 0.45–0.97 ng m^{-2} h^{-1}), is representative of the North Atlantic and Arctic oceans (combined area: ~ 57.048 million km^2), and the mean of the Cape Point- and Amsterdam Island-based estimates, 0.73 ng m^{-2} h^{-1} (0.57–0.89 ng m^{-2} h^{-1}), is representative of the Southern, South Atlantic and Indian oceans (~ 132.79 million km^2). For the Pacific Ocean (~ 168.723 million km^2), which is not covered by our observatories, we use the mean of the four estimates, 0.72 ng m^{-2} h^{-1} (0.51–0.93 ng m^{-2} h^{-1}). Under these assumptions, we obtain a global mean evasion flux of around 2270t y^{-1}, with a 95 % confidence interval of 1600–2900 t y^{-1}. This flux is rather small compared to recent model estimates, which range from 2800 to 4000 Hg^0 t y^{-1} (Horowitz et al., 2017; AMAP/UNEP, 2018; Outridge et al., 2018; Shah et al., 2021; Zhang et al., 2023), suggesting that net oceanic Hg^0 emission may currently be overestimated. Such an overestimation may relate to the parameterisation of the air–sea exchange velocity (e.g., Nightingale et al., 2000; McGillis et al., 2001) used in the models which is a large source of uncertainty (Zhang et al., 2019; Osterwalder et al., 2021).

That being said, our estimate is evidently subject to significant uncertainties, particularly due to the strong assumption that the results corresponding to individual sites and their oceanic areas of influence (see Figure 7) are somewhat representative of larger oceanic regions. In addition, back trajectories, on which our estimate is based, provide only a general indication of

air mass source regions, and are prone to large uncertainties from possible errors in input meteorological fields as well as numerical models (Yu et al., 2009).

3.4 Summary and conclusions

In this study, we combined long-term Hg^0_{air} observations with HYSPLIT air mass back trajectories at four ground-based monitoring sites, Mace Head and Cabo Verde Observatory in the NH, and Cape Point and Amsterdam Island in the SH, to study Hg^0 air–sea exchange. At all sites, we observed weak seasonal and diurnal Hg^0_{air} variations, even after filtering the data to extract observations representative of MBL conditions. This suggests that the weak variations reflect actual MBL dynamics and are not an artefact of the sampling of air masses of both oceanic and terrestrial origin.

We investigated the relationship between Hg^0_{air} concentrations and the recent residence time of air masses in the MBL. Our results showed a gradual increase in mean Hg^0_{air} concentration with air mass recent MBL residence time, followed by a steady state. The observed pattern is consistent with the thin film gas exchange model, which predicts net ocean Hg^0 emissions into the atmosphere until the Hg^0_{air} concentration normalised by the Henry's law constant matches the surface ocean Hg^0_{aq} concentration. This provides strong evidence that ocean Hg^0 emissions directly influence the observed Hg^0_{air} concentrations at the sites. Combined with the weak seasonal and diurnal variability at the sites, our findings suggest that recent air mass MBL residence time has a stronger influence on Hg^0_{air} concentrations in the MBL than seasonal and diurnal factors, such as solar radiation.

Using the relationship between mean Hg^0_{air} concentrations and air mass recent MBL residence time at the sites, we estimated surface ocean Hg^0_{aq} concentrations as well as ocean net Hg^0 evasion fluxes for the North Atlantic and Arctic oceans (AA) and the Southern, South Atlantic and south Indian oceans (SSI). The estimated Hg^0_{aq} concentration was in the range of ~ 4–7 pg L^{-1} for the AA and around 4 pg L^{-1} for the SSI, while the mean evasion flux was around 0.6–0.8 ng m^{-2} h^{-1} and 0.5–0.7 ng m^{-2} h^{-1} for the AA and SSI, respectively. Extrapolating the fluxes to the global scale, we derived a net global Hg^0 evasion flux of around 2270 t y^{-1} (95 % CI: 1600–2900 t y^{-1}). While this global estimate is based on strong assumptions and is subject to significant uncertainties, it suggests that current model estimates of net Hg^0 evasion flux

(2800–4000 Hg^0 t y^{-1}) may be too high. To improve the accuracy of the flux estimate, it is crucial to conduct longer term, higher frequency in situ measurements of Hg^0 air–sea exchange fluxes (as well as Hg^0_{aq} concentrations). These efforts are particularly crucial in the SH, where direct measurements are currently very sparse. Such comprehensive measurements would significantly improve our understanding and modeling of Hg cycling in the MBL.

The methodology applied here could be improved. In particular, the air mass back trajectories could be computed with higher spatially and temporally resolved meteorological input, if enough computational resources are available. However, while higher-resolution input data could provide more accurate insights into the sources and travel paths of air masses, a relatively low-resolution input data (NCEP/NCAR Reanalysis) was chosen here considering the large number of trajectories (e.g., every hour between 1996 and 2020 for Mace Head) which had to be computed for the study.

While the results of this paper are subject to significant uncertainties, our study demonstrates the applicability of ground-based Hg^0_{air} observations, where the currently available measurements span multiple years, in studying air–sea exchange as well constraining surface ocean Hg^0_{aq} concentrations and net ocean Hg^0 evasion fluxes.

Chapter 4 – Constraining the influence of sea surface temperature and aquatic primary productivity on gaseous elemental mercury air–sea exchange using ground-based atmospheric observations

This chapter is based on the following paper, which is in preparation for submission:

Koketso M. Molepo, Ian M. Hedgecock, Alkuin M. Koenig, Francesco Carbone, Ralf Ebinghaus, Aurelien Dommergue: Constraining the influence of sea surface temperature and aquatic primary productivity on gaseous elemental mercury air–sea exchange using ground-based atmospheric observations. *In preparation for submission*

Abstract

Air–sea exchange of gaseous elemental mercury (Hg^0) plays a pivotal role in the global mercury (Hg) biogeochemical cycle, yet the mechanisms driving this exchange remain poorly understood. This study examines the potential influence of sea surface temperature (SST) and surface ocean primary productivity on atmospheric Hg^0 (Hg^0_{air}) concentrations in the marine boundary layer, assuming a direct link between the concentrations and Hg^0 air–sea exchange fluxes. We analyse 12 years of Hg^0_{air} measurements at Mace Head, Ireland, together with SST observations and satellite-retrieved surface ocean chlorophyll-*a* concentrations, the latter representing primary productivity, and examine relationships across different temporal scales. At the diurnal and seasonal scales, Hg^0_{air} concentrations were inversely related to SSTs, contrary to expected evasion enhancement with warmer waters, suggesting that, on a large scale, SST-driven emission increases are minor or are masked by concurrent processes such as vegetation uptake or phytoplankton uptake. No meaningful Hg^0_{air}–SST relationships were observed at the interannual scale. Hg^0_{air} showed a strong inverse relationship with surface ocean primary productivity at seasonal and interannual scales, consistent with enhanced phytoplankton Hg^0_{air} uptake or surfactant-mediated evasion suppression with high

productivity. However, at the seasonal scale, a similarly strong anticorrelation was observed with NDVI, in line with previously established vegetation uptake control on northern hemispheric Hg^0_{air} seasonality. Moreover, no correlation was observed between seasonal Hg^0_{air} and chlorophyll-*a* at Cape Point in the southern hemisphere, casting doubt on the seasonal aquatic primary productivity influence at Mace Head. On the other hand, at Cape Point, annual mean Hg^0_{air} concentrations were also inversely related to chlorophyll-*a*, supporting the interannual link between Hg^0_{air} and aquatic primary productivity. We also observe that, while the long-term Hg^0_{air} decline at Mace Head is likely linked to vegetation uptake, interannual variability may be related to oceanic productivity. These findings highlight surface ocean primary productivity as a key modulator of Hg^0_{air} air–sea exchange on interannual scales, a driving factor that has so far been largely overlooked.

4.1 Introduction

Understanding the dynamics of mercury (Hg) in different environmental compartments is crucial to constraining the global Hg biogeochemical cycle. At the air–sea interface, the exchange of gaseous elemental Hg (Hg^0) plays a pivotal role in determining the fate and distribution of Hg in the environment. Atmospheric deposition, as the dominant source of Hg (Hg^0, plus divalent Hg, Hg^{II}) to the oceans, significantly influences concentrations of marine Hg (Strode et al., 2007; Horowitz et al., 2017; AMAP/UNEP, 2018; Zhang et al., 2019, 2023; Jiskra et al., 2021; Shah et al., 2021). Conversely, a large portion of the deposited Hg is re-emitted back to the atmosphere (as Hg^0), with ocean emissions estimated to contribute roughly one-third to the total annual atmospheric Hg burden (Horowitz et al., 2017; AMAP/UNEP, 2018; Zhang et al., 2019; Shah et al., 2021). Through this recurrent deposition and re-emission, ocean emissions prolong the residence time of Hg in the environment (Strode et al., 2007; Amos et al., 2013). On the other hand, reduction of dissolved Hg^{II} to Hg^0 in seawater and its subsequent evasion to the atmosphere decreases the pool of Hg^{II} available in the surface ocean for transformation to the neurotoxic methylmercury (Lehnherr, 2014).

Despite its significance in global Hg cycling, Hg^0 air–sea exchange remains poorly constrained, due to limited direct observations as well as an incomplete understanding of the environmental parameters influencing this process (Zhang et al., 2019; Osterwalder et al., 2021; Li et al., 2024; Dastoor et al., 2025). In this context, we aim to gain a better understanding of Hg^0 air–sea exchange using long-term atmospheric Hg^0 (Hg^0_{air}) observations from ground-based coastal

monitoring sites. We infer Hg^0 air–sea exchange from patterns observed in the observations and their relation to environmental factors.

Sea surface temperature (SST) is one of the key variables thought to strongly influence Hg^0 air–sea exchange (e.g., Andersson et al., 2008; Soerensen et al., 2013; Osterwalder et al., 2021). Higher SSTs not only enhance microbial reduction of Hg^{II} to Hg^0 (Soerensen et al., 2013; Lee and Fisher, 2019), but also increase the diffusivity of Hg^0 in seawater, both of which promote evasion. Observational studies have reported positive relationships between Hg^0_{air} concentrations in the marine boundary layer (MBL) and SSTs. For example, Bieser et al. (2020) observed that elevated Hg^0_{air} concentrations at Cape Point were associated with air masses from the warm Agulhas Current, while Carbone et al. (2016) found a positive correlation between Hg^0_{air} concentrations at Mauna Loa Observatory and SSTs over the Pacific Ocean. In the northern Adriatic Sea, Floreani et al. (2019) reported significantly higher Hg^0 evasion fluxes in summer compared to autumn and winter, coinciding with increased SSTs. While these studies indicate SST as a positive driver of evasion, no prior work, to our best knowledge, has systematically assessed its influence on Hg^0_{air} air–sea exchange and the resultant variability in Hg^0_{air} concentrations across different time scales using long-term datasets.

Another potentially important, yet underexplored, driver of Hg^0 dynamics in the MBL is surface ocean primary productivity. Aquatic primary producers, which contribute ~ 50 % of the annual global primary productivity (Field et al., 1998), can influence Hg cycling in the marine environment through several mechanisms. For example, laboratory studies show that phototrophs and their exudates can reduce Hg^{II} to Hg^0 (Grégoire and Poulain, 2014 and references therein; Liang et al., 2022), thereby promoting evasion. On the other hand, recent experimental work (Santos et al., 2024) suggests that phytoplankton may also sequester Hg^0_{air}, acting as a net sink. In addition, accumulation of biological surfactants in the surface ocean microlayer, which are derived largely from phytoplankton and their exudates (Tsa and Liu, 2003), can form a physicochemical barrier that suppresses air–sea gas exchange (e.g., Tsa and Liu, 2003; Pereira et al., 2018; Li et al., 2024). Despite these opposing mechanisms, the net role of surface ocean primary productivity in modulating Hg^0_{air} concentrations in the MBL has not been extensively explored.

In this study, we investigate the potential influence of SST and surface ocean primary productivity on Hg^0_{air} concentrations in the MBL, assuming a direct link between Hg^0_{air} concentrations and air–sea exchange. We analyse 12 years (2008–2019) of Hg^0_{air} measurements from Mace Head, a coastal monitoring station on the Irish west coast that primarily samples clean North Atlantic air masses. SST data are obtained from the Irish Marine Data Buoy Observation Network (IMDBON), and MODIS-Aqua surface ocean chlorophyll-*a* concentrations are used to represent sea surface primary productivity. By examining relationships between Hg^0_{air} concentrations and these variables across different time scales, this work aims to improve understanding of how these oceanic parameters modulate Hg^0 air–sea exchange.

4.2 Data and methods

4.2.1 Study area

The study mainly uses Hg^0_{air} observations from the Mace Head atmospheric research station on the west coast of Ireland. Relationships are examined between the observations and SSTs measured from offshore buoys located along the Irish coast, as well as satellite-retrieved surface ocean chlorophyll-*a* concentrations averaged over the North Atlantic Ocean. Figure 8 shows the locations of Mace Head and the observational buoys, as well as the spatial domain over which the chlorophyll-*a* data were averaged.

4.2.2 Datasets

4.2.2.1 Hg measurements at Mace Head

Mace Head (53°20′ N, 9°54′ W) is located in County Galway on the west coast of Ireland (Figure 8). The site is exposed to the North Atlantic Ocean with a wide clean sector between 180° and 300° (Ebinghaus et al., 2011), making it ideal to study atmospheric composition under northern hemispheric background conditions but also under regionally polluted European continental conditions when air masses originate from the east (Ebinghaus et al., 2011). On average, over half of the air masses sampled at Mace Head originate within the clean sector, having recently travelled thousands of kilometres across the North Atlantic Ocean (Ebinghaus et al., 2011; Molepo et al., accepted). The site experiences a mild, moist climate, with an average air temperature of about 10 °C, generally high relative humidity (80–85 %) and annual

rainfall of about 1200 mm (www.macehead.org, last access: June 2022). Air is sampled from a 10 m a.gl. tower situated 100 m from the shoreline and 50 m from the high-water mark. The nearest major urban area, Galway city, is located approximately 90 km to the east of Mace Head, and there are no nearby industrial activities influencing measurements at the site (Ebinghaus et al., 2011). Mace Head is operated by the Atmospheric Science Research Group at the National University of Ireland (Kock et al., 2005), and is part of several international research networks including the Global Mercury Observation System (GMOS) and the World Meteorological Organisation's (WMO) Global Atmosphere Watch Programme (GAW).

Since September 1995, atmospheric Hg measurements have been carried out at Mace Head using a Tekran Model 2537 A/B analyser (Tekran Inc., Toronto, Canada). As described in detail in Molepo et al. (accepted), the analyser operates via Hg enrichment on a gold cartridge, followed by thermal desorption and detection by cold vapour atomic fluorescence spectroscopy (CVAFS) at 253.7 nm (Fitzgerald and Gill, 1979; Bloom and Fitzgerald, 1988). The instrument features two gold cartridges, switching between them to allow for alternating sampling and desorption, resulting in continuous sampling of the incoming air. The instrument is operated with a 15 min temporal resolution, reporting concentrations in nanograms per cubic metre at standard temperature and pressure (STP) conditions (273.15 K and 1013.25 hPa), and has a detection limit of around 0.1 ng m^{-3}. In this study, we used the Hg measurements aggregated into hourly averages. Automated calibration of the analyser occurs every 25 hours using an internal permeation source. The internal permeation source is in turn validated ~ every 6 months using manual injection of saturated Hg vapour from a temperature-controlled vessel adapted following the Dumarey et al. (1985) procedures. Further information on the sampling procedure, including quality assurance and quality control measures in operation at Mace Head, are detailed in other studies (e.g., Ebinghaus et al., 2011; Weigelt et al., 2015).

Some studies refer to the Tekran 2537A/B measurements at Mace Head as total gaseous mercury (TGM; TGM = Hg^0_{air} + gaseous oxidised mercury, Hg^{II}_{air}) (e.g., Andersson et al., 2011; Ebinghaus et al., 2011; Custódio et al., 2020, 2022). However, the measurements are most likely of Hg^0_{air} rather than TGM, as Hg^{II}_{air} is easily lost to sea-salt deposits in the inlet tubing and filters of the instrument (Weigelt et al., 2015). Moreover, TGM typically comprises mostly (> 98 %) Hg^0_{air} (e.g., Soerensen et al., 2010a; Yin et al., 2018; Wang et al., 2019).

Therefore, we refer to the Tekran 2537A/B measurements at Mace Head as Hg^0_{air} and do not distinguish between TGM and Hg^0_{air}, including when citing other studies.

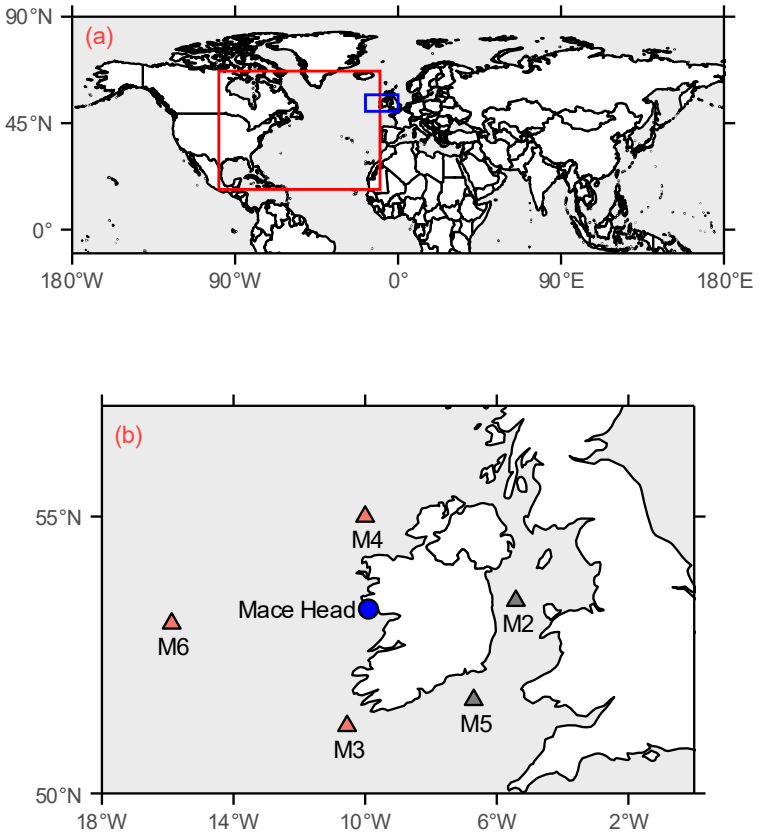

Figure 8: Visualisation of the study area. (a) The red box shows the spatial domain (North Atlantic Ocean; 99° W–10° W, 17° N–67 °N) over which the surface ocean chlorophyll-*a* concentrations were averaged to generate a monthly mean time series. The blue box encompasses the domain shown in panel (b). (b) Locations of Mace Head (blue circle) and the IMDBON buoys (triangles). The study primarily uses SSTs measured at buoys M6, M4 and M3 (triangles in red).

4.2.2.2 SST observations

SST data were obtained from the Irish Marine Data Buoy Observation Network (IMDBON; www.marine.ie, last access: February 2025), which consists of five offshore observation buoys deployed around the Irish coast (Figure 8). Operating since 2001, the network provides hourly mean values of several meteorological and oceanographic variables including air temperature, relative humidity, wind speed, wind direction, SST and wave height (www.marine.ie). The network is managed by the Irish Marine Institute in collaboration with Met Éireann and the UK Met Office, and is part of WMO's Global Telecommunications System (www.marine.ie).

In this study, we primarily use SST data from buoys M6, M4 and M3, located west, northeast and southwest of Mace Head, respectively (Figure 8(b)). Where SST data from the other two buoys (M2 and M5) are used, this is explicitly stated.

4.2.2.3 Sea surface chlorophyll-*a* concentrations

To assess the potential influence of surface ocean primary productivity on Hg^0_{air} concentrations at Mace Head, we used surface ocean chlorophyll-*a* concentration data from the Moderate Resolution Imaging Spectroradiometer (MODIS) aboard NASA's Aqua satellite (NASA, 2022). Chlorophyll-*a* concentration is widely used as a proxy for ocean primary productivity (e.g., Wernand et al., 2013; Ye et al., 2015; Gregg and Rousseaux, 2019). The data were originally obtained from NASA's Ocean Biology Processing Group (OBPG; https://oceandata.sci.gsfc.nasa.gov) and further processed and distributed by the Integrated Climate Data Center (ICDC), Centre for Earth System Research and Sustainability (CEN), Universität Hamburg, Germany (https://www.cen.uni-hamburg.de/icdc; last access: April 2025).

The ICDC-processed dataset, spanning the period September 2002–July 2024, were provided in daily NetCDF files with a global coverage at spatial resolution of ~ 4.63 km × 4.63 km (https://www.cen.uni-hamburg.de/icdc). From this dataset, we generated a daily mean surface ocean chlorophyll-*a* concentration time series by spatially averaging the data over the North Atlantic Ocean (99° W–10° W, 17° N–67 °N; see Figure 8(a)).

4.2.2.4 NDVI

While this study focuses on sea surface parameters, it is important to consider terrestrial vegetation photosynthetic activity when examining temporal Hg^0_{air} variability at northern hemispheric midlatitudes, due to its proposed strong influence via vegetation Hg^0_{air} uptake (e.g., Jiskra et al., 2018; Feinberg et al., 2022). To represent terrestrial vegetation activity, we used normalised difference vegetation index (NDVI; e.g., Jiskra et al., 2018; Fu et al., 2019; Ballabio et al., 2021) data derived from the MODIS instrument aboard NASA's Terra satellite (Didan, 2021). The data, originally from the Land Processes Distributed Active Archive Center (LP DAAC), was also processed and distributed by the ICDC (https://www.cen.uni-hamburg.de/en/icdc/data/land/modis-vegetationindex.html; last access: June 2025).

The ICDC data, which were provided as global monthly means in NetCDF format, have a spatial resolution of 0.05° × 0.05° and span the period from 2000 to 2024. For this study, we averaged the NDVI values over the entire northern hemisphere (~180° W–180° E, 0°–90 °N) to generate a monthly mean time series.

4.2.3 Air mass back trajectories

To estimate the origin of air masses arriving at Mace Head, we use the same HYSPLIT (Hybrid Single-Particle Lagrangian Integrated Trajectory; Stein et al., 2015) air mass back trajectories from Molepo et al. (accepted). Briefly, for each hourly Hg^0_{air} observation, a 144-hour (i.e., 6-day) air mass back trajectory starting at 50 m above model ground level was computed, using the National Centers for Environmental Prediction/National Center for Atmospheric Research (NCEP/NCAR) reanalysis data (Kalnay et al., 1996) for model input. The reanalysis data has a spatial resolution of 2.5° and a temporal resolution of 6 hours.

4.2.4 Data treatment

4.2.4.1 Hg^0_{air} data filtering

While Mace Head predominantly receives clean marine air masses, the site is also influenced by anthropogenic pollution from continental Europe (e.g., Ebinghaus et al., 2002, 2011; Custodio et al., 2022; Molepo et al., accepted). This influence can obscure natural signals in the Hg^0_{air} record, such as those associated with oceanic Hg^0 evasion (e.g., Molepo et al.,

accepted). To assess the influence of anthropogenic emissions, we generated a clean sector (filtered) Hg^0_{air} dataset, following an approach similar to Ebinghaus et al. (2002), who defined the clean sector as the wind sector between 180° and 300°. In the present study, we used the air mass back trajectories (Section 4.2.3) to identify clean sector observations: an hourly data point was classified as a clean sector observation if the corresponding back trajectory remained within the 180°–300° sector over the full 6-day travel time.

Generally, we did not observe substantial differences between the analyses performed with the filtered vs unfiltered data. Therefore, we present and discuss results based on the unfiltered Hg^0_{air} data. Where the filtered dataset is used, this is explicitly stated.

4.2.4.2 Hg^0_{air} and NDVI detrending

We also generated time series of detrended Hg^0_{air} and NDVI over the study period (2008–2012; see Section 4.3.4.3 below), both of which exhibit long-term linear trends (downward for Hg^0_{air} and upward for NDVI; see Figure 9). Detrending was performed by fitting a linear model of each variable as a function of time (in seconds since the start of the dataset) and then subtracting the linear trend from the original data.

As well, we present mainly the analyses with the original (non-detrended) datasets and explicitly state where detrended data are used.

4.2.4.3 Study period selection and calculation of temporal averages

Due to differences in the temporal coverage of the datasets (for example, the Mace Head Hg^0_{air} data were available from February 1996 to January 2020, whereas the M6 and M3 SST records were available from September 2006 and May 2007 onwards, respectively), the study period was limited to January 2008–December 2019 for consistent data coverage across the variables. Although data are available from May 2007 for all variables, 2007 data were discarded to ensure comparable (i.e., calculated with January–December data) annual mean values within each dataset.

From the datasets, we calculated diurnal, monthly, seasonal and annual averages (diurnal averages were computed only for Hg^0_{air} and SST). Note that here, "monthly" refers to

individual calendar months within each year (e.g., January 2008, February 2008, etc.), while "seasonal" refers to multi-year (i.e., long-term) averages for each month (i.e., the average of all Januaries from 2008 to 2019, etc.).

The original time series over the analysis period, including their summary statistics, are presented in Figure 9.

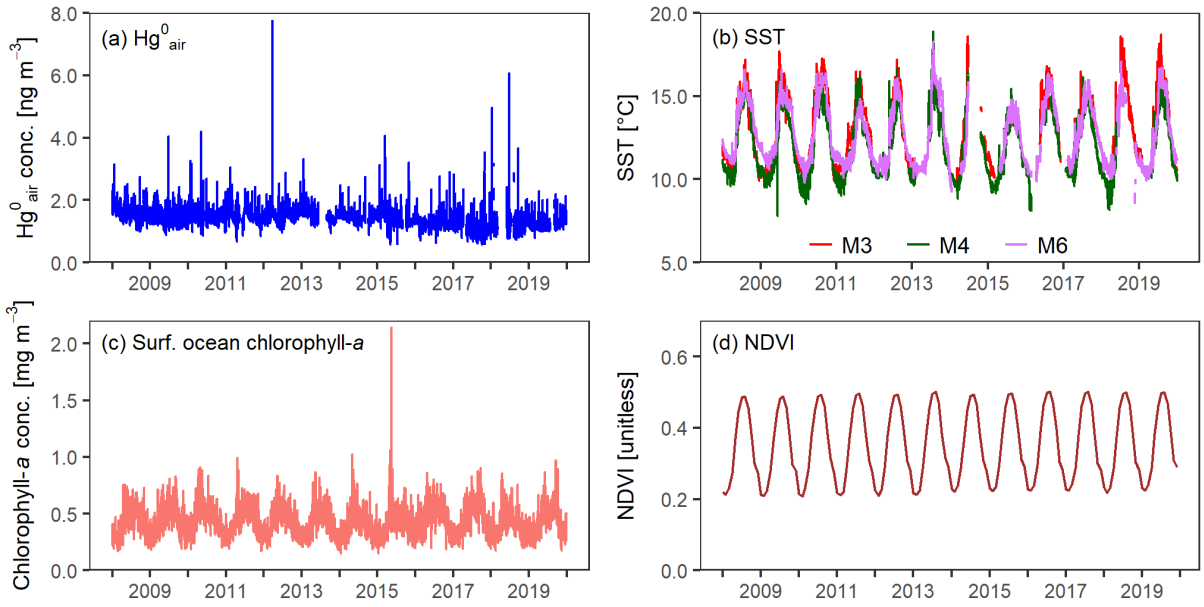

(e)

Variable [unit]	Resolution	Mean ± std. dev. (range)	No. of data points	Perc. data coverage [%]
Hg^0_{air} [ng m^{-3}]	Hourly	1.39 ± 0.21 (0.55–8.19)	88 603	84
M3 SST [°C]	Hourly	12.99 ± 2.12 (9.50–19.73)	63 788	60
M4 SST [°C]	Hourly	11.91 ± 1.83 (7.80 18.93)	82 235	78
M5 SST [°C]	Hourly	12.69 ± 1.78 (8.50–18.30)	84 343	80
Chl-*a* conc. [mg m^{-3}]	Daily	0.43 ± 0.14 (0.15–2.14)	4 383	100
NDVI [unitless]	Monthly	0.35 ± 0.10 (0.21–0.50)	145	100

Figure 9: Overview of the main datasets used in the study over the analysis period (January 2008 and December 2019). (a) Hourly mean Hg^0_{air} concentrations at Mace Head, (b) hourly mean SSTs measured at buoys M3, M4 and M6, (c) daily mean surface ocean chlorophyll-*a* concentrations over the North Atlantic and (d) monthly mean NDVI averaged over the northern hemisphere. (e) Summary of the datasets, showing the mean, standard deviation (std. dev.), total number of data points (per temporal resolution) and percentage data coverage (i.e., proportion of valid or non-missing) over the analysis period.

4.2.5 Statistical analysis

All analyses were conducted using the *R* programming language (R Core Team, 2024). Most of the data processing was performed with packages from *tidyverse* (Wickham et al., 2019), in particular *dplyr*. All figures, including maps, were created with the *ggplot2* package (Wickham, 2016). Correlations were computed using the *corr.test* function within the *psych* package (Revelle, 2025), while cross-correlations were computed with the base *R* function *ccf* (R Core Team, 2024).

4.3 Results and discussion

4.3.1 Overview of Hg^0_{air} concentrations at Mace Head

Between January 2008 and December 2019, hourly mean Hg^0_{air} concentrations at Mace Head averaged 1.39 ± 0.21 ng m^{-3} (mean ± standard deviation), ranging between 0.55 and 8.19 ng m^{-3} (Figure 9(a)). The mean seasonal and diurnal Hg^0_{air} variability at the site (Figure B1.1(a) and Figure B1.1(b), respectively, Appendix B) have been described in previous studies (e.g., Ebinghaus et al., 2002; Jiskra et al., 2018; Custódio et al., 2022; Molepo et al., accepted). Briefly, the concentrations are on average higher in winter (December–April, averaging 1.44 ± 0.22 ng m^{-3} for 2008 to 2019) than in summer and spring (May–November, 1.35 ± 0.19 ng m^{-3}), similar to other ground-based and cruise-based measurements in the northern hemisphere (e.g., Temme et al., 2003; Soerensen et al., 2010a, 2014; Xia et al., 2010; Sprovieri et al., 2016; Custódio et al., 2022). Proposed explanations for this pattern include increased anthropogenic emissions from fossil-fuel combustion for heating in winter (Ebinghaus et al., 2002; Lan et al., 2012), increased vegetation Hg^0_{air} uptake in summer (Jiskra et al., 2018; Feinberg et al., 2022) as well as higher North Atlantic Ocean Hg^0 emissions in winter (Soerensen et al., 2010b). The diurnal variability is rather weak, with the daily mean minimum and maximum values representing a less than 2 % change from the overall mean, consistent with other studies that have reported negligible mean Hg^0_{air} diurnal variability in the MBL in the open ocean (e.g., Soerensen et al., 2010a; Wang et al., 2017; Wang et al., 2019; Molepo et al., accepted).

Annual mean concentrations show a decreasing trend (–0.033 ng m^{-3} y^{-1} over our analysis period; Figure B1.1(c)), in line with observations at other northern hemisphere sites (e.g., Cole

et al., 2014; Marumoto et al., 2019; Custódio et al., 2022; Feinberg et al., 2024). The downward trend has been attributed to decreased global anthropogenic emissions (Zhang et al., 2016; Feinberg et al., 2024), increased terrestrial net primary productivity (Jiskra et al., 2018) and reduced emissions from the North Atlantic due to declining subsurface Hg concentrations (Soerensen et al., 2012).

While anthropogenic emissions and terrestrial vegetation activity may contribute to the temporal Hg^0_{air} variability at Mace Head, other lines of evidence suggest an important role of Hg^0 air–sea exchange with the North Atlantic Ocean (e.g., Soerensen et al., 2010b, 2012). However, the role of surface ocean parameters such as SST and primary productivity in modulating this exchange has not been thoroughly explored. In the following sections, we examine how SST and surface ocean primary productivity in the North Atlantic may contribute to the temporal variability in Hg^0_{air} concentrations at Mace Head, assuming a direct link between Hg^0_{air} concentrations and Hg^0 air–sea exchange.

4.3.2 Hg^0_{air} relationships with SST and surface ocean primary productivity

4.3.2.1 Hg^0air and SST

Figure 10, Figure 11(a) and Figure 12(a) show the diurnal, seasonal and annual mean Hg^0_{air} concentrations at Mace Head, respectively, together with SSTs measured at buoys M3, M4 and M6 along the Irish coast. At both the diurnal- and seasonal-scales (Figure 10 and Figure 11(a), respectively), the Hg^0_{air} concentrations are strongly anticorrelated with SSTs across all buoys (R = −0.83, −0.92 and −0.86 with M3, M4 and M6 SSTs, respectively, at the diurnal scale; R = −0.68, −0.73 and −0.72 with M3, M4 and M6 SSTs, respectively, at the seasonal scale; $p <$ 0.05 in all cases). This observation is counterintuitive, considering current understanding of Hg^0–SST dynamics in the MBL. Warmer waters generally enhance the microbial reduction of Hg^{II} to Hg^0 (Soerensen et al., 2013; Lee and Fisher, 2019), which increases surface ocean Hg^0 concentrations and induces Hg^0 evasion. Additionally, higher SSTs increase the diffusivity and decrease the solubility of Hg^0 in seawater, both of which further promote evasion. Indeed, studies conducted at other locations have reported positive relationships between MBL Hg^0_{air} concentrations and SSTs, for example, Bieser et al. (2020) at Cape Point in the Southern Ocean, Carbone et al. (2016) at Mauna Loa Observatory in the Pacific Ocean and Floreani et al. (2019) in the northern Adriatic Sea, as previously mentioned.

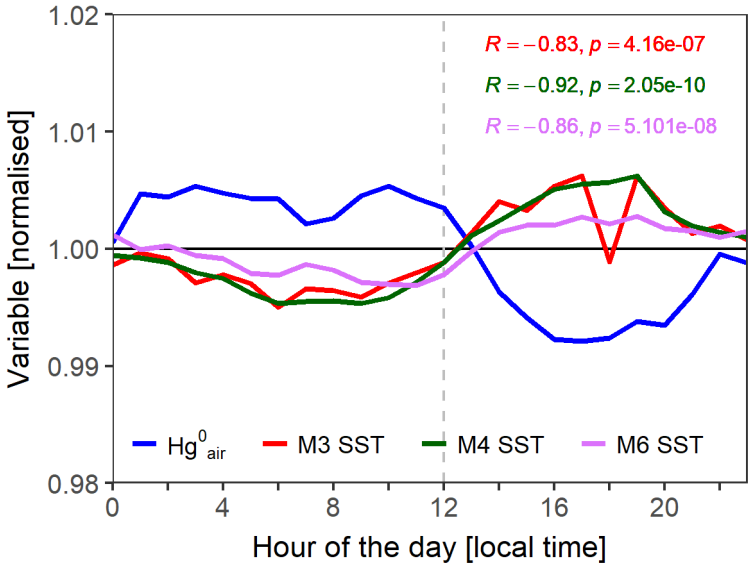

Figure 10: Normalised mean diurnal variation in Hg^0_{air} concentration at Mace Head and SST at buoys M3, M4 and M6 for the period 2008–2019. The horizontal line represents the normalised mean value (i.e., 1 ng m^{-3} for Hg^0_{air} concentration and 1 °C for SST); actual (non-normalised) mean values are provided in the table in Figure 9. The dashed vertical line is plotted along 12:00 local time. Pearson correlation coefficients (*R*) and associated *p*-values (*p*) between Hg^0_{air} and SST at each buoy are shown on the top right, with colours matching the corresponding SST time series (red for M3, dark green for M4 and light green for M6).

Inspection of diurnal-scale Hg^0_{air}–SST cross-correlations considering M2, M4 and M6 SSTs reveals an east-to-west pattern in correlation strength, with peak anticorrelation occurring at different time lags depending on buoy position relative to Mace Head (Figure 13). The negative Hg^0_{air}–SST correlation is strongest with M2 (east of Mace Head), M4 (similar longitude) and M6 (west) SSTs at a lag of −2, 0 and +1 hours, respectively. This pattern, as well as the strong inverse relationship with the SSTs, indicates that the mean diurnal Hg^0_{air} variation is more strongly influenced by other solar radiation-enhanced processes than by SST-induced evasion. The strong anticorrelation with SSTs at the seasonal scale also suggests the influence of other solar radiation-driven processes. Such processes could include Hg^0_{air} uptake by terrestrial vegetation (e.g., Jiskra et al., 2018; Feinberg et al., 2022) and photooxidation. Indeed, we find a strong negative correlation between the seasonal mean Hg^0_{air} concentrations and NDVI averaged over the northern hemisphere (Figure 11(b); $R = -0.72$, $p < 0.05$). Without higher

resolution NDVI data, it is difficult to determine whether terrestrial vegetation uptake is also a key driver of the mean diurnal Hg^0_{air} variability.

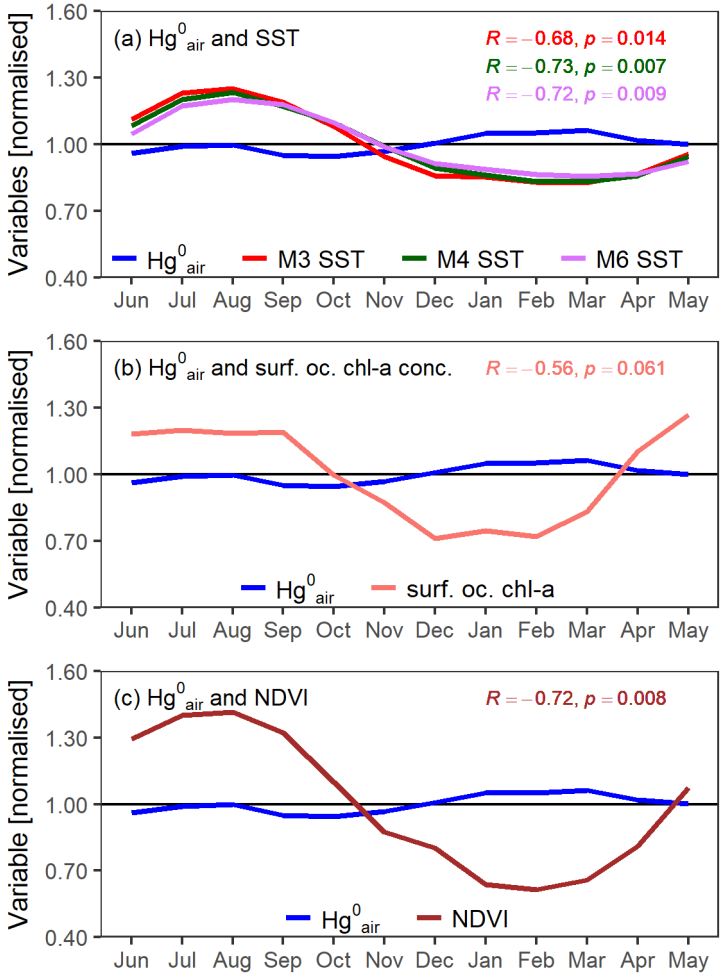

Figure 11: Normalised mean seasonal variation in Hg^0_{air} concentration at Mace Head along with (a) SST at buoys M3, M4 and M6 and (b) surface ocean chlorophyll-*a* concentration over the North Atlantic Ocean and (c) NDVI over the northern hemisphere. The horizontal line in each panel represents the normalised mean value (i.e., 1 ng m^{-3} for Hg^0_{air} concentration, 1 °C for SST and 1 mg m^{-3} for chlorophyll-*a* concentration; NDVI is unitless); actual (non-normalised) mean values are shown in the table in Figure 9. Pearson correlation coefficients (*R*) and associated *p*-values (*p*) between Hg^0_{air} and the variables are shown on the top right, with colours matching the corresponding time series. The months have been ordered starting in June, such that the seasonal cycle starts in summer and ends in spring.

The hypothesis that vegetation uptake is a major driver of diurnal Hg^0_{air} variability at northern hemispheric midlatitudes has been proposed by Jiskra et al. (2018). However, we do not believe that this is the case at Mace Head for two reasons. (i) In our previous study (Molepo et al., accepted), we showed that the amplitude of the mean diurnal cycle at Mace Head is not only low but also exhibits little seasonal variation (see Figure A1.3 here, Appendix A). If vegetation uptake were the main driver, strong seasonal differences would be expected due to higher uptake rates in summer than in winter. (ii) The amplitude of the mean diurnal variation at Mace Head is similar to that observed at Cape Point and Amsterdam Island in the southern hemisphere (Molepo et al., accepted; Figure A1.3). Jiskra et al. (2018) argue that vegetation uptake is much weaker in the southern hemisphere compared to the northern hemisphere, which they suggest explains the more pronounced seasonal Hg^0_{air} variability in the northern hemisphere vs the southern hemisphere. Based on this, it would be expected that the diurnal variation magnitude at Mace Head exceeds that in the southern hemisphere, particularly in summer, when vegetation uptake rates are highest, which is not the case. These observations make it unlikely that vegetation uptake is the dominant factor controlling the diurnal cycle at Mace Head.

Regarding redox chemistry, our previous study (Molepo et al., accepted) also derived a mean net Hg^0_{air} oxidation rate in the MBL, using chemical transport model results from Shah et al. (2021). Here, applying this rate, 2.5×10^{-4} h^{-1}, we assessed whether oxidation alone could account for the observed mean diurnal Hg^0_{air} variation at Mace Head, by comparing the expected decrease in concentration due to oxidation with the observed decrease. We focus on the 7-hour window from the late morning peak (at 10:00) to the afternoon minimum (17:00), during which the observed mean Hg^0_{air} concentration declines from 1.395 ng m^{-3} to 1.377 ng m^{-3}, a decrease of 0.018 ng m^{-3} (Figure B1.1(b)). Assuming exponential decay due to oxidation, the expected concentration decrease is calculated as:

$$c(t) = c_0 . e^{-kt}, \quad (5.1)$$

where *c(t)* is the Hg^0_{air} concentration after time *t*, c_0 the initial concentration (the 10:00 maximum, 1.395 ng m^{-3}), *k* the oxidation rate (2.5×10^{-4} h^{-1}) and *t* the time (7 hours). This yields a concentration of 1.393 ng m^{-3}, a decrease of only 0.0024 ng m^{-3}. Compared to the

observed decrease (0.018 ng m^{-3}), the expected decline from oxidation loss is approximately eight times smaller. Although Eq. (5.1) is an oversimplification and neglects concurrent processes and replenishment (e.g., oceanic evasion), it nonetheless provides an upper-limit estimate of oxidation-driven loss. Even under this assumption, the oxidation-driven decline is insufficient to account for the observed decrease, indicating that additional processes are involved. Similarly, at the seasonal scale redox chemistry alone has been deemed insufficient to explain observed Hg^0_{air} variability (e.g., Jiskra et al., 2018; Feinberg et al., 2022).

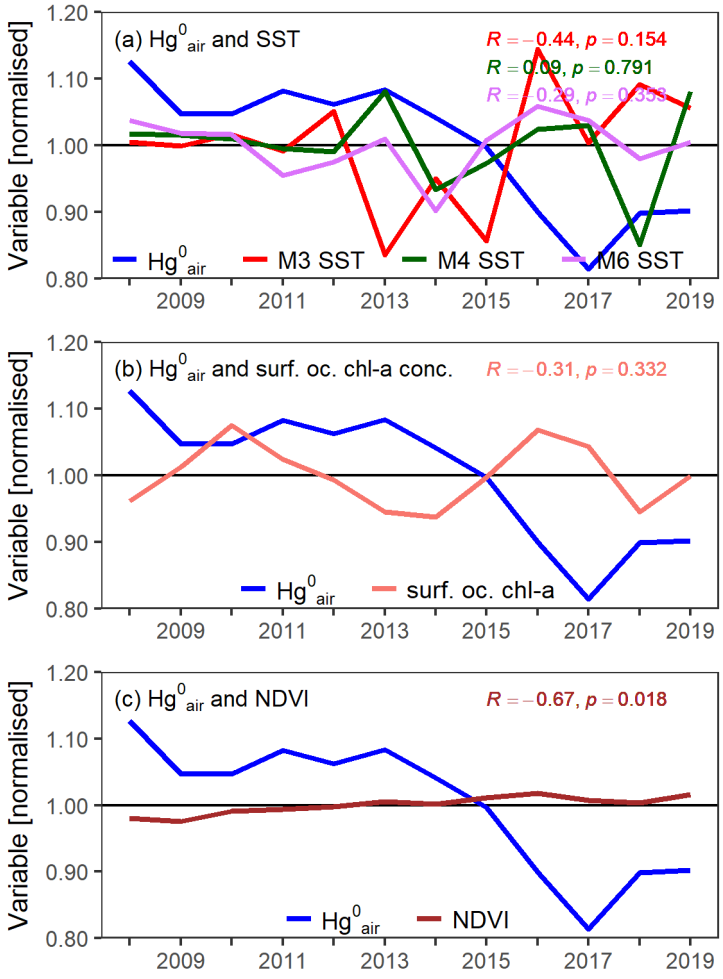

Figure 12: Normalised mean annual variation in Hg^0_{air} concentration at Mace Head along with (a) SST at buoys M3, M4 and M6 and (b) surface ocean chlorophyll-*a* concentration over the North Atlantic Ocean

and (c) NDVI over the northern hemisphere. The horizontal line in each panel represents the normalised mean value (i.e., 1 ng m^{-3} for Hg^0_{air} concentration, 1 °C for SST and 1 mg m^{-3} for chlorophyll-*a* concentration; NDVI is unitless); actual (non-normalised) mean values are shown in the table in Figure 9. Pearson correlation coefficients (*R*) and associated *p*-values (*p*) between Hg^0_{air} and each dataset are shown on the top right, with colours matching the corresponding time series.

To decouple the strong seasonal influence of vegetation uptake, we also assessed the Hg^0_{air}–SST relationships using deseasonalised monthly mean values, that is, with the long-term monthly means (i.e., seasonal cycle) subtracted from the original time series. These results showed no meaningful relationships between monthly mean Hg^0_{air} concentrations and SSTs (not shown).

For annual means, Hg^0_{air} exhibits weak and statistically insignificant responses to SSTs (Figure 12(a); $R = -0.44$, 0.09 and −0.29 with M3, M4 and M6, respectively; $p > 0.05$ in all cases), indicating no meaningful relationships at zero-lag.

Anthropogenic emissions also influence Hg^0_{air} concentrations at Mace Head (Ebinghaus et al., 2002, 2011; Custódio et al., 2022; Feinberg et al., 2024; Molepo et al., accepted), potentially obscuring the link between observed concentrations and SST-enhanced evasion. To assess the potential influence of anthropogenic pollution on our findings, we repeated all analyses (including those in Section 4.3.3.2 below) with the clean sector Hg^0_{air} dataset (see Sect 4.2.4.1 for the filtering procedure). The results, presented in Figure B1.2–Figure B1.4, Appendix B, show minimal differences compared to the unfiltered data, suggesting that anthropogenic emissions have a negligible impact on the Hg^0_{air}–SST relationships (as well as the results in Section 4.3.3.2 below) observed in our study.

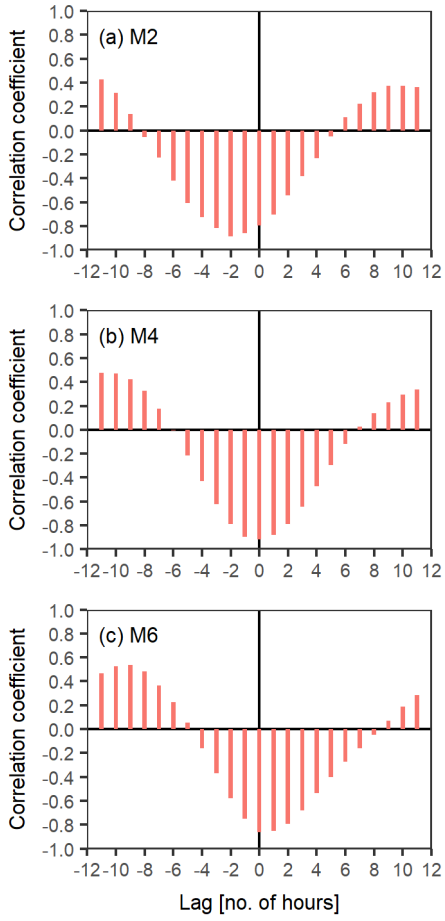

Figure 13: Pearson cross-correlations between diurnal mean Hg^0_{air} concentrations at Mace Head (predicted variable) and SSTs (predictor variable) measured at buoys (a) M2, (b) M4 and (c) M6.

4.3.2.2 Hg^0_{air} and surface ocean primary productivity

Presented in Figure 11(b) and Figure 12(b) are the mean seasonal and annual Hg^0_{air} concentrations along with surface ocean chlorophyll-*a* concentrations from the North Atlantic Ocean, respectively. Seasonally, Hg^0_{air} levels exhibit a moderate inverse relationship with chlorophyll-*a*, although the correlation is not statistically significant (Figure 11(b); $R = -0.56$, $p > 0.05$). Cross-correlation analysis (Figure B2.1(a), Appendix A) reveals a stronger and

statistically significant inverse relationship with a delay of one month ($R = -0.71$, $p < 0.05$). These results suggest that, at the seasonal scale, processes that may enhance net Hg^0 evasion, such as phytoplankton-mediated reduction of Hg^{II} to Hg^0, are outweighed by processes that may reduce net Hg^0 evasion, such as phytoplankton Hg^0_{air} sequestration and/or surfactant-driven evasion suppression, and that the latter two processes significantly contribute to seasonal Hg^0_{air} variability at Mace Head.

However, this apparent oceanic influence should be interpreted with terrestrial vegetation Hg^0_{air} uptake in mind, since (i) both oceanic and terrestrial primary productivity exhibit similar seasonal patterns (Figure 11) and (ii) the control of terrestrial vegetation on northern hemispheric seasonal Hg^0_{air} variability is well established (e.g., Jiskra et al., 2018; Feinberg et al., 2022). At zero lag, the seasonal Hg^0_{air} concentrations show a stronger, statistically significant anticorrelation with NDVI ($R = -0.72$, $p < 0.05$), which is stronger than the corresponding Hg^0_{air}-chlorophyll-*a* relationship. While at the one-month lag seasonal Hg^0_{air} shows a significantly strong anticorrelation with chlorophyll-*a*, a similarly strong anticorrelation is observed with NDVI with the same lag (Figure B2.1(b); $R = -0.73$, $p < 0.05$). This suggests that aquatic primary productivity may also contribute to seasonal modulation of Hg^0_{air} at the site, possibly with a delayed effect, alongside terrestrial vegetation uptake. However, it is difficult to attribute the seasonal aquatic primary productivity contribution in the presence of terrestrial vegetation activity.

At the interannual scale, the influence of oceanic primary productivity becomes clearer. As previously mentioned, increased net terrestrial vegetation activity has been proposed as one of the factors driving the observed long-term downward trend in northern hemispheric Hg^0_{air} concentrations (Jiskra et al., 2018). Consistent with this, we observe a significantly strong inverse relationship between mean annual Hg^0_{air} concentrations and NDVI (Figure 12(c); $R = -0.62$, $p < 0.05$), whereas the correlation with chlorophyll-*a* is weak and insignificant (Figure 12(b); $R = -0.31$ $p > 0.05$). However, despite the arithmetically weak correlation of Hg^0_{air} and chlorophyll-*a*, Figure 12(b) shows an inverse relationship between Hg^0_{air} and chlorophyll-*a*, which is slightly masked by the downward Hg^0_{air} trend. Indeed, detrending the Hg^0_{air} data completely decouples the Hg^0_{air} relationship with NDVI ($R = 0.19$, $p > 0.05$) while strengthening that with chlorophyll-*a* ($R = -0.68$, $p < 0.05$), as observed in Figure 14. Even after detrending NDVI, the relationship between detrended mean annual Hg^0_{air} and NDVI is

weak and insignificant (R = 0.32, p = 0.305; not shown). These results suggest that, while terrestrial vegetation uptake contributes to the long-term Hg^0_{air} downward trend, interannual variability is related to surface ocean primary productivity.

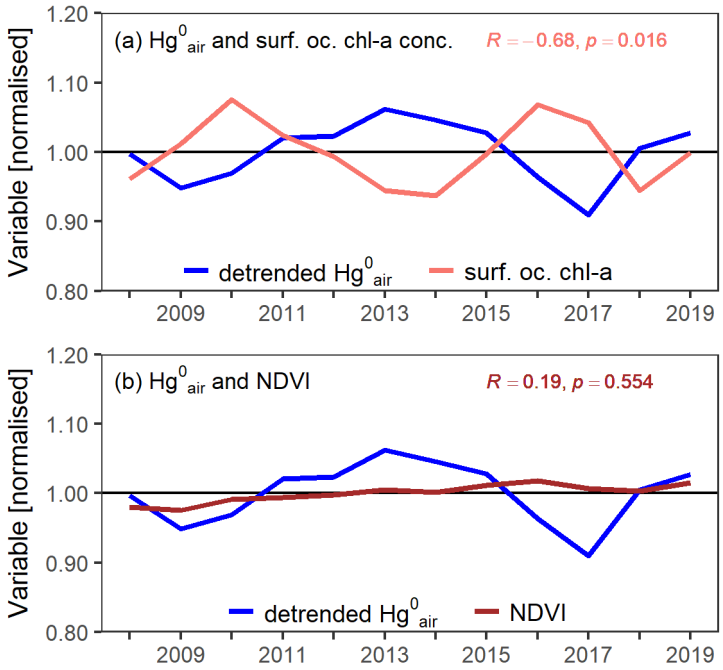

Figure 14: Similar to Figure 12(b) and Figure 12(c), but with the Hg^0_{air} data detrended to remove the long-term trend.

To further investigate, we extended the Hg^0_{air}–chlorophyll-*a* analysis to the southern hemisphere. At Cape Point, on the southwestern tip of South Africa, the surrounding South Atlantic and Southern oceans are a known net source of Hg^0_{air} (e.g., Bieser et al., 2020; Slemr et al., 2020; Molepo et al., accepted). Combining Cape Point Hg^0_{air} measurements with surface ocean chlorophyll-*a* concentrations from these oceans (see Section B4, Appendix B for details on the southern hemispheric datasets), we examined relationships between the two variables at seasonal and annual scales. Seasonally, no correlation was found between Hg^0_{air} and chlorophyll-*a* concentrations (Figure B1.5), despite having similar productivity (mean 0.40 ± 0.14 std. dev.: 0.43 ± 0.14 mg m^{-3} for 2008–2019 for the North Atlantic; 0.40 ± 0.14 mg m^{-3} between 2008–2017 for the South Atlantic and Southern Ocean). At the interannual scale

(Figure 15(a)), however, as with Mace Head, Hg^0_{air} concentrations show an inverse relationship with chlorophyll-*a*. Although the correlation is moderate and not statistically significant ($R = -0.45$, $p > 0.05$), which may be due to the small data set, this inverse relationship supports the strong link between surface ocean primary productivity and Hg^0_{air} concentrations on interannual scales. However, the lack of a seasonal Hg^0_{air}–chlorophyll-*a* relationship at Cape Point, where the influence of terrestrial vegetation uptake is much less dominant (Jiskra et al., 2018), raises questions whether the Hg^0_{air}-chlorophyll-*a* relationship at Mace Head is merely an artefact of the terrestrial vegetation-driven Hg^0_{air} seasonality at the northern hemispheric site.

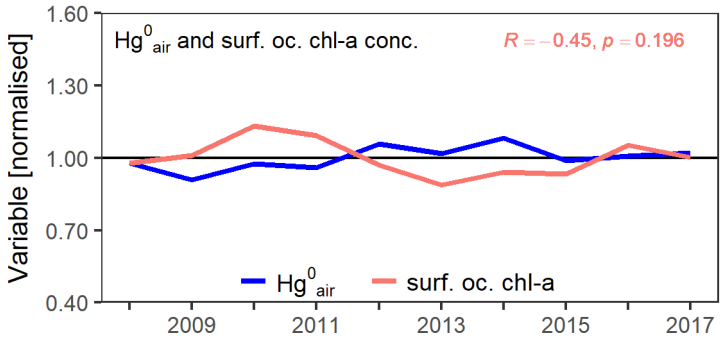

Figure 15: Normalised mean annual variation in Hg^0_{air} concentration at Cape Point and surface ocean chlorophyll-*a* concentration over the South Atlantic and Southern oceans between 2008 and 2017. The horizontal line represents the normalised mean value (i.e., 1 ng m^{-3} for Hg^0_{air} concentration and 1 mg m^{-3} for chlorophyll-*a* concentration); actual (non-normalised) mean values are shown in the table in Figure B3.1. The pearson correlation coefficients (*R*) and associated *p*-values (*p*) between the two time series is shown on the top right.

4.3.3 Drivers of interannual chlorophyll-*a* variability

As discussed in the previous section, both hemispheres show an inverse relationship between interannual Hg^0_{air} concentrations and surface ocean primary productivity. This raises the question of the underlying drivers of interannual variability in primary productivity. A plausible factor is biomass burning, which can deposit anomalously high levels of nutrients (such as iron) to the surface ocean, stimulating phytoplankton growth (e.g., Wang et al., 2022; Weiss et al., 2022; Liu and Wang, 2025). However, biomass burning would also increase Hg^0_{air} concentrations, leading to a positive correlation between Hg^0_{air} and surface ocean chlorophyll-

a concentrations, opposite to our observations. Furthermore, Slemr et al. (2020), who also analysed the mean interannual Hg^0_{air} variability at Cape Point, concluded based on concurrent patterns in other gases (e.g., CO and radon), that the variability is likely linked to oceanic rather than terrestrial processes.

4.4 Summary and conclusions

This study aimed to improve understanding of Hg^0 air–sea exchange by investigating the potential influence of SST and surface ocean primary productivity on this process. We analysed 12 years (2008–2019) of Hg^0_{air} measurements from Mace Head, Ireland, alongside SST observations from offshore buoys and satellite-derived surface chlorophyll-*a* concentrations in the North Atlantic Ocean, the latter representing surface ocean primary productivity. Assuming that Hg^0_{air} concentrations at Mace Head are directly influenced by Hg^0 air–sea exchange, we investigated their relationship with SST and chlorophyll-*a*. To account for the known influence of terrestrial vegetation on Hg^0 cycling in the northern hemisphere, we also analysed NDVI data. Relationships between Hg^0_{air} and these variables were examined across diurnal, seasonal and interannual scales.

At the diurnal and seasonal scales, Hg^0_{air} concentrations were inversely related to SSTs, contrary to expectations of enhanced Hg^0 emissions with warmer waters due to increased microbial production, decreased solubility and increased diffusivity of Hg^0 in seawater. This suggests that, in the North Atlantic, SST-driven increases in Hg^0 emissions may be minor and/or masked by concurrent opposing processes, such as terrestrial vegetation uptake, phytoplankton uptake or increased boundary layer height, which also generally respond positively to solar radiation. Future studies should quantitatively assess SST-driven evasion by isolating it from the effects of these competing processes. At the interannual scale we observed no significant Hg^0_{air} correlations with SSTs.

Regarding surface ocean primary productivity, we found strong negative correlations between Hg^0_{air} and chlorophyll-*a* concentrations at the seasonal and annual scales. This suggests that processes such as Hg^0_{air} sequestration by phytoplankton or surfactant-driven suppression of Hg^0 evasion outweigh phytoplankton-mediated Hg^{II} (to Hg^0) reduction and substantially contribute to the Hg^0_{air} variability at Mace Head. However, seasonal Hg^0_{air} also showed a strong negative relationship with NDVI, making it difficult to ascertain seasonal oceanic primary

productivity influence from terrestrial vegetation uptake. Moreover, at Cape Point in the southern hemisphere, where terrestrial vegetation uptake is negligible, no seasonal Hg^0_{air}–chlorophyll-*a* correlation was found, bringing into question whether the seasonal Hg^0_{air}-chlorophyll-*a* relationship observed at Mace Head is an artefact of the terrestrial vegetation-driven Hg^0_{air} seasonality. Further studies are needed to confirm whether oceanic productivity plays a meaningful seasonal role at Mace Head.

On the other hand, a similar interannual Hg^0_{air}–chlorophyll-*a* signal was found at Cape Point, confirming the interannual link between Hg^0_{air} and aquatic primary productivity on a global scale. Moreover, at Mace Head, we also found that, while the long-term decrease in Hg^0_{air} levels may be related to terrestrial vegetation activity, interannual variability may be strongly tied to oceanic primary productivity. These findings show that surface ocean primary productivity, a driving mechanism which has largely been overlooked, may play a significant role in modulating Hg^0 air–sea exchange and resultant Hg^0_{air} concentrations in the Marine Boundary Layer (MBL).

Chapter 5 – Overall conclusions and outlook

In this dissertation, elemental mercury (Hg^0) air–sea exchange has been extensively examined using long-term atmospheric Hg^0 (Hg^0_{air}) concentration measurements from four ground-based coastal monitoring sites: Mace Head (Ireland) and Cape Point (South Africa), the longest continuous Hg^0_{air} records in the northern and southern hemisphere, respectively, Cabo Verde Observatory (sub-tropical North Atlantic) as well as Amsterdam Island (remote Indian Ocean). These datasets, combined with air mass back trajectory analyses and ancillary environmental data, provided new insights into Hg^0 air–sea exchange processes not previously accessible with short-term in situ measurements from shipboard sampling campaigns.

The work addressed three key objectives:

1) Assessing the influence of Hg^0 air–sea exchange on observed Hg^0_{air} concentrations.
2) Constraining the net global Hg^0 air–sea exchange flux.
3) Understanding the influence of different environmental drivers on Hg^0 air–sea exchange.

The first study (Chapter 3) showed that Hg^0_{air} concentrations at all the monitoring sites gradually increase with air mass recent residence time in the Marine Boundary Layer (MBL), consistent with the thin film gas exchange model. This relationship enabled estimation of a net global ocean Hg^0 evasion flux; the first time the flux is estimated from Hg^0_{air} concentration change with airmass MBL exposure time. The derived flux, ~ 2270 t y^{-1} (95 % confidence interval: 1600–2900 t y^{-1}), is lower than current chemical transport model (CTM) estimates, which range between 2800 and 4000 t y^{-1} (e.g., Horowitz et al., 2017; AMAP/UNEP, 2018; Outridge et al., 2018; Shah et al., 2021; Zhang et al., 2023). While the estimate from the present work is not without uncertainty, it suggests that CTMs overestimate the net flux. Interestingly, a recent study, Tang et al. (2025), which also used long-term ground-based measurements of Hg^0_{air} concentrations, along with isotopic compositions, similarly derived a global evasion flux lower than CTM estimates, concluding that gross oceanic Hg^0 emissions should be below 2250 t y^{-1} ± 891 t y^{-1} (± 1 stand. dev.). A major source of uncertainty in CTM-based estimates is the air–sea gas transfer velocity, which, for Hg^0 there is currently a critical lack of in situ measurements. Current CTM estimates are based on gas transfer velocities derived for other

trace gases, such as CO_2, together with surface wind speed (e.g., Wanninkhof, 1992; McGillis et al., 2001; Nightingale et al., 2000). This approach is problematic as gases with different solubilities do not respond uniformly to the physical processes driving air–sea exchange, meaning that wind speed-based parameterisations developed for one gas may not be directly applicable for others (Osterwalder et al., 2021). In this dissertation, these gas transfer velocity parameterisations could be circumvented, with fluxes estimated using observed concentration changes with air mass recent residence time in the MBL. This work underscores the applicability of indirect observations in constraining Hg^0 air–sea exchange, considering the limited availability of in situ flux measurements.

Despite evidence that oceanic emissions significantly influence observed Hg^0_{air} concentrations, all sites showed weak mean seasonal and especially diurnal Hg^0_{air} variability, a puzzling feature also reported at other locations in the MBL (e.g., Soerensen et al., 2010a, 2013; Wang et al., 2017; Wang et al., 2019). This observation contrasts with expectations of strong variability in oceanic emissions in response to strongly varying environmental parameters such as sea surface temperature (SST), solar radiation and wind speed, which have been suggested to substantially influence Hg^0 air–sea exchange. The weak variability may point to the following: (i) that ocean Hg^0 emissions themselves exhibit limited mean seasonal and diurnal variability, and/or (ii) that other processes are masking the variability. One potential major contributor to (i) could be dark reduction and its role in sustaining surface ocean dissolved Hg^0 (Hg^0_{aq}) concentrations. As proposed by Lamborg et al. (2021), dark reduction, rather than photoreduction, as had been previously believed, may be the dominant source of Hg^0_{aq} in the surface ocean. Being largely independent of climatic conditions, dark reduction may be maintaining relatively stable (that is, exhibiting weak seasonal and diurnal variability) surface ocean Hg^0_{aq} levels, leading to relatively stable emissions and consequently weak seasonal and diurnal variability in Hg^0 air concentrations in the MBL. Nonetheless, even with steady Hg^0_{aq} concentrations, variability in physical exchange processes, such as wind-driven turbulence and SST-driven enhancement of evasion, could still modulate exchange fluxes. To disentangle the relative contributions of supply-side controls (i.e., Hg^0_{aq} concentrations) and physical exchange mechanisms to the observed weak variability in Hg^0_{air} concentrations in the MBL, extensive, simultaneous measurements of Hg^0_{air} and Hg^0_{aq} together with relevant environmental parameters are needed.

Regarding (ii), the second study (Chapter 4), using Hg^0_{air} concentrations at Mace Head, examined the potential role of SST in modulating Hg^0 air–sea exchange, assuming a direct link between the concentrations and air–sea exchange. Contrary to expectations of enhanced evasion with warmer waters, due to increased microbial reduction of Hg^{II} as well as increased diffusivity and decreased solubility of Hg^0 in seawater, concentrations exhibited strong negative correlations with SSTs at both diurnal and seasonal scales. This finding also contradicts with previous studies reporting positive Hg^0–SST relationships at other locations, such as the north Adratic Sea (Floreani et al., 2019), Mauna Loa in the Pacific Ocean (Carbone et al., 2016) and Cape Point (Bieser et al., 2020). However, the Mauna Loa (Carbone et al., 2016) and Cape Point (Bieser et al., 2020) studies, for instance, did not explicitly, extensively assess SST influences on seasonal and diurnal scales. The most direct comparison is the study by Floreani et al. (2019), who analysed seasonal-diurnal variations in Hg^0 evasion fluxes, and reported significantly higher fluxes in summer compared to autumn and winter, coinciding with increased SST (and incident solar radiation). It should be noted, however, that the measurements from Floreani et al. (2019), based on the flux chamber technique (discussed in Chapter 2.3.1), only reflect micro-environmental conditions. Similarly, laboratory experiments demonstrate a positive SST effect on microbial Hg^{II} reduction (e.g., Lee and Fisher, 2019), but the large-scale impact is unclear. While such studies are crucial for isolating and understanding individual mechanisms, they do not account for interacting variables in natural systems.

As demonstrated in this dissertation, on a large scale, or at least in the open North Atlantic (where the air masses sampled at Mace Head originate), SST increases do not correspond to observable increases in Hg^0_{air} concentrations. Instead, concentrations are negatively correlated with SST, likely reflecting the influence of opposing processes, such as phytoplankton uptake (Santos et al., 2024), foliar uptake (e.g., Jiskra et al., 2018) and increased boundary layer height, which also respond positively to solar radiation. In summary, while SST likely enhances seawater Hg^0 production and evasion under controlled environments, on a large scale (both spatially and temporally) its impact may be outweighed by concurrent processes that suppress Hg^0_{air} concentrations. Findings from this dissertation show the value of long-term, ground-based observations in complementing in situ and laboratory approaches for a more comprehensive understanding of environmental controls on Hg^0 air–sea exchange.

Also examined in Chapter 4 was the potential net influence of surface ocean primary productivity, which may influence air–sea Hg^0 dynamics through various, contrasting mechanisms: mediating aqueous Hg^{II} reduction (Grégoire and Poulain, 2014; Kim et al., 2016; Lee and Fisher 2018; Liang et al., 2022), sequestering Hg^0_{air} (Santos et al., 2024) as well as forming biological surfactants that suppress air–sea gas exchange (Tsa and Liu, 2003; Pereira et al., 2018; Li et al., 2024). Negative correlations were found between Hg^0_{air} concentrations and surface ocean chlorophyll-*a* concentrations in the North Atlantic (used to represent primary productivity) at seasonal and interannual scales, suggesting that phytoplankton uptake and/or surfactant-driven evasion suppression outweigh phytoplankton-mediated Hg^0 production, and that the former mechanisms significantly contribute to Hg^0_{air} variability in the North Atlantic region. However, seasonal mean Hg^0_{air} concentrations also showed a strong negative relationship with NDVI, consistent with the well-established impact of foliar uptake (e.g., Jiskra et al., 2018; Feinberg et al., 2022). At Cape Point, where foliar uptake is minimal, no seasonal Hg^0_{air}–surface ocean primary productivity relationship was found, raising the possibility that the observed Mace Head Hg^0_{air}–surface ocean primary productivity signal is simply an artefact of the foliar-uptake-driven Hg^0_{air} seasonality, since both aquatic and terrestrial primary productivity exhibit the same seasonality.

On the other hand, a similar interannual Hg^0_{air}–chlorophyll-*a* signal was found at Cape Point, confirming the interannual link between Hg^0_{air} concentrations and aquatic primary productivity on a global scale. Moreover, from the Mace Head analysis, the present work also showed that, while the long-term decrease in Hg^0_{air} levels in the northern hemisphere is more likely related to terrestrial vegetation activity, interannual variability may be more strongly tied to oceanic primary productivity.

Together, these findings suggest that, on a global scale, surface ocean primary productivity has a substantial influence on Hg^0 air–sea exchange and resultant concentrations in the MBL. However, at the season scale in the northern hemisphere, concentrations may be more strongly influenced by terrestrial vegetation uptake. Further analysis, performed at more sites in both hemispheres, is needed to evaluate whether oceanic productivity plays a meaningful seasonal role in Hg^0 air cycling in the MBL. In addition, further studies are needed to isolate and quantify the roles of phytoplankton uptake vs surfactant presence.

In conclusion, this dissertation provides new constraints on Hg^0 air–sea exchange and cycling in the MBL. It underlines the roles of atmospheric transport and oceanic variables, and in particular, surface ocean primary productivity, a factor that has been largely overlooked, in shaping Hg^0_{air} concentrations in the MBL. Moreover, the dissertation demonstrates the value and applicability of indirect observations, that is, ground-based Hg^0_{air} measurements, in constraining Hg^0 air–sea exchange and building a more comprehensive understanding of this crucial component of the global Hg cycle. These datasets, which are more comprehensive, can help bridge knowledge gaps stemming from the scarce availability of direct observations. Notwithstanding, this does not diminish the need for direct observations. Moving forward, progress will require coordinated, widespread, frequent and high-resolution in situ measurements of both Hg^0_{air} and Hg^0_{aq}, along with relevant meteorological and oceanographic data. These measurements are essential for deriving Hg^0-specific air–sea transfer velocities, addressing uncertainties arising from the wind-based parameterisations derived from other gases, and for improving understanding of how different environmental drivers modulate Hg^0 air–sea exchange.

Appendix A – Supplementary information for Chapter 3

A1. Supplementary figures

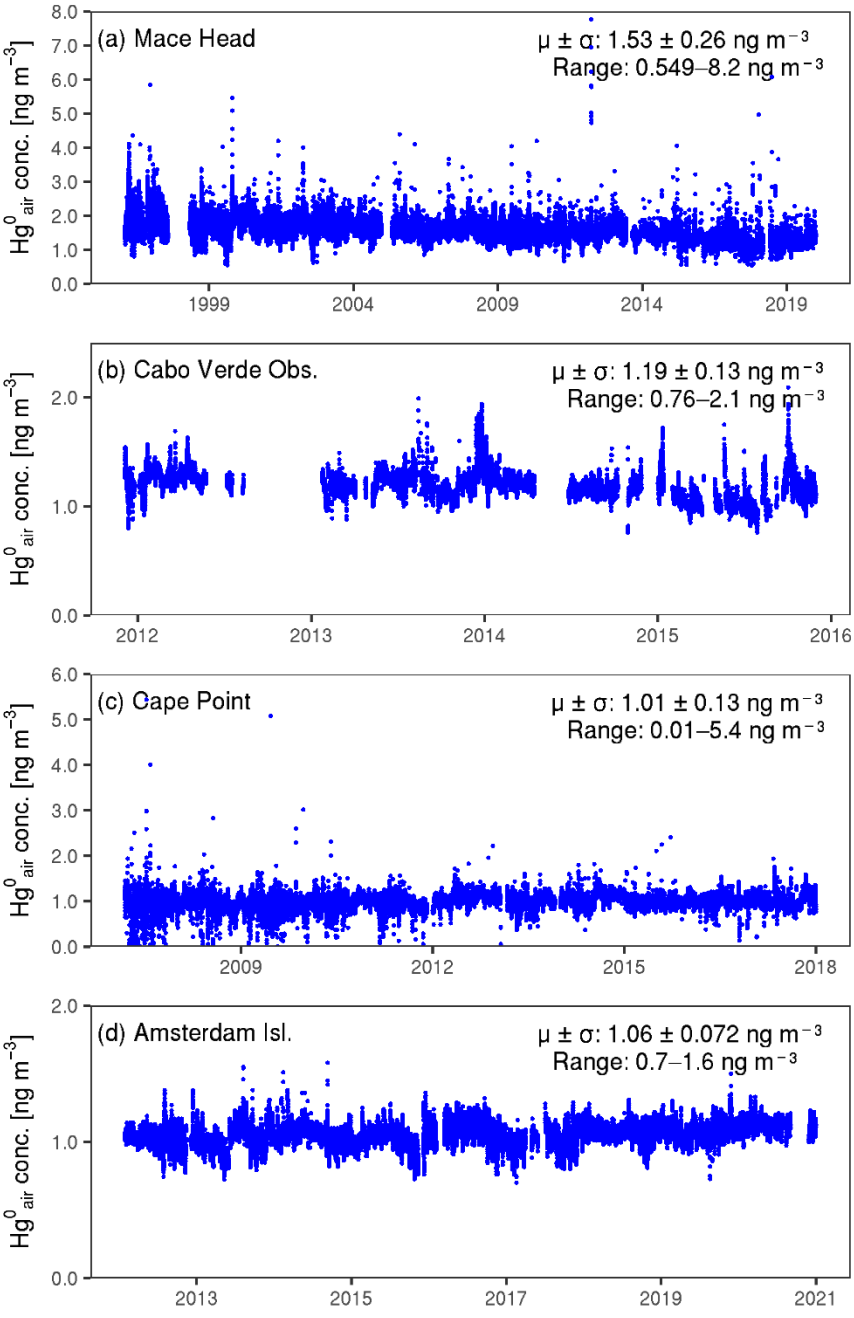
(a) Mace Head
μ ± σ: 1.53 ± 0.26 ng m⁻³
Range: 0.549–8.2 ng m⁻³
(b) Cabo Verde Obs.
μ ± σ: 1.19 ± 0.13 ng m⁻³
Range: 0.76–2.1 ng m⁻³
(c) Cape Point
μ ± σ: 1.01 ± 0.13 ng m⁻³
Range: 0.01–5.4 ng m⁻³
(d) Amsterdam Isl.
μ ± σ: 1.06 ± 0.072 ng m⁻³
Range: 0.7–1.6 ng m⁻³
Hg⁰air conc. [ng m⁻³]

Figure A1.1: Hourly mean Hg^0_{air} concentrations at (a) Mace Head, (b) Cabo Verde Observatory, (c) Cape Point and (d) Amsterdam Island. The mean ± 1 standard deviation as well as the range of the hourly observations are shown in each panel. Note that the extent of both the x- and y-axis differs across the four panels.

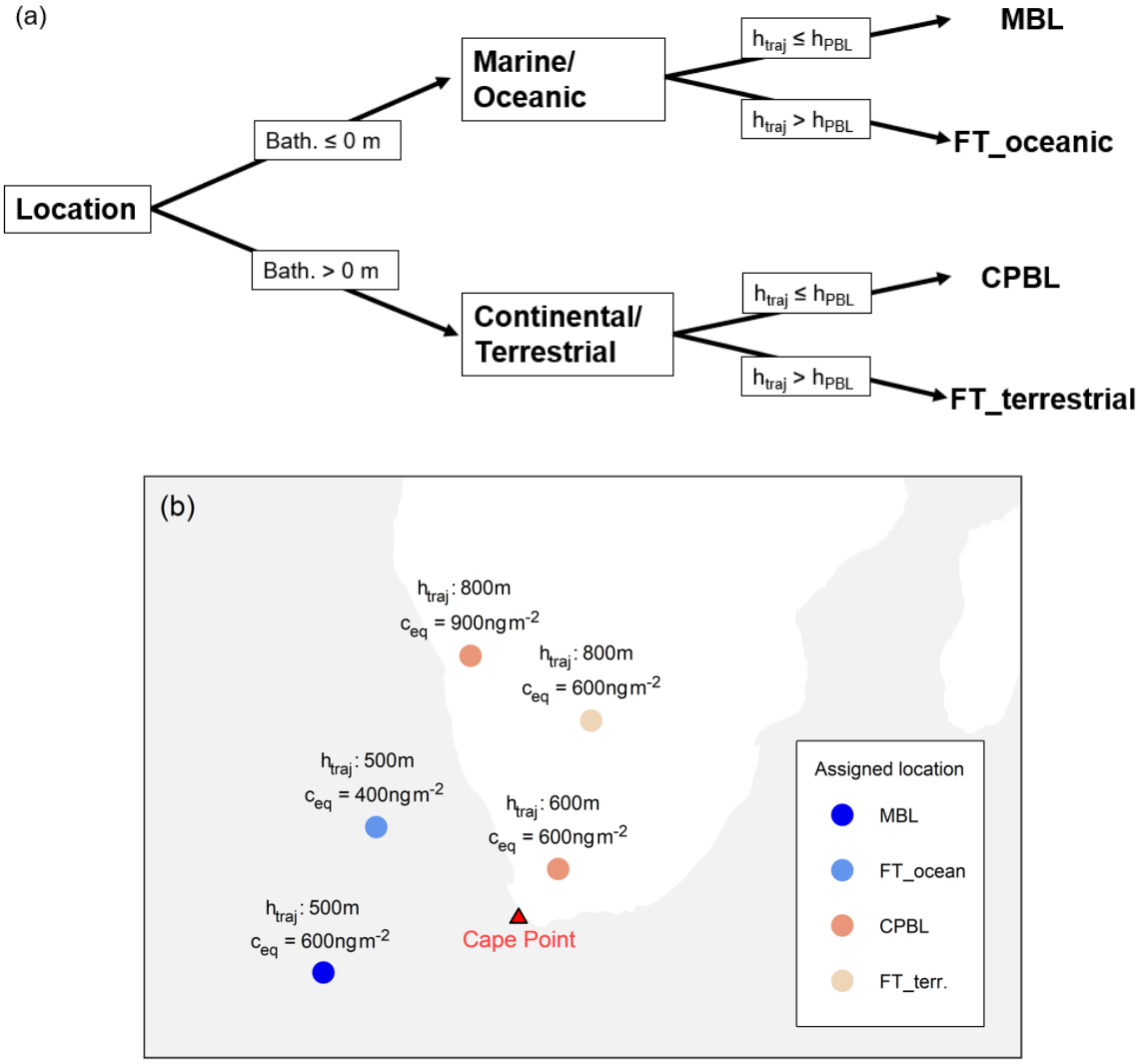

Figure A1.2: Illustration of the trajectory-segment categorisation applied in the study. (a) Framework of the trajectory-segment categorisation applied in the study. Bathymetry denotes the GEBCO-derived bathymetry at the location of the trajectory, "h_{traj}" the height above ground/sea level of the trajectory

segment, and "h_{PBL}" the ERA5-obtained PBL height at the instance (i.e., the time and geographical location) of the trajectory segment. Segments over the ocean at a height equal to or below the PBL height are assigned MBL, while those over the ocean above the PBL are FT_ocean. Similarly, segments over land at or below the height of the PBL are assigned CPBL, while those over land above the PBL are FT_terrestrial. (b) Randomly generated trajectory points to illustrate the categorisation

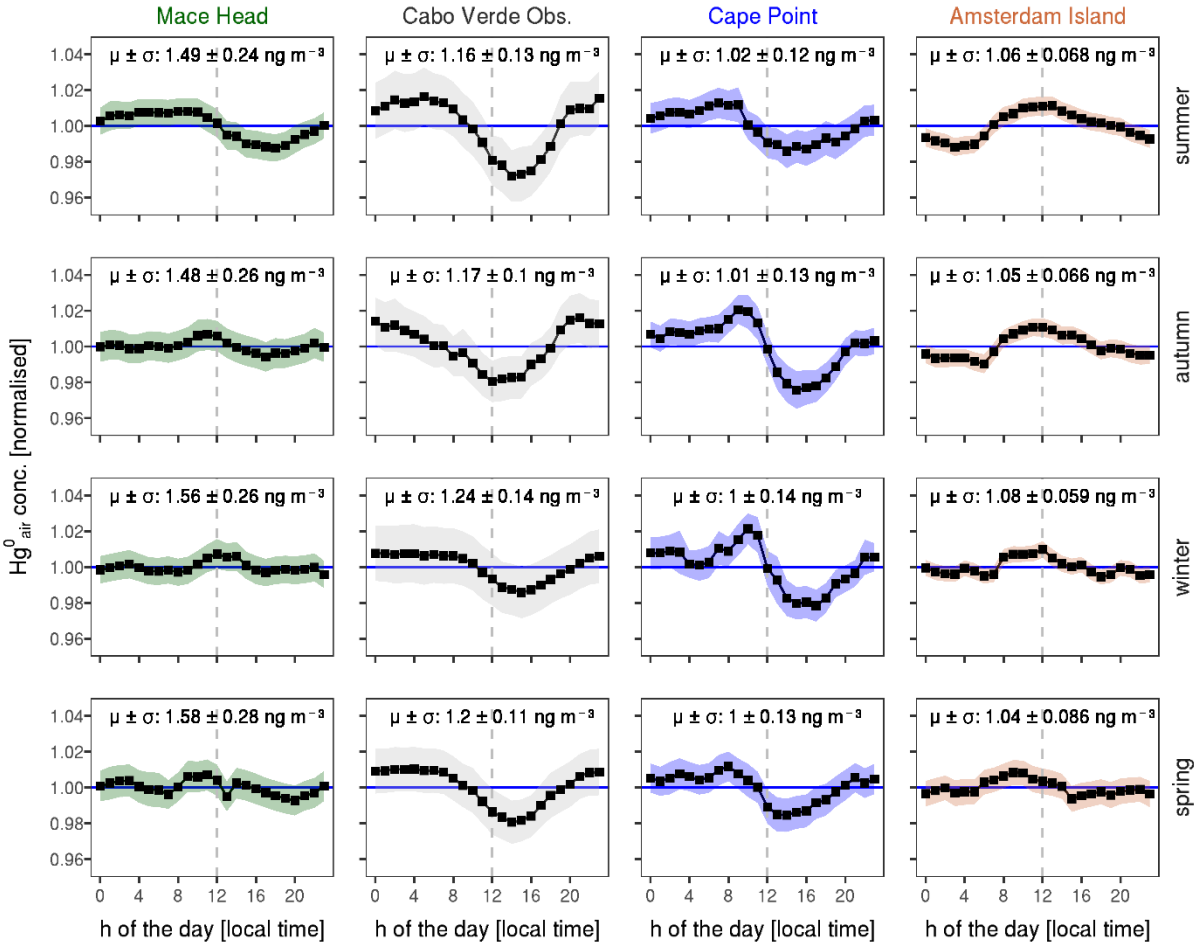

Figure A1.3: Normalised mean atmospheric Hg^0 diurnal variation at the fur study sites in different seasons. Summer, autumn, winter and spring refer to Jun–Aug, Sep–Nov, Dec–Feb and Mar–May, respectively, for Mace Head and Cabo Verde Observatory, and to Dec–Feb, Mar–May, Jun–Aug and Sep–Nov, respectively, for Cape Point and Amsterdam Island. The mean ± the standard deviation of the hourly observations in each season is shown in the panel. The shaded area shows the mean ± 2 times the standard error. The horizontal line represents the normalised mean value (i.e., 1 ng m^{-3}) and the dashed vertical line is plotted along 12:00 local time.

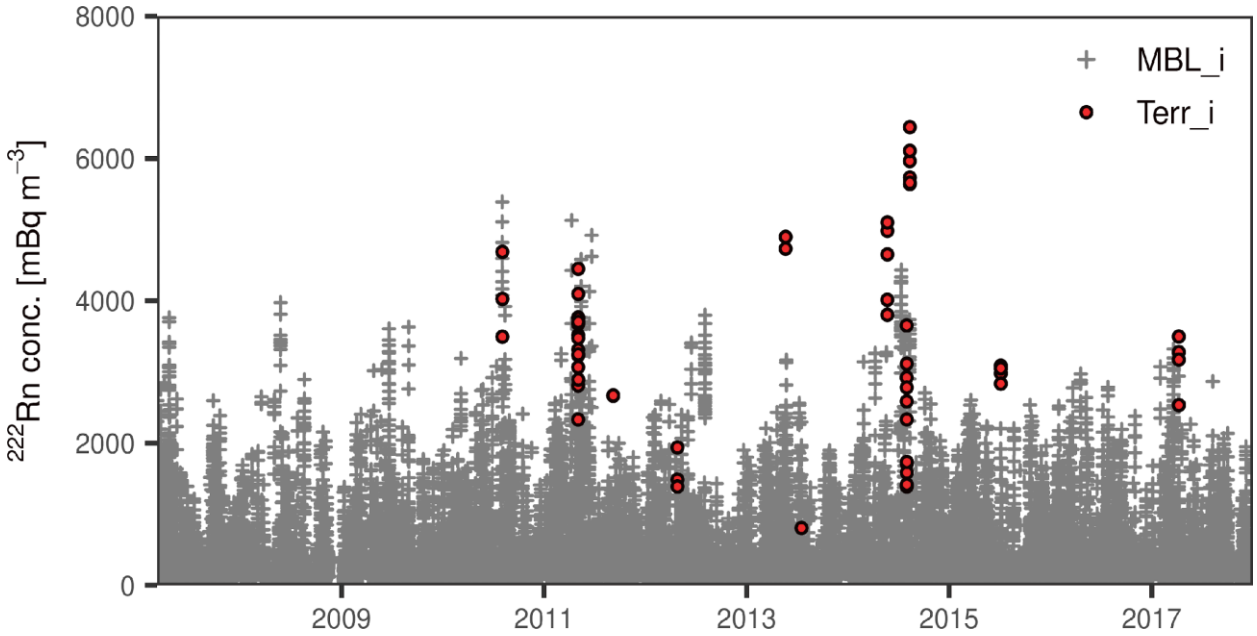

Figure A1.4: Time series of hourly mean ^{222}Rn concentrations at Cape Point, with the data points distinguished between MBL_i and Terr_i.

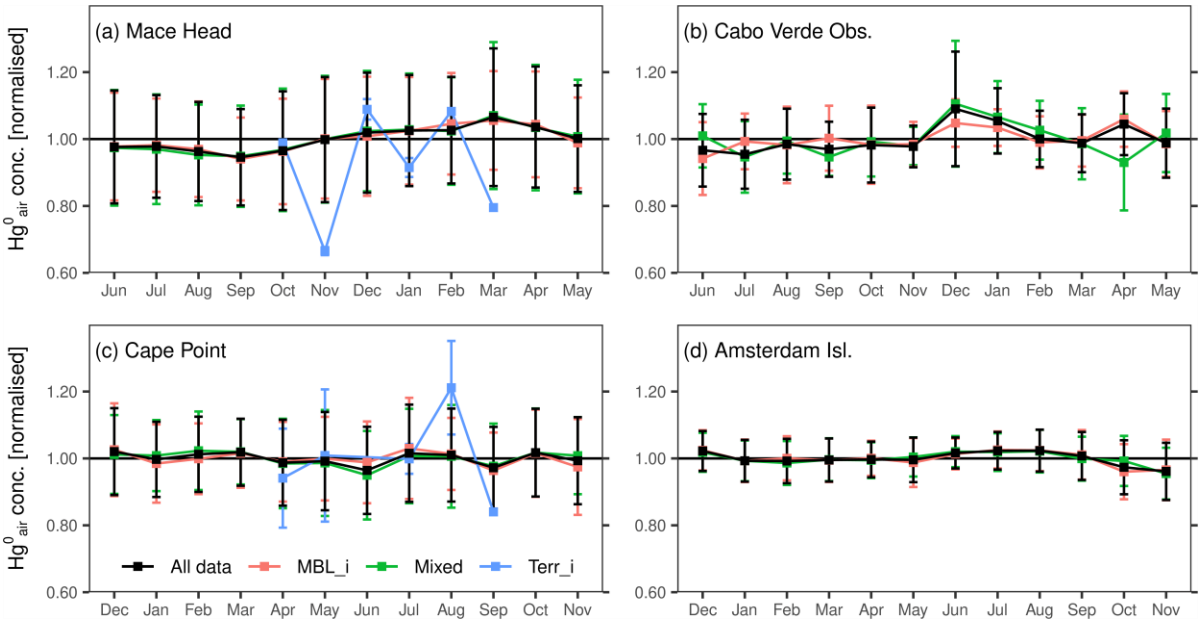

Figure A1.5: Similar to Figure 4 in the main text but also including the MBL_i, Terr_i and Mixed Hg^0_{air} datasets for each site. The mean, standard deviation and proportion of hourly observations assigned to each category is provided in Table S1 in this Supplement.

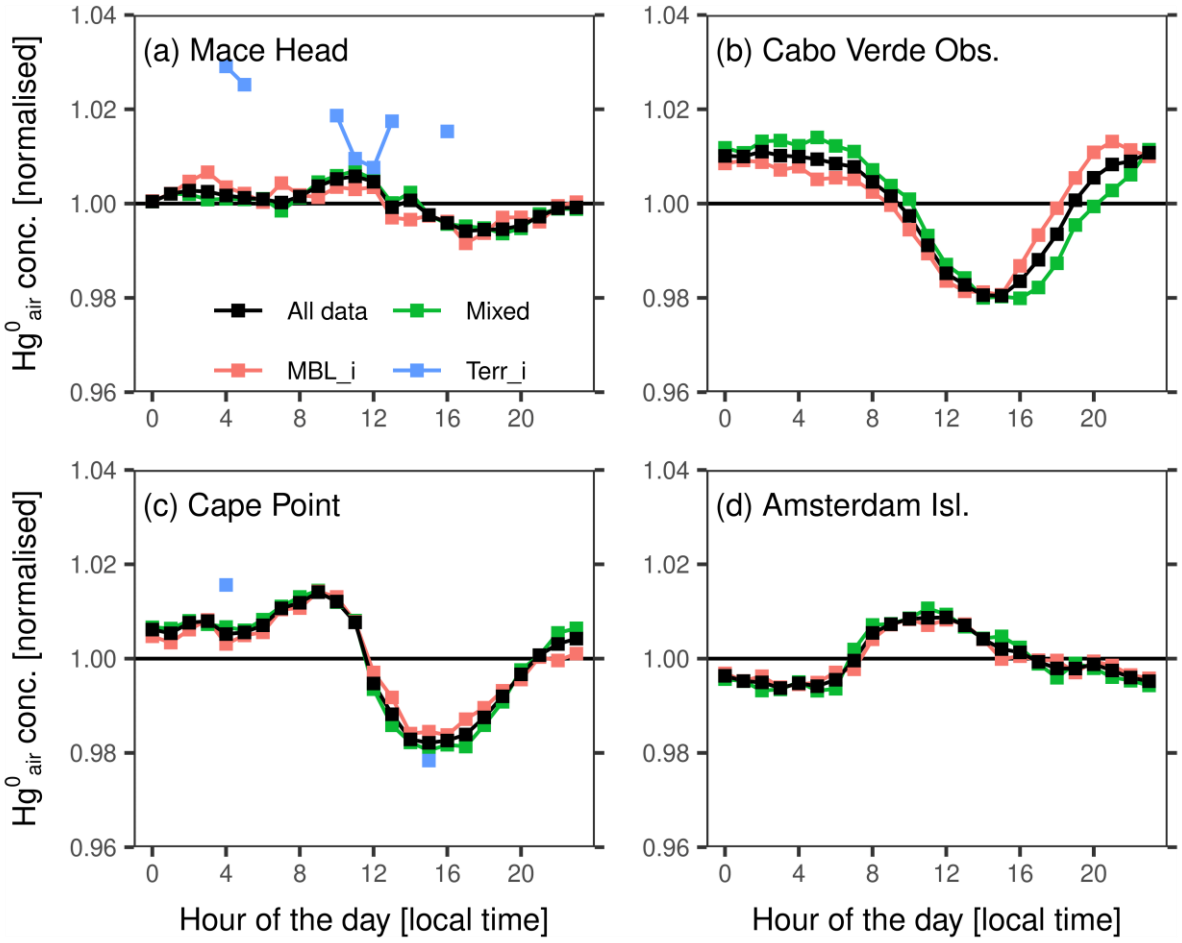

Figure A1.6: Similar to Figure 5 in the main text but also including the MBL_i, Terr_i and Mixed Hg^0 datasets for each site. The mean, standard deviation and proportion of hourly observations assigned each category is provided in Table S1 in this Supplement.

Table A1.1: Hg^0_{air} mean concentration, standard deviation as well as proportion of the data from the full the full data ("All data") classified into the group, for the groups MBL_i, Terr_i and Mixed, at the four study sites.

Group	Mean [ng m^{-3}]	Std. dev. [ng m^{-3}]	Proportion of All data [%]
		Mace Head	
All data	1.53	0.26	
MBL_i	1.53	0.24	28.73
Mixed	1.52	0.27	71.24
Terri_i	1.70	0.35	0.03
		Cabo Verd Obs.	
All data	1.19	0.13	
MBL_i	1.19	0.11	53.39
Mixed	1.21	0.14	46.61
Terri_i	–	–	0
		Cape Point	
All data	1.01	0.13	
MBL_i	1.01	0.12	42.95
Mixed	1.00	0.13	56.96
Terri_i	1.07	0.20	0.09
		Amsterdam Isl.	
All data	1.06	0.07	
MBL_i	1.06	0.07	55.74
Mixed	1.06	0.07	44.26
Terri_i	–	–	0

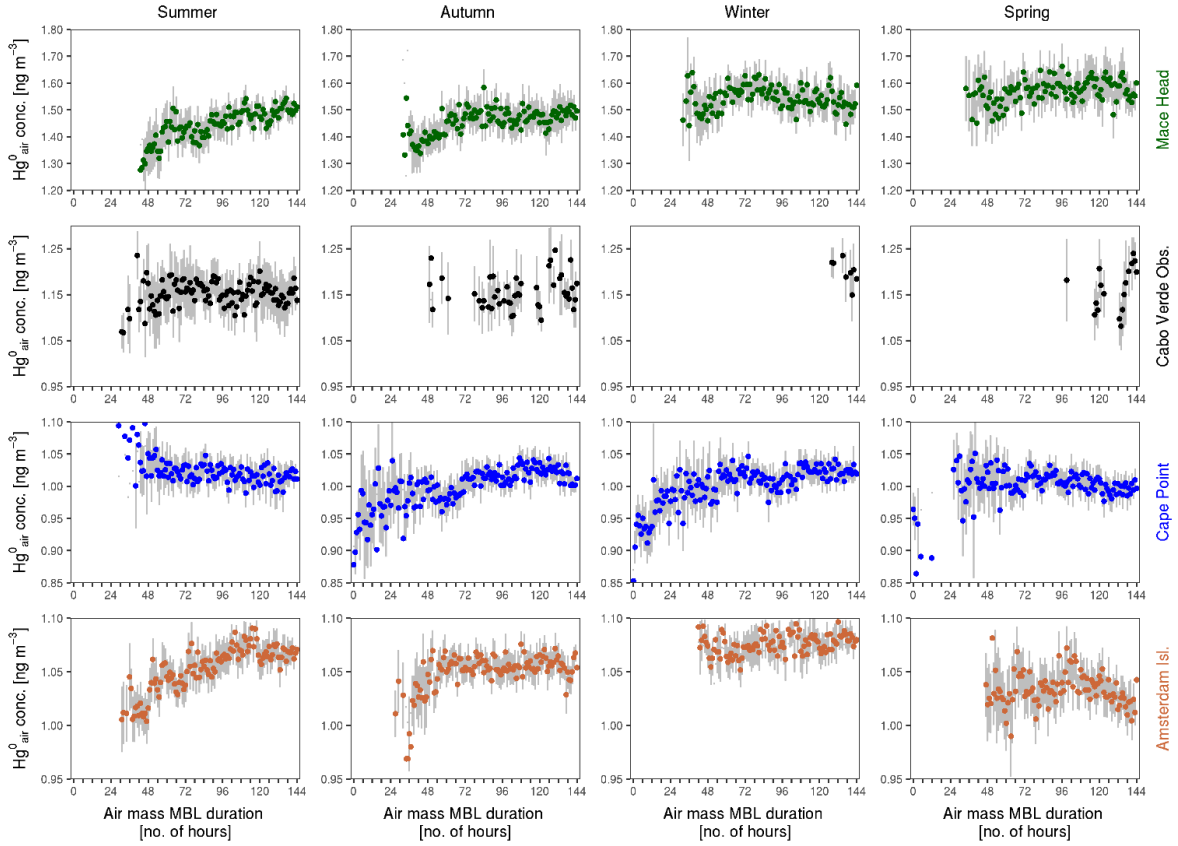

Figure A1.7: Seasonal variation in the relationship between mean Hg^0_{air} concentration and air mass recent MBL residence time at Mace Head, Cabo Verde Observatory, Cape Point and Amsterdam Island. Summer, autumn, winter and spring refer to Jun–Aug, Sep–Nov, Dec–Feb and Mar–May, respectively, for Mace Head and Cabo Verde Observatory, and to Dec–Feb, Mar–May, Jun–Aug and Sep–Nov, respectively, for Cape Point and Amsterdam Island. The bars show 2 times the standard error of the means. The extent of the y-axis differs across the four sites.

A2. Hg^0_{air} concentration in relation to air mass recent MBL residence time

We used the HYSPLIT air mass back trajectories to investigate the relationship between observed Hg^0_{air} concentration and air mass recent MBL residence time. Air mass recent MBL residence time is defined as the number of hours that an air mass (corresponding to an hourly Hg^0_{air} observation) spent in the MBL in the past 144 hours before reaching the site, i.e., the number of segments of the back trajectory that are classified as MBL, as per our back trajectory segment categorisation (described in Section 3.2.2, Chapter 3). We then group together the Hg^0_{air} observations according to recent air mass MBL residence time, at an hourly temporal resolution.

Figure A2.1 shows the mean Hg^0_{air} concentrations against air mass recent MBL residence time at the four sites. The left-hand panels show the initial results. For Cape Point and Amsterdam Island (Figure A2.1(g) and Figure A2.1(i), respectively), there is a clear pattern of increasing mean Hg^0_{air} concentration with recent air mass MBL residence time, albeit with some outliers. At Mace Head, we observe an increase in mean Hg^0_{air} concentration from 0 to about 14 hours in the MBL, followed by a decline until about 48 hours, a slight increase, and then steady concentrations (Figure A2.1(a)). Cabo Verde Observatory shows a similar pattern, with decreasing concentrations until about 60 hours of MBL duration, followed by an increase until about 68 hours and then mostly steady Hg^0_{air} concentrations (Figure A2.1(d)).

We expected the pattern observed at Cape Point and Amsterdam Island to be present at Mace Head and Cabo Verde Observatory as well, so we investigated further. Since anthropogenic Hg emissions are generally higher in the NH compared to the SH, we hypothesised that, at Mace Head and Cabo Verde Observatory, the relationship between mean Hg^0_{air} concentrations and air mass recent residence time in the MBL is obscured by anthropogenic emissions. This would explain the relatively high mean Hg^0_{air} concentrations at low MBL residence times at the two NH sites (Figure A2.1(a) and Figure A2.1(d)). To reduce the impact of anthropogenic emissions, we removed the hourly Hg^0_{air} observations where the air mass recently had contact with the terrestrial surface, i.e., where the corresponding air mass back trajectory has any segments classified as CPBL (see Figure A2.2 for an illustration of the of the trajectory filtering). These results, referred to as No_CPBL, are shown in the middle column of Figure A2.1. We tested various (less strict) versions of this filter, for instance, removing the Hg^0_{air} observations where the back trajectory had a certain percentage of segments in the CPBL only

in the last 6, 12, or 24 hours before arrival at the site (not shown). These various filters produced more or less similar results to the No_CPBL filter.

As seen in Figure A2.1(b) and Figure A2.1(e), reducing the influence of the terrestrial environment at Mace Head and Cabo Verde Observatory, respectively, reveals a similar pattern to that observed at the SH sites, albeit with considerable noise at the lower MBL residence time groups, particularly at Mace Head. Further investigation showed that the noisy values were due to a low number of observations in the groups (in some instances, a single data point). Therefore, we applied a 12-data-points (equivalent to half a day's observations) minimum filter, removing groups with fewer than 12 observations. This rule was applied to all sites, and the results (Minimum data points) are presented on the right-hand panels of Figure A2.1.

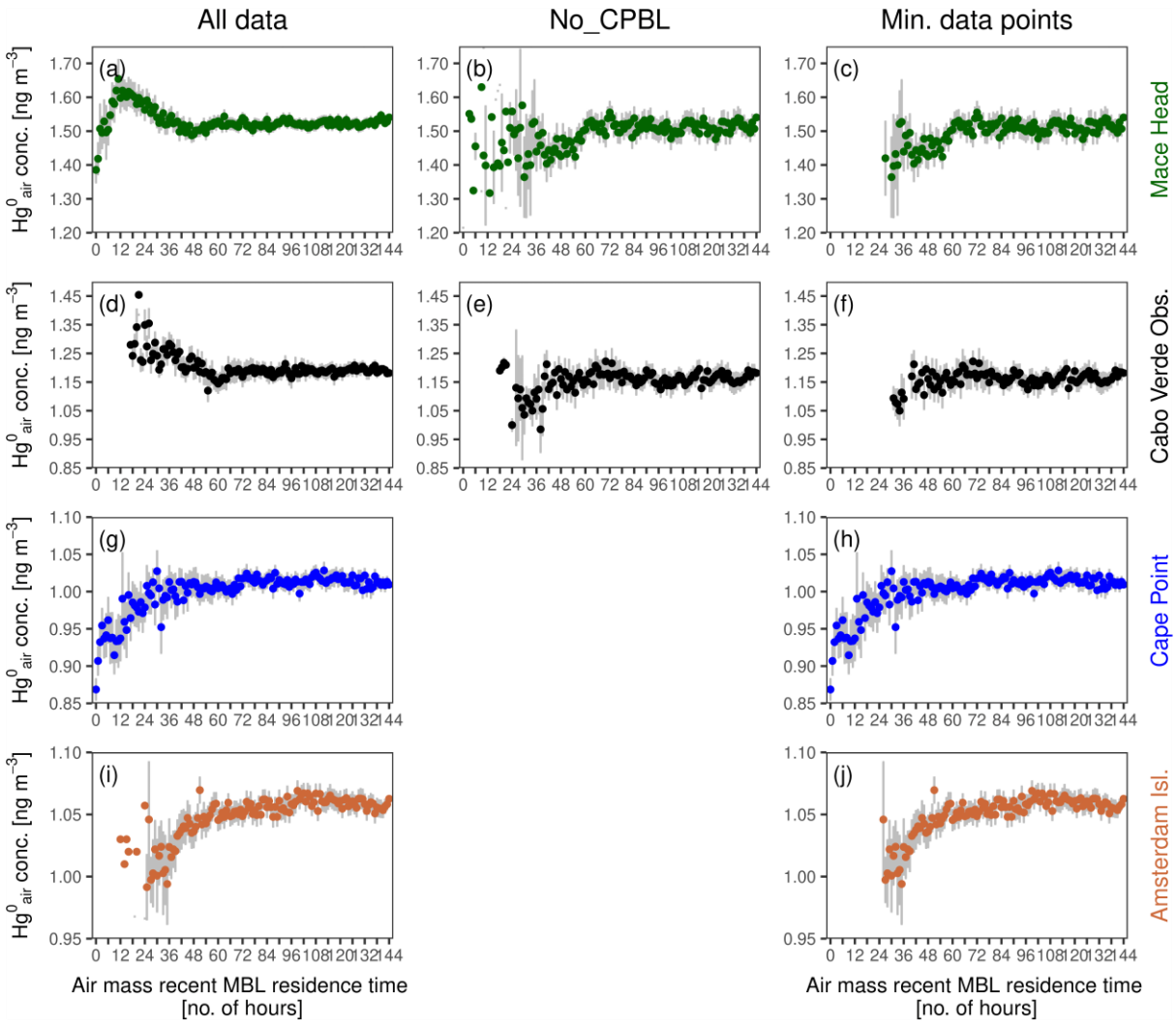

Figure A2.1: Mean Hg^0_{air} concentration against air mass recent MBL residence time at Mace Head, Cabo Verde Observatory, Cape Point and Amsterdam Island, showing the progressive filtering applied. In the panel on the left ("All data"), the entire data set is used at each site. In the middle panels ("No_CPBL"), Hg^0_{air} data points in which the corresponding back trajectory has any segments categorised as CPBL have been removed; this is applied only at Mace Head and Cabo Verde Observatory. In the panels on the right ("Minimum data points"), the same data to the left is used but MBL residence times with less than 12 Hg^0_{air} observations are removed. The bars show 2 times the standard error of the means. Note that the extent of the y-axis differs across the four stations.

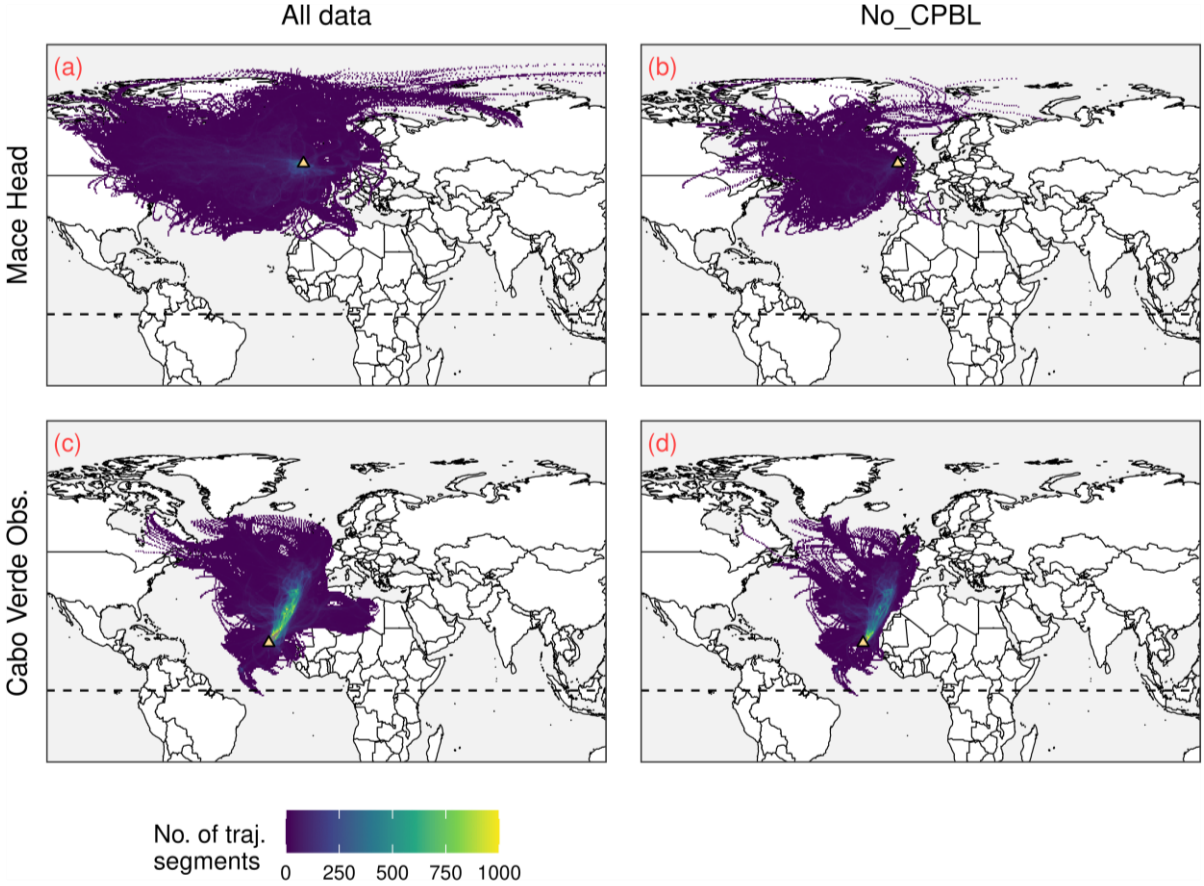

Figure A2.2: Illustration of the back trajectory-based filtering applied at Mace Head and Cabo Verde Observatory, with a sample from Jul–Dec 2013. The left-side panels ((a) and (c)) show the trajectories corresponding to the whole data, and on the right ((b) and (d)) the trajectories which have any segments categorised as CPBL have been removed. The dashed horizontal line shows 0° latitude and the location of the station is illustrated with the yellow triangle.

Influence of Agulhas Current region emissions at Amsterdam Island

The Hg^0_{air} observations at Amsterdam Island show a clear pattern of increasing concentration with air mass recent MBL residence time (Figure A2.1(i)–(j)). Nevertheless, there are occurrences of relatively high mean concentrations at low MBL residence time groups. We investigated these occurrences by studying the individual hourly observations in these groups. The investigation showed that for most of these occurrences, one or more of the hourly

observations has an unusually high value (considering the site's mean of 1.06 ± 0.07 ng m^{-3}), over 1.3 ng m^{-3}. Further investigation into these unusually high concentrations showed a close association with air masses coming from the Agulhas Current region. This finding is analogous to that of Bieser et al. (2020), who observed that elevated Hg^0_{air} concentrations at Cape Point were linked to air masses from the warm Agulhas Current region. We therefore remove all hourly observations at Amsterdam Island where the corresponding trajectory has travelled over the Agulhas Current region (Figure A2.3). For Cape Point, we did not observe the same impact, hence the same filtering was not applied.

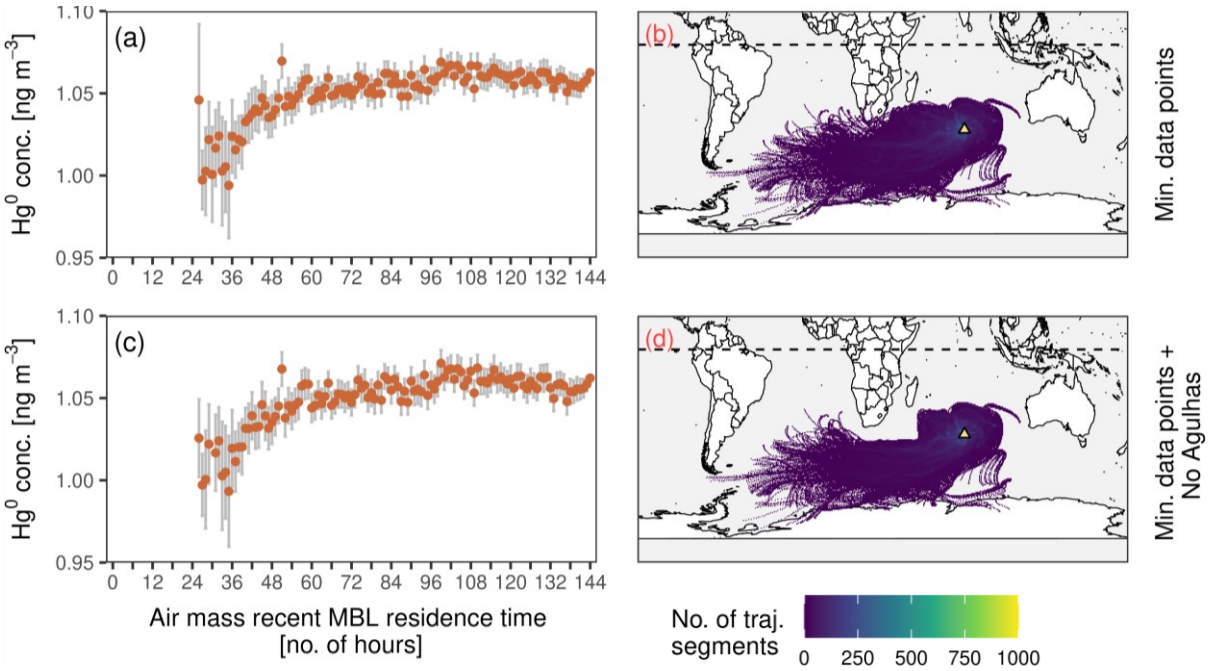

Figure A2.3: Illustration of the Agulhas Current filtering applied at Amsterdam Island. (a)–(c) Mean Hg^0_{air} concentration against air mass recent MBL residence time, and ((b)–(d)) the corresponding air mass back trajectories (a sample, Jan–Jun 2013). (a) Is the same as Figure A2.1(j), while in (c) Hg^0_{air} observations where the back trajectory has travelled over the Agulhas Current (defined as latitude between 40° S and 27° S and longitude between 20° E and 50° E) have been removed (as shown in (d)). In panels (a) and (c) the bars show 2 times the standard error of the means. On the maps the location of the station is shown by the yellow triangle and the dotted horizontal line shows 0° latitude.

A3. Constraining ocean net Hg^0 evasion fluxes from the observed relationship between mean Hg^0_{air} concentration and air mass recent MBL residence time

We use the observed relationship between mean Hg^0_{air} concentration and air mass recent MBL residence time at the sites to constrain the associated mean ocean net Hg^0 evasion fluxes. We apply the continuity equation in the Lagrangian form describing the change in Hg^0 mixing ratio along a trajectory (Brasseur and Jacob, 2017):

$$\frac{d\mu}{dt} = \frac{1}{\rho_a}\left(\frac{F}{h_{PBL}} - L\right), \quad \text{(A1)}$$

where $\mu = c/\rho_a$ is the mass mixing ratio of Hg^0 in air, c is the Hg^0 air concentration and ρ_a the air density, h_{PBL} is the planetary boundary layer height, F is the air–sea Hg^0 exchange flux and L is the net chemical loss of Hg^0. The flux F and net loss L terms are expressed according to:

$$F = k_w\left(c_w - \frac{c}{H'}\right), \quad \text{(A2)}$$

$$L = cR_{ch} \quad \text{(A3)}$$

where k_w is the gas transfer velocity, c_w is the seawater dissolved Hg^0 concentration and $H' = c/c_w$ is the dimensionless Henry's law constant, and R_{ch} is the net chemical loss rate of Hg^0 in the MBL.

Substituting Eqs. (A2) and B(3) into Eq. (A1) and multiplying the resulting equation by air density ρ_{st} = 1.275 kg m^{-3} at standard temperature and pressure (T_{st} = 273.15 K, p_{st} = 10^5 Pa, IUPAC), we obtain the equation for Hg^0 air concentration at standard temperature and pressure (as measured by Tekran):

$$\frac{dc}{dt} = B - Ac, \quad \text{(A4)}$$

where $A = \frac{k_w}{H' h_{PBL}} + cR_{ch}$ and $B = \frac{\rho_{st}}{\rho_a}\frac{k_w c_w}{h_{PBL}}$.

Assuming A and B are constants in the first approximation, Eq. (A4) has a solution:

$$c(t) = \frac{B}{A} - \left(\frac{B}{A} - c_0\right) e^{-At}, \quad \text{(A5)}$$

where c_0 is the initial concentration at $t = 0$.

Equation (A5) can be transformed to

$$c(t) = c_{eq} - De^{-At}, \quad \text{(A6)}$$

where $c_{eq} = B/A$ is the equilibrium concentration ($t \to \infty$), and $D = c_{eq} - c_0$.

Equation (A6) describes the temporal change in the Hg^0 concentration (at standard temperature and pressure) in an air parcel moving along a trajectory.

We obtain c_{eq} by averaging the Hg^0_{air} concentrations at the steady state. Shown in the left-most panels of Figure A3.1 are the c_{eq} values (which are also described in Section 3.3.3 of Chapter 3). Next, taking the natural logarithm of $c_{eq}–c$, we obtain from Eq. (A5):

$$ln(c_{eq} - c) = lnD - At. \quad \text{(A7)}$$

Plotting $ln(c_{eq}–c)$ against air mass MBL residence time and applying a linear approximation, we obtain A and lnD, as well as the standard error (SE) of A (see middle panels of Figure A3.1). Using the A and lnD, we obtain the final approximation of $c(t)$, as shown in the left-most panels of Figure A3.1.

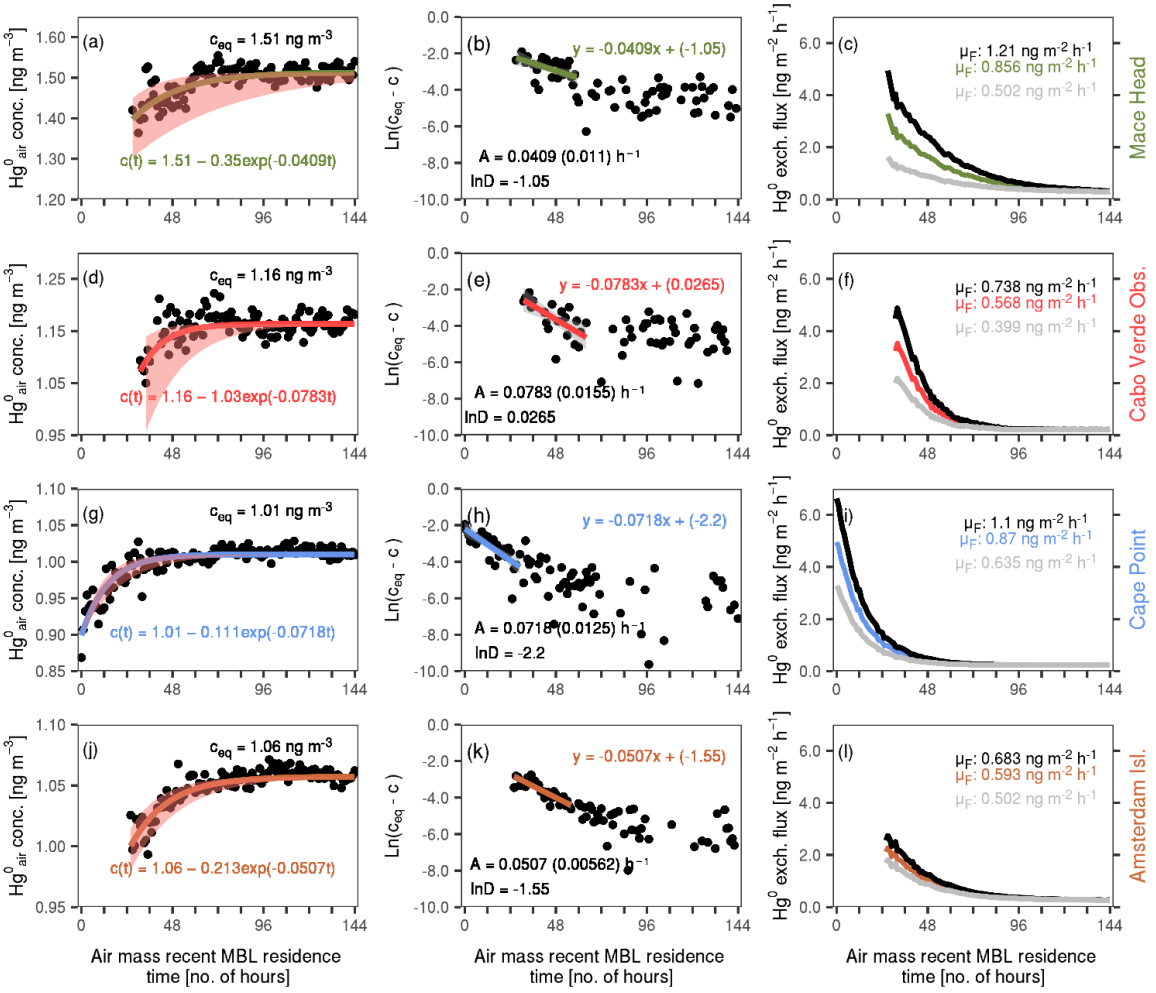

Figure A3.1: Sequential process of estimating mean ocean net Hg^0 evasion fluxes from the relationship between mean Hg^0_{air} concentration and air mass recent MBL residence time at the monitoring sites. Left-most panels: Mean Hg^0_{air} concentration against air mass recent MBL residence time (black dots), with the mean steady state Hg^0_{air} concentration (c_{eq}) and the approximation for *c(t)* (curve and equation) also shown. The shading gives the approximate 95 % confidence interval of *c(t)* (derived using *A* ± 2 times SE of *A*). Middle panels: $ln(c_{eq}–c)$ against air mass recent MBL residence time. Also illustrated is the linear approximation of $ln(c_{eq}–c)$ (curve and the equation) as well as the resultant *A* (including the SE of *A*, in brackets) and *lnD* estimates. Right-most panels: Ocean net Hg^0 evasion flux (*F*) against air mass recent MBL residence time. The three curves correspond to the best approximation and the upper and lower bounds of the 95 % confidence interval of *F* (calculated using *A* ± 2 times SE of *A*). The mean values of the curves, μ_F, are shown on the top right.

Flux estimations using the relationship between mean Hg^0_{air} concentrations and air mass recent MBL duration

Substituting expressions for A and B from Eqs. (A4) into Eq. (A2) and taking into account that $C_{eq} = B / A$, we derive:

$$F = h_{PBL} A \left(\frac{\rho_a}{\rho_{st}} c_{eq} - \frac{A - R_{ch}}{A} c \right). \quad \text{(A8)}$$

Assuming $\rho_a \approx \rho_{st}$ we finally obtain:

$$F \approx h_{PBL} A \left(c_{eq} - \frac{A - R_{ch}}{A} c \right), \quad \text{(A9)}$$

where h_{PBL} is the mean (ERA5-derived) planetary boundary layer height corresponding to the trajectories associated with the Hg^0_{air} observations, considering only the trajectory segments assigned as MBL. The net chemical loss rate R_{ch}, is determined by complex oxidation and reduction reactions of Hg^0 in the MBL and is difficult to evaluate directly. However, its order of magnitude can be roughly estimated using published results from chemical transport modelling. For instance, the average net chemical loss L of Hg^0 in the MBL can be approximately derived from Shah et al. (2021) as 1 ppq d^{-1}, which corresponds to 3.7×10^{-4} ng m^{-3} h^{-1} under standard temperature and pressure conditions. Dividing this by the average Hg^0 concentration of 1.5 ng m^{-3}, we obtain an average net loss rate of $R_{ch} = 2.5 \times 10^{-4}$ h^{-1}. It should be noted that this value is two orders of magnitude lower than the estimated above values of the concentration change rate A (4-8 × 10^{-2} h^{-1}), meaning that net chemical loss does not have significant effect on the variation of Hg^0 in the MBL over short time scales.

In particular, it can be easily shown that under steady-state conditions ($d\mu / dt = 0$) the air–sea exchange flux is close to zero, assuming an insignificant effect of redox chemistry. Indeed, from Eq. (B1) at steady state, we obtain:

$$\frac{F}{h_{PBL}} - L = 0. \quad \text{(A10)}$$

Substituting Eqs. (A2) and (B3) into Eq. (A10), expressing c_w and substituting the expression for A from Eq. (A4), we derive:

$$c_w = \frac{c}{H'}\left(1 + \frac{R_{ch}}{\mathrm{A} - R_{ch}}\right), \tag{A11}$$

which simplifies to $c_w \approx \frac{c}{H'}$ by applying the earlier estimate $R_{ch} \ll A$. Under these conditions, the air–sea flux transforms to

$$F = k_w\left(c_w - \frac{c}{H'}\right) \approx 0. \tag{A12}$$

The final approximation of F is shown in right-most panels of Figure A3.1. We assume that the coloured curves in Figure A3.1 (left column) show the change of Hg^0 concentrations during the recent (last 144 h) transport history of a typical air parcel travelling over the oceanic regions represented by our sites. To obtain the mean fluxes at each site (shown in the top right of the right-most panels), we integrated the instantaneous fluxes over the period from the shortest MBL residence time with a value to the mean MBL residence time. The integral was then normalised by the mean MBL residence time.

Appendix B – Supplementary information for Chapter 4

B1. Supplementary figures

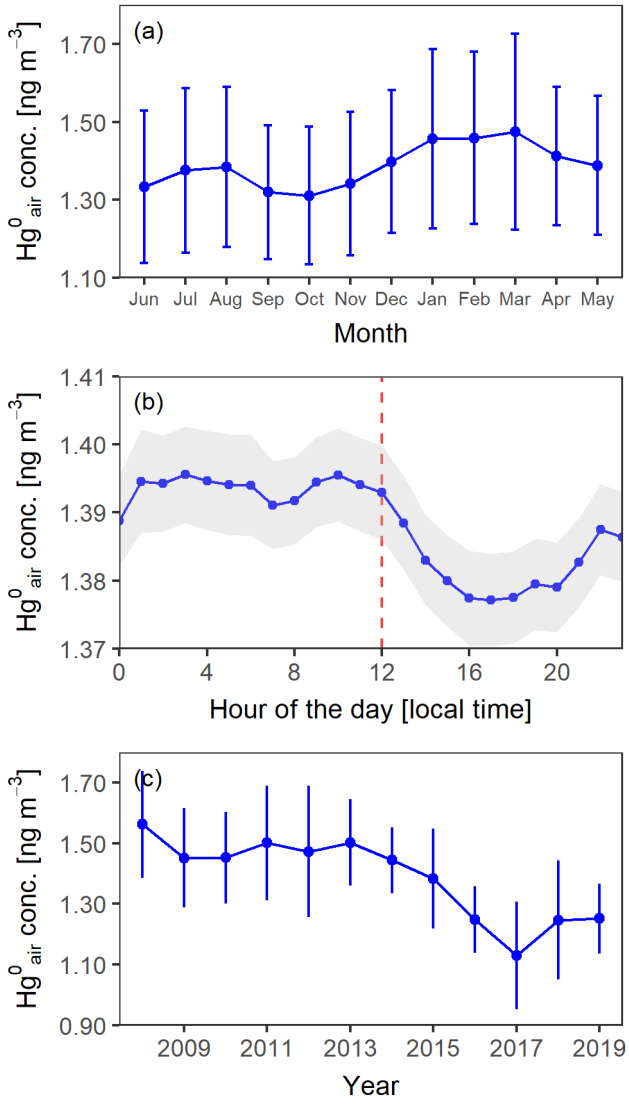

Figure B1.1: (a) Seasonal, (b) diurnal and (c) annual mean Hg^0_{air} concentrations at Mace Head between 2008 and 2019. In panels (a) and (c) the bars show one standard deviation of the monthly and annual means, respectively, while in panel (b) the shaded area shows the mean ± 2 times the standard error. The dotted vertical line in panel (b) shows 12:00 local time.

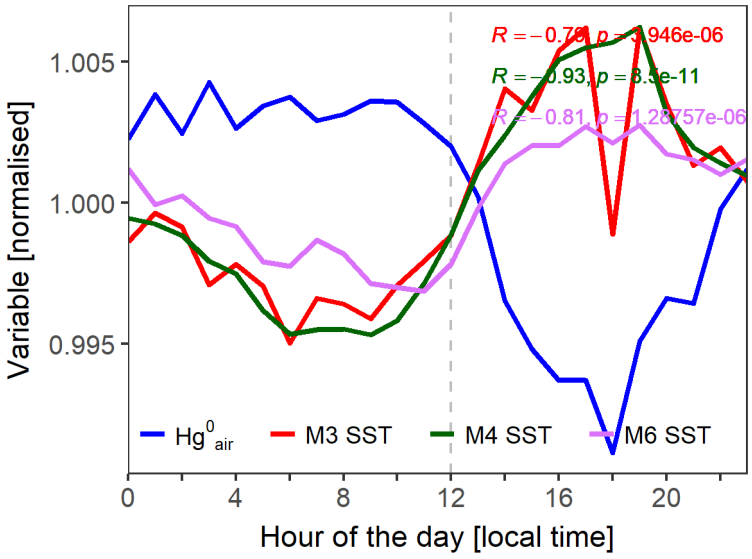

Figure B1.2: Similar to Figure 10 but with the filtered (clean sector) Hg^0_{air} data.

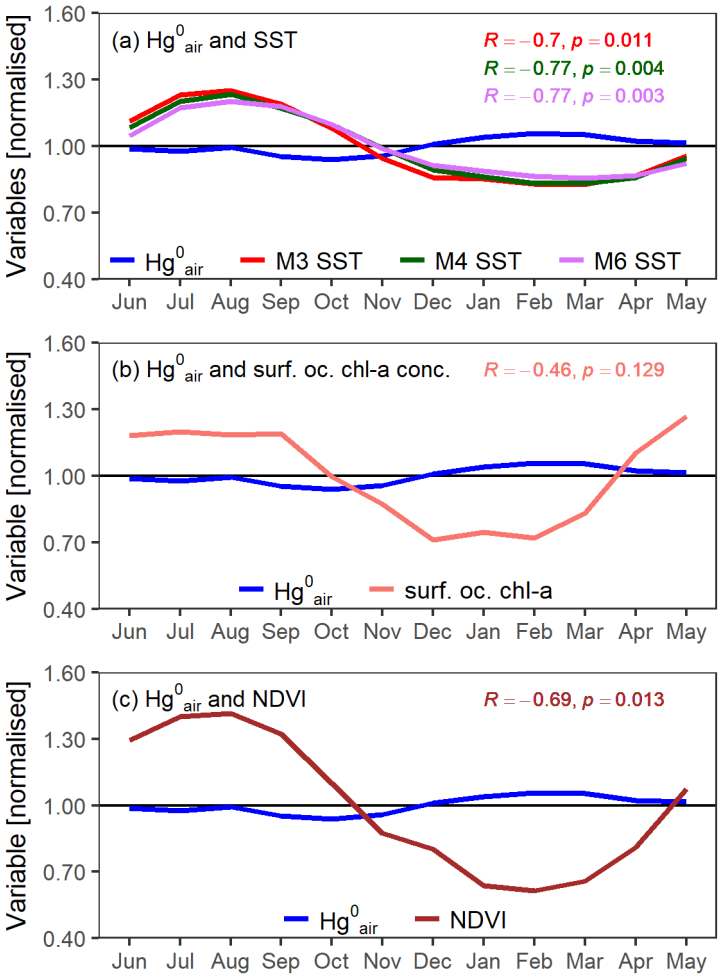

Figure B1.3: Similar to Figure 11 but with the filtered (clean sector) Hg^0_{air} data.

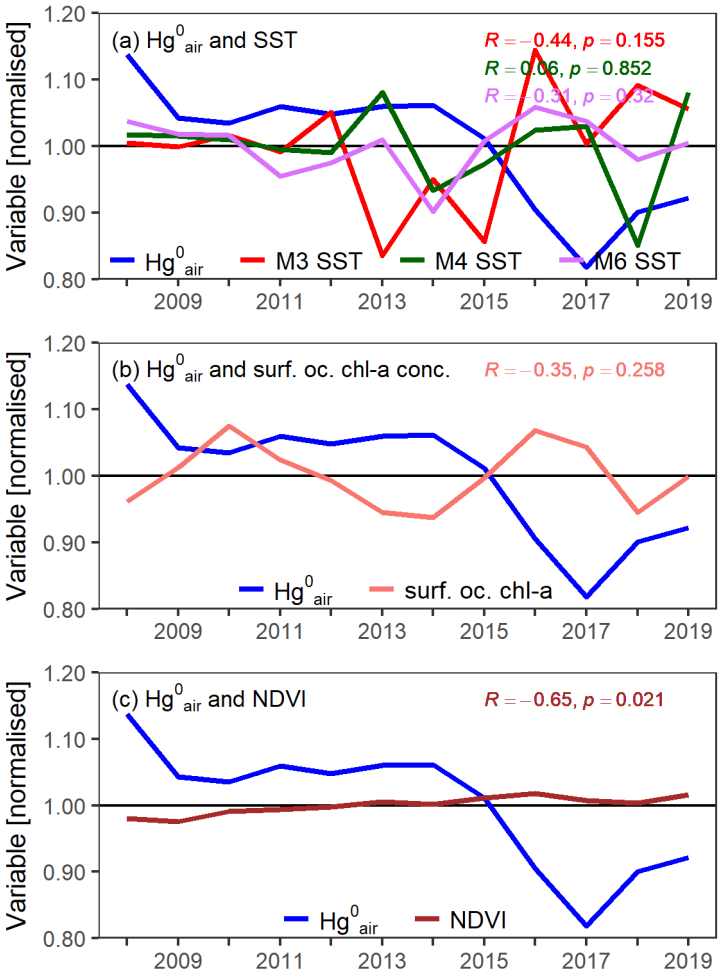

Figure B1.4: Similar to Figure 12 but with the filtered (clean sector) Hg^0_{air} data.

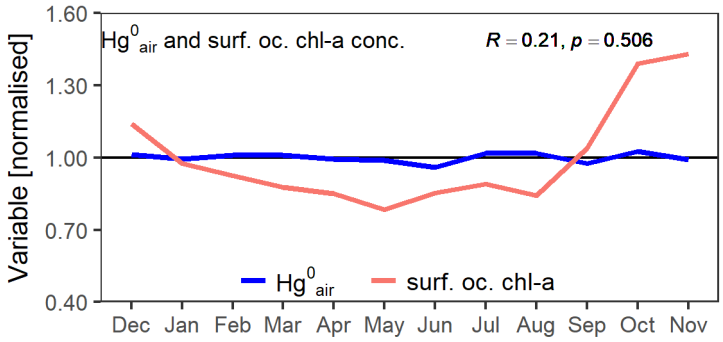

Figure B1.5: Normalised mean seasonal variation in Hg^0_{air} concentration at Cape Point and surface ocean chlorophyll-*a* concentration over the South Atlantic and Southern oceans between 2008 and 2017. The horizontal line represents the normalised mean value (i.e., 1 ng m^{-3} for Hg^0_{air} concentration and 1 mg m^{-3} for chlorophyll-*a* concentration); actual (non-normalised) mean values are shown in the table in Figure B3.1. The pearson correlation coefficients (*R*) and associated *p*-values (*p*) between the two time series is shown on the top right.

B2. Cross-correlation analysis

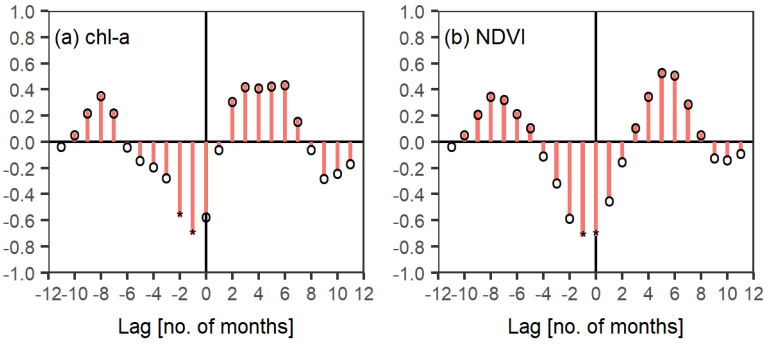

Figure B2.1: Cross-correlations between seasonal mean Hg^0_{air} concentrations at Mace Head (response variable) and (a) surface chlorophyll-*a* over the North Atlantic and (b) NDVI over the northern hemisphere. An asterisk (*) indicates that the correlation is statistically significant ($p < 0.05$) while a circle (o) indicates that it is not ($p \geq 0.05$).

B3. Southern hemisphere data analysis

B3.1 Description of the Cape Point atmospheric monitoring station

The Cape Point atmospheric monitoring station (Figure B3.1(a)) is located at the southern tip of the Cape Peninsula, approximately 60 km south of Cape Town, South Africa (34°21′ S, 18°29′ E; Martin et al., 2017). It is situated within the Cape Point National Park on a coastal cliff about 230 m above sea level (Brunke et al., 2004; Martin et al., 2017). The site experiences a Mediterranean-type climate with moderate temperatures, dry summers and increased precipitation in winter (Brunke et al., 2004). Prevailing winds are from the southeast to southwest, advecting clean marine air from the Southern Ocean (Brunke et al., 2004). However, the site is occasionally affected by anthropogenically polluted air masses from the north to northeast, mainly in winter (Brunke et al., 2010). Cape Point is operated by the South African Weather Service (SAWS) and, as with Mace Head, is part of multiple research networks including GMOS and GAW (Martin et al., 2017; Slemr et al., 2020).

B3.2 Hg measurements at Cape Point

Hg^0_{air} concentrations have been monitored at Cape Point with a Tekran Model 2537 A/B analyser since March 2007. Apart from the frequency at which the internal permeation source is checked, which is performed annually at Cape Point, the same sampling procedure at Mace Head (described in detail in the Section 5.2.2.1) is in operation at Cape Point. Moreover, to ensure comparability, the Tekran analysers at both Mace Head and Cape Point (as well as other GMOS sites) are operated and calibrated according to GMOS standard operating procedures (Sprovieri et al., 2016; Martin et al., 2017; Slemr et al., 2020).

We used hourly mean Hg^0_{air} measurements from Cape Point from January 2008 to December 2017. From the hourly means, we generated seasonal and annual mean time series.

B3.3 Chlorophyll-*a* concentrations over the South Atlantic and Southern oceans

Using the same daily global dataset from ICDC (detailed in Section 4.2.2.3), we generated a daily mean chlorophyll-*a* concentration time series for the same period as the Hg^0_{air} data, by averaging the concentrations over a spatial domain encompassing the South Atlantic and Southern oceans. From the daily data we also generated seasonal and annual mean time series.

Presented in Figure B3.1 is an overview of the dataset used for the southern hemisphere analysis, showing the spatial domain of the chlorophyll-*a* data averaging, the location of Cape Point, the daily mean chlorophyll-*a* concentrations and hourly mean Hg^0_{air} concentrations.

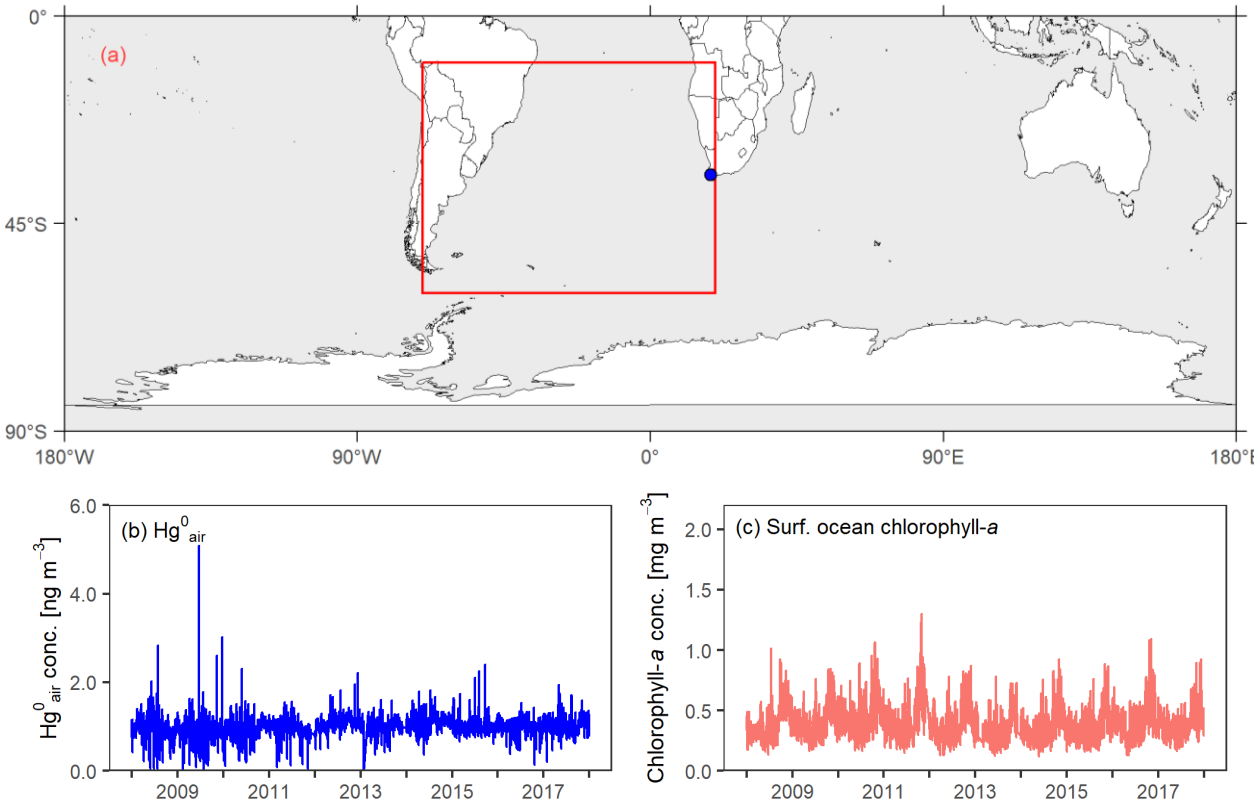

(d)

Variable [unit]	Resolution	Mean ± std. dev. (range)	No. of data points	Perc. data coverage [%]
Hg^0_{air} [ng m^{-3}]	Hourly	1.01 ± 0.12 (0.01–5.08)	76 615	100
Chl-*a* conc. [mg m^{-3}]	Daily	0.40 ± 0.14 (0.12–1.3)	4 383	100

Figure B3.1: Overview of the data analysis for the southern hemisphere. (a) Map showing the location of Cape Point (blue dot) as well as the spatial domain over which the chlorophyll-*a* data was averaged (red box; South Atlantic and Southern oceans; 60° W–10° E, 17° S–10 °S), (b) the hourly mean Hg^0_{air} time series from Cape Point and (c) daily mean surface ocean chlorophyll-*a* concentrations over the over the South Atlantic and Southern oceans. (d) Summary of the datasets, showing the mean, standard deviation (std. dev.), total number of data points (per temporal resolution) and percentage data coverage (i.e., proportion of valid or non-missing) over the analysis period.

References

Adams, H. M., Cui, X., Lamborg, C. H., and Schartup, A. T.: Dimethylmercury as a Source of Monomethylmercury in a Highly Productive Upwelling System, Environ. Sci. Technol., 58, 10591–10600, https://doi.org/10.1021/acs.est.4c01112, 2024.

Al-Sulaiti, M. M., Soubra, L., and Al-Ghouti, M. A.: The causes and effects of mercury and methylmercury contamination in the marine environment: A review, Current Pollution Reports, 8, 249–272, https://doi.org/10.1007/s40726-022-00226-7, 2022.

AMAP/UNEP: Technical Background Report to the Global Mercury Assessment 2018, Arctic Monitoring and Assessment Programme, Oslo, Norway/UN Environment Programme, Chemicals and Health Branch, Geneva, Switzerland, 2018.

Amos, H. M., Jacob, D. J., Streets, D. G., and Sunderland, E. M.: Legacy impacts of all-time anthropogenic emissions on the global mercury cycle, Global Biogeochem. Cy., 27, 410–421, https://doi.org/10.1002/gbc.20040, 2013.

Amos, H. M., Jacob, D. J., Kocman, D., Horowitz, H. M., Zhang, Y., Dutkiewicz, S., Horvat, M., Corbitt, E. S., Krabbenhoft, D. P., and Sunderland, E. M.: Global biogeochemical implications of mercury discharges from rivers and sediment burial, Environ. Sci. Technol., 48, 9514–9522, https://doi.org/10.1021/es502134t, 2014.

Andersson, M. E., Gårdfeldt, K., Wängberg, I., Sprovieri, F., Pirrone, N., and Lindqvist, O.: Seasonal and daily variation of mercury evasion at coastal and off shore sites from the Mediterranean Sea, Mar. Chem., 104, 214–226, https://doi.org/10.1016/j.marchem.2006.11.003, 2007.

Andersson, M. E., Gårdfeldt, K., Wängberg, I., and Strömberg, D.: Determination of Henry's law constant for elemental mercury, Chemosphere, 73, 587–592, https://doi.org/10.1016/j.Chemosphere.2008.05.067, 2008a.

Andersson, M. E., Sommar, J., Gårdfeldt, K., and Lindqvist, O.: Enhanced concentrations of dissolved gaseous mercury in the surface waters of the Arctic Ocean, Mar. Chem., 110, 190–194, https://doi.org/10.1016/j.marchem.2008.04.002, 2008b.

Andersson, M. E., Sommar, J., Gårdfeldt, K., and Jutterström, S.: Air–sea exchange of volatile mercury in the North Atlantic Ocean, Mar. Chem., 125, 1–7, https://doi.org/10.1016/j.marchem.2011.01.005, 2011.

Andersson, A., Rutgersson, A., and Sahlée, E.: Using eddy covariance to estimate air–sea gas transfer velocity for oxygen, Journal of Marine Systems, 159, 67–75. https://doi.org/10.1016/j.jmarsys.2016.02.008, 2016.

Angot, H., Barret, M., Magand, O., Ramonet, M., and Dommergue, A.: A 2-year record of atmospheric mercury species at a background Southern Hemisphere station on Amsterdam Island, Atmos. Chem. Phys., 14, 11461–11473, https://doi.org/10.5194/acp-14-11461-2014, 2014.

Angot, H., Dion, I., Vogel, N., Legrand, M., Magand, O., and Dommergue, A.: Multi-year record of atmospheric mercury at Dumont d'Urville, East Antarctic coast: continental outflow and oceanic influences, Atmospheric Chemistry and Physics, 16, 8265–8279, https://doi.org/10.5194/acp-16-8265-2016, 2016.

Ariya, P. A., Amyot, M., Dastoor, A., Deeds, D., Feinberg, A., Kos, G., Poulain, A., Ryjkov, A., Semeniuk, K., Subir, M. and Toyota, K., Mercury physicochemical and biogeochemical transformation in the atmosphere and at atmospheric interfaces: A review and future directions. Chemical reviews, 115, 3760–3802, https://doi.org/10.1021/cr500667e, 2015.

Baboukas, E., Sciare, J., and Mihalopoulos, N.: Spatial, temporal and interannual variability of methanesulfonate and non-sea-salt sulfate in rainwater in the southern Indian Ocean (Amsterdam, Crozet and Kerguelen Islands), J. Atmos. Chem., 48, 35–57, https://doi.org/10.1023/B:JOCH.0000034508.13326.cd, 2004.

Bagnato, E., Sproveri, M., Barra, M., Bitetto, M., Bonsignore, M., Calabrese, S., Di Stefano, V., Oliveri, E., Parello, F., and Mazzola, S.: The sea–air exchange of mercury (Hg) in the marine boundary layer of the Augusta basin (southern Italy): Concentrations and evasion flux, Chemosphere, 93, 2024–2032, https://doi.org/10.1016/j.chemosphere.2013.07.025, 2013.

Ballabio, C., Jiskra, M., Osterwalder, S., Borrelli, P., Montanarella, L., and Panagos, P.: A spatial assessment of mercury content in the European Union topsoil. Sci. Total Environ., 769, 144755, https://doi.org/10.1016/j.scitotenv.2020.144755, 2021.

Basu, N., Bastiansz, A., Dórea, J. G., Fujimura, M., Horvat, M., Shroff, E., Weihe, P., and Zastenskaya, I.: Our evolved understanding of the human health risks of mercury, Ambio, 52, 877–896, https://doi.org/10.1007/s13280-023-01831-6, 2023.

Baumann, Z., Jonsson, S., and Mason, R. P.: Geochemistry of mercury in the marine environment, Encyclopedia of Ocean Sciences, 6, 301–308, https://doi.org/10.1016/B978-0-12-409548-9.11096-6, 2019.

Bieser, J., Angot, H., Slemr, F., and Martin, L.: Atmospheric mercury in the Southern Hemisphere–Part 2: Source apportionment analysis at Cape Point station, South Africa, Atmos. Chem. Phys., 20, 10427–10439, https://doi.org/10.5194/acp-20-10427-2020, 2020.

Bieser, J., Amptmeijer, D., Daewel, U., Kuss, J., Soerensen, A. L., and Schrum, C., 2022: The 3D biogeochemical marine mercury cycling model MERCY v2.0 – linking atmospheric Hg to methyl mercury in fish, Geosci. Model Dev. Discuss., 1–59, https://doi.org/10.5194/gmd-16-2649-2022, 2022.

Bloom, N. and Fitzgerald, W. F.: Determination of volatile mercury species at the picogram level by low-temperature gas chromatography with cold-vapour atomic fluorescence detection, Anal. Chim. Acta, 208, 151-161, https://doi.org/10.1016/S0003-2670(00)80743-6, 1988.

Botha, R., Labuschagne, C., Williams, A. G., Bosman, G., Brunke, E. G., Rossouw, A., and Lindsay, R.: Characterising fifteen years of continuous atmospheric radon activity observations at Cape Point (South Africa), Atmos. Environ., 176, 30–3, https://doi.org/10.1016/j.atmosenv.2017.12.010, 2018.

Bowman, K. L., Hammerschmidt, C. R., Lamborg, C. H., and Swarr, G.: Mercury in the North Atlantic Ocean: The US GEOTRACES zonal and meridional sections, Deep Sea Research Part II: Topical Studies in Oceanography, 116, 251–261, https://doi.org/10.1016/j.dsr2.2014.07.004, 2014.

Bowman, K. L., Lamborg, C. H., and Agather, A. M.: A global perspective on mercury cycling in the ocean, Sci. Total Environ., 710, 136166, https://doi.org/10.1016/j.scitotenv.2019.136166, 2020.

Brasseur, G. P. and Jacob, D. J.: Modeling of Atmospheric Chemistry, Cambridge University Press, Cambridge, https://doi.org/10.1017/9781316544754, 2017.

Bratkič, A., Vahčič, M., Kotnik, J., Obu Vazner, K., Begu, E., Woodward, E. M. S., and Horvat, M.: Mercury presence and speciation in the South Atlantic Ocean along the 40° S transect, Global Biogeochem. Cy., 30, 105–119, https://doi.org/10.1002/2015GB005275, 2016.

Brunke, E. G., Labuschagne, C., Parker, B., Scheel, H. E., and Whittlestone, S.: Baseline air mass selection at Cape Point, South Africa: application of 222Rn and other filter criteria to CO2, Atmos. Environ., 38, 5693–5702, https://doi.org/10.1016/j.atmosenv.2004.04.024, 2004.

Brunke, E. G., Labuschagne, C., Ebinghaus, R., Kock, H. H., and Slemr, F.: Gaseous elemental mercury depletion events observed at Cape Point during 2007–2008, Atmos. Chem. Phys., 10, 1121–1131, https://doi.org/10.5194/acp-10-1121-2010, 2010.

Budnik, L. T. and Casteleyn, L.: Mercury pollution in modern times and its socio medical consequences, Sci. Total Environ., 654, 720–734, https://doi.org/10.1016/j.scitotenv.2018.10.408, 2019.

Carbone, F., Landis, M. S., Gencarelli, C. N., Naccarato, A., Sprovieri, F., De Simone, F., Hedgecock, I. M., and Pirrone, N.: Sea surface temperature variation linked to elemental mercury concentrations measured on Mauna Loa, Geophys. Res. Lett., 43, 7751–7757, https://doi.org/10.1002/2016GL069252, 2016.

Carpenter, L. J., Fleming, Z. L., Read, K. A., Lee, J. D., Moller, S. J., Hopkins, J. R., Purvis, R. M., Lewis, A. C., Müller, K., Heinold, B., Herrmann, H., Fomba, K. Wadinga, Pinxteren, D., Müller, C., Tegen, I., Wiedensohler, A., Müller, T., Niedermeier, N., Achterberg, Eric P., Patey, M. D., Kozlova, E. A., Heimann, M., Heard, D. E., Plane, J. M. C., Mahajan, A., Oetjen, H., Ingham, T., Stone, D., Whalley, L. K., Evans, M. J., Pilling, M. J., Leigh, R. J., Monks, P. S., Karunaharan, A., Vaughan, S., Arnold, S. R., Tschritter, J., Pöhler, D., Frieß, U., Holla, R., Mendes, L. M., Lopez, H., Faria, B., Manning, A. J., and Wallace, D. W. R.: Seasonal characteristics of tropical marine boundary layer air measured at the Cabo Verde Atmospheric Observatory, J. Atmos. Chem., 67, 87–140, https://doi.org/10.1007/s10874-011-9206-1, 2010.

Castro, P. J., Kellö, V., Cernušák, I., and Dibble, T. S.: Together, not separately, OH and O_3 oxidize $Hg^{(0)}$ to $Hg^{(II)}$ in the atmosphere, The Journal of Physical Chemistry A, 126, 8266–8279, https://doi.org/10.1021/acs.jpca.2c04364, 2022.

Chambers, S. D., Preunkert, S., Weller, R., Hong, S.-B., Humphries, R.S., Tositti, L., Angot, H., Legrand, M., Williams, A.G., Griffiths, A. D., Crawford, J., Simmons, J., Choi, T.J., Krummel, P. B., Molloy, S., Loh, Z., Galbally, I., Wilson, S., Magand, O., Sprovieri, F., Pirrone, N., and Dommergue, A.: Characterizing Atmospheric Transport Pathways to Antarctica and the Remote Southern Ocean using Radon-222, Front. Earth Sci., 6, 190, doi:10.3389/feart.2018.00190, 2018.

Chen, Y. S., Tseng, C. M., and Reinfelder, J. R.: Spatiotemporal variations in dissolved elemental mercury in the river-dominated and monsoon-influenced East China Sea: drivers, budgets, and implications, Environ. Sci. Technol., 54, 3988–3995, https://doi.org/10.1021/acs.est.9b06092, 2020.

Cheng, I., Zhang, L., Mao, H., Blanchard, P., Tordon, R., and Dalziel, J.: Seasonal and diurnal patterns of speciated atmospheric mercury at a coastal-rural and a coastal-urban site, Atmos. Environ., 82, 193–205, https://doi.org/10.1016/j.atmosenv.2013.10.016, 2014.

Cole, A. S., Steffen, A., Eckley, C. S., Narayan, J., Pilote, M., Tordon, R., Graydon, J. A., St. Louis, V. L., Xu, X., and Branfireun, B. A.: A survey of mercury in air and precipitation across Canada: Patterns and trends, Atmosphere, 5, 635–668, https://doi.org/10.3390/atmos5030635, 2014.

Cossa, D., Heimbürger, L. E., Lannuzel, D., Rintoul, S. R., Butler, E. C., Bowie, A. R., Averty, B., Watson, R. J., and Remenyi, T.: Mercury in the Southern Ocean, Geochim. Cosmochim. Ac., 75, 4037–4052, https://doi.org/10.1016/j.gca.2011.05.001, 2011.

Custódio, D., Ebinghaus, R., Spain, T. G., and Bieser, J.: Source apportionment of atmospheric mercury in the remote marine atmosphere: Mace Head GAW station, Irish western coast, Atmos. Chem. Phys., 20, 7929–7939, https://doi.org/10.5194/acp-20-7929-2020, 2020.

Custódio, D., Slemr, F., Pfaffhuber, K. A., Spain, T. G., Pankratov, F. F., Strigunova, I., Molepo, K., Skov, H., Bieser, J., and Ebinghaus, R.: Odds and ends of atmospheric mercury in Europe and over northern Atlantic Ocean: Temporal trends of 25 years of measurements, Atmos. Chem. Phys. Discuss., 1–20, https://doi.org/10.5194/acp-22-3827-2022, 2022.

Das, R., Wang, X., Khezri, B., Webster, R. D., Sikdar, P. K., and Datta, S.: Mercury isotopes of atmospheric particle bound mercury for source apportionment study in urban Kolkata, India, Elementa, 4, 000098, https://doi.org/10.12952/journal.elementa.000098, 2016.

Dastoor, A., Angot, H., Bieser, J., Brocza, F., Edwards, B., Feinberg, A., Feng, X., Geyman, B., Gournia, C., He, Y., Hedgecock, I. M., Ilyin, I., Kirk, J., Lin, C.-J., Lehnherr, I., Mason, R., McLagan, D., Muntean, M., Rafaj, P., Roy, E. M., Ryjkov, A., Selin, N. E., De Simone, F., Soerensen, A. L., Steenhuisen, F., Travnikov, O., Wang, S., Wang, X., Wilson, S., Wu, R., Wu, Q., Zhang, Y., Zhou, J., Zhu, W., and Zolkos, S.: The Multi-Compartment Hg Modeling and Analysis Project (MCHgMAP): mercury modeling to

support international environmental policy, Geosci. Model Dev., 18, 2747–2860, https://doi.org/10.5194/gmd-18-2747-2025, 2025.

Didan, K: MOD13C2 MODIS/Terra Vegetation Indices Monthly L3 Global 0.05Deg CMG V061, NASA EOSDIS Land Processes DAAC, https://doi.org/10.5067/MODIS/MOD13C2.061; obtained from the Land Processes Distributed Active Archive Center (LP DAAC), located at the U.S. Geological Survey (USGS) Earth Resources Observation and Science (EROS) Center (lpdaac.usgs.gov), modified and converted into netCDF file format at the Integrated Climate Data Center (ICDC), CEN, University of Hamburg, Germany, 2021 [last access: December, 2024].

Díez, S.: Human health effects of methylmercury exposure, Rev. Environ. Contam. Toxicol., 111–132, https://doi.org/10.1007/978-0-387-09647-6_3, 2009.

DiMento, B. P., Mason, R. P., Brooks, S. and Moore, C.: The impact of sea ice on the air–sea exchange of mercury in the Arctic Ocean, Deep Sea Research Part I: Oceanographic Research Papers, 144, 28–38, https://doi.org/10.1016/j.dsr.2018.12.001, 2019.

Driscoll, C. T., Mason, R. P., Chan, H. M., Jacob, D. J., and Pirrone, N.: Mercury as a global pollutant: sources, pathways, and effects, Environ. Sci. Technol., 47, 4967–4983, https://doi.org/10.1021/es305071v, 2013.

Dumarey, R., Temmerman, E., Adams, R., and Hoste, J.: The accuracy of the vapour-injection calibration method for the determination of mercury by amalgamation/cold-vapour atomic absorption spectrometry, Anal. Chim. Acta, 170, 337–340, https://doi.org/10.1016/S0003-2670(00)81759-6, 1985.

Durnford, D., Dastoor, A., Figueras-Nieto, D., and Ryjkov, A.: Long range transport of mercury to the Arctic and across Canada, Atmos. Chem. Phys., 10, 6063–6086, https://doi.org/10.5194/acp-10-6063-2010, 2010.

Ebinghaus, R., Kock, H. H., Coggins, A.M., Spain, T. G., Jennings, S. A., and Temme, C.: Long-term measurements of atmospheric mercury at Mace Head, Irish west coast, between 1995 and 2001, Atmos. Environ., 36, 5267–5276, https://doi.org/10.1016/S1352-2310(02)00691-X, 2002.

Ebinghaus, R., Jennings, S. G., Kock, H. H., Derwent, R. G., Manning, A. J., and Spain, T. G.: Decreasing trends in total gaseous mercury observations in baseline air at Mace Head, Ireland from 1996 to 2009, Atmos. Environ., 45, 3475–3480, https://doi.org/10.1016/j.atmosenv.2011.01.033, 2011.

Fairall, C. W., Yang, M., Bariteau, L., Edson, J. B., Helmig, D., McGillis, W., Pezoa, S., Hare, J.E., Huebert, B., and Blomquist, B.: Implementation of the Coupled Ocean-Atmosphere Response Experiment flux algorithm with CO_2, dimethyl sulfide, and O_3, Journal of Geophysical Research, 116, C00F09, https://doi.org/10.1029/2010JC006884, 2011.

Feinberg, A., Dlamini, T., Jiskra, M., Shah, V., and Selin, N. E.: Evaluating atmospheric mercury (Hg) uptake by vegetation in a chemistry-transport model, Environmental Science: Processes & Impacts, 24, 1303–1318, https://doi.org/10.1039/d2em00032f, 2022.

Feinberg, A., Selin, N. E., Braban, C. F., Chang, K. L., Custódio, D., Jaffe, D. A., Kyllönen, K., Landis, M. S., Leeson, S. R., Luke, W., and Molepo, K. M.: Unexpected anthropogenic emission decreases explain recent atmospheric mercury concentration declines, Proc. Natl. Acad. Sci. USA, 121, e2401950121, https://doi.org/10.1073/pnas.2401950121, 2024.

Field, C. B., Behrenfeld, M. J., Randerson, J. T., and Falkowski, P.: Primary production of the biosphere: integrating terrestrial and oceanic components, Science, 281, 237–240, https://doi.org/10.1126/science.281.5374.237, 1998.

Fitzgerald, W. F. and Gill, G. A.: Subnanogram determination of mercury by two-stage gold amalgamation and gas phase detection applied to atmospheric analysis, Anal. Chem., 51, 1714–1720, https://doi.org/10.1021/ac50047a030, 1979.

Floreani, F., Acquavita, A., Petranich, E., and Covelli, S.: Diurnal fluxes of gaseous elemental mercury from the water-air interface in coastal environments of the northern Adriatic Sea, Sci. Total Environ., 668, 925–935, https://doi.org/10.1016/j.scitotenv.2019.03.012, 2019.

Friedli, H. R., Arellano Jr, A. F., Cinnirella, S., and Pirrone, N.: Mercury emissions from global biomass burning: Spatial and temporal distribution, in: Mercury Fate and Transport in the Global Atmosphere: Emissions, Measurements and Models, edited by: Mason, R. and Pirrone, N., Springer, Boston, MA, US, 193–220, https://doi.org/10.1007/978-0-387-93958-2_8, 2009.

Fu, X. W., Zhang, H., Yu, B., Wang, X., Lin, C. J., and Feng, X. B.: Observations of atmospheric mercury in China: a critical review, Atmos. Chem. Phys., 15, 9455–9476, https://doi.org/10.5194/acp-15-9455-2015, 2015.

Fu, X., Zhang, H., Liu, C., Zhang, H., Lin, C.J., and Feng, X.: Significant seasonal variations in isotopic composition of atmospheric total gaseous mercury at forest sites in China caused by vegetation and mercury sources, Environ. Sci. Technol., 53, 13748–13756, https://doi.org/10.1021/acs.est.9b05016, 2019.

Gårdfeldt, K., Sommar, J., Ferrara, R., Ceccarini, C., Lanzillotta, E., Munthe, J., Wängberg, I., Lindqvist, O., Pirrone, N., Sprovieri, F., and Pesenti, E.: Evasion of mercury from coastal and open waters of the Atlantic Ocean and the Mediterranean Sea, Atmos. Environ., 37, 73–84, https://doi.org/10.1016/S1352-2310(03)00238-3, 2003.

Gay, D. A., Schmeltz, D., Prestbo, E., Olson, M., Sharac, T., and Tordon, R.: The Atmospheric Mercury Network: measurement and initial examination of an ongoing atmospheric mercury record across North America, Atmos. Chem. Phys., 13, 11339–11349, https://doi.org/10.5194/acp-13-11339-2013, 2013.

GEBCO Compilation Group (2020) GEBCO 2020 Grid (doi:10.5285/a29c5465-b138-234d-e053-6c86abc040b9).

Gregg, W. W. and Rousseaux, C. S.: Global ocean primary production trends in the modern ocean color satellite record (1998–2015), Environmental Research Letters, 14, 124011, https://doi.org.10.1088/1748-9326/ab4667, 2019.

Grégoire, D. S. and Poulain, A. J.: A little bit of light goes a long way: the role of phototrophs on mercury cycling, Metallomics, 6, 396–407, https://doi.org/10.1039/C3MT00312D, 2014.

Hedgecock, I. M., and Pirrone, N.: Mercury and photochemistry in the marine boundary layer—modelling studies suggest the in situ production of reactive gas phase mercury, Atmos. Environ., 35, 3055–3062, https://doi.org/10.1016/S1352-2310(01)00109-1, 2001.

Hedgecock, I. M. and Pirrone, N.: Chasing quicksilver: Modeling the atmospheric lifetime of Hg0(g) in the marine boundary layer at various latitudes, Environ. Sci. Technol., 38, 69–76, https://doi.org/10.1021/es034623z, 2004.

Hersbach, H., Bell, B., Berrisford, P., Hirahara, S., Horányi, A., Muñoz-Sabater, J., Nicolas, J., Peubey, C., Radu, R., Schepers, D., and Simmons, A.: The ERA5 global reanalysis, Q. J. Roy. Meteor. Soc., 146, 1999–2049, https://doi.org/10.1002/qj.3803, 2020.

Holloway, T. and Littlefield, C.: Intercontinental Air Pollution Transport: Links to Environmental Health, in: Encyclopedia of Environmental Health, edited by: Nriagu, J. O., Elsevier, 266–272, https://doi.org/10.1016/B978-0-444-52272-6.00529-8, 2011.

Horowitz, H. M., Jacob, D. J., Zhang, Y., Dibble, T. S., Slemr, F., Amos, H. M., Schmidt, J. A., Corbitt, E. S., Marais, E. A., and Sunderland, E. M.: A new mechanism for atmospheric mercury redox chemistry: implications for the global mercury budget, Atmos. Chem. Phys., 17, 6353–6371, https://doi.org/10.5194/acp-17-6353-2017, 2017.

Horvat, M., Kotnik, J., Logar, M., Fajon, V., Zvonarić, T., and Pirrone, N.: Speciation of mercury in surface and deep-sea waters in the Mediterranean Sea, Atmos. Environ., 37, 93–108, https://doi.org/10.1016/S1352-2310(03)00249-8, 2003.

Jiskra, M., Sonke, J. E., Obrist, D., Bieser, J., Ebinghaus, R., Myhre, C. L., Pfaffhuber, K. A., Wängberg, I., Kyllönen, K., Worthy, D., and Martin, L. G.: A vegetation control on seasonal variations in global atmospheric mercury concentrations, Nat. Geosci., 11, 244–250, https://doi.org/10.1038/s41561-018-0078-8, 2018.

Jiskra, M., Heimbürger-Boavida, L. E., Desgranges, M. M., Petrova, M. V., Dufour, A., Ferreira-Araujo, B., Masbou, J., Chmeleff, J., Thyssen, M., Point, D., and Sonke, J. E.: Mercury stable isotopes constrain atmospheric sources to the ocean, Nature, 597, 678–682, https://doi.org/10.1038/s41586-021-03859-8, 2021.

Kalinchuk, V. V., Lopatnikov, E. A., Astakhov, A. S., Ivanov, M. V., and Hu, L.: Distribution of atmospheric gaseous elemental mercury (Hg^0) from the Sea of Japan to the Arctic, and Hg^0 evasion fluxes in the Eastern Arctic Seas: results from a joint Russian-Chinese cruise in fall 2018, Sci. Total Environ., 753, 142003, https://doi.org/10.1016/j.scitotenv.2020.142003, 2021.

Kalinchuk, V. V.: Gaseous elemental mercury and its evasion fluxes in the marine boundary layer of the marginal seas of the northwestern Pacific: Results from two cruises in September–December 2019, Sci. Total Environ., 858, 159711, https://doi.org/10.1016/j.scitotenv.2022.159711,2023.

Kalnay, E., Kanamitsu, M., Kistler, R., Collins, W., Deaven, D., Gandin, L., Iredell, M., Saha, S., White, G., Woollen, J., and Zhu, Y.: The NCEP/NCAR 40-year reanalysis project, B. Am. Meteorol. Soc., 77, 437–472, https://doi.org/10.1175/1520-0477(1996)077<0437:TNYRP>2.0.CO;2, 1996.

Kim, M. K., Won, A. Y., and Zoh, K. D.: The production of dissolved gaseous mercury from methylmercury photodegradation at different salinity, Desalin. Water Treat., 57, 610–619, https://doi.org/10.1080/19443994.2014.986829, 2016.

Koenig, A. M., Magand, O., Laj, P., Andrade, M., Moreno, I., Velarde, F., Salvatierra, G., Gutierrez, R., Blacutt, L., Aliaga, D., and Reichler, T.: Seasonal patterns of atmospheric

mercury in tropical South America as inferred by a continuous total gaseous mercury record at Chacaltaya station (5240 m) in Bolivia, Atmos. Chem. Phys., 21, 3447–3472, https://doi.org/10.5194/acp-21-3447-2021, 2021.

Koenig, A. M., Sonke, J. E., Magand, O., Andrade, M., Moreno, I., Velarde, F., Forno, R., Gutierrez, R., Blacutt, L., Laj, P., and Ginot, P.: Evidence for interhemispheric mercury exchange in the Pacific Ocean upper troposphere, J. Geophys. Res.-Atmospheres, 127, e2021JD036283, https://doi.org/10.1029/2021JD036283, 2022.

Koenig, A. M., Magand, O., Verreyken, B., Brioude, J., Amelynck, C., Schoon, N., Colomb, A., Ferreira Araujo, B., Ramonet, M., Sha, M.K., and Cammas, J. P.: Mercury in the free troposphere and bidirectional atmosphere–vegetation exchanges–insights from Maïdo mountain observatory in the Southern Hemisphere tropics, Atmos. Chem. Phys., 23, 1309–1328, https://doi.org/10.5194/acp-23-1309-2023, 2023.

Kock, H. H., Bieber, E., Ebinghaus, R., Spain, T. G., and Thees, B.: Comparison of long-term trends and seasonal variations of atmospheric mercury concentrations at the two European coastal monitoring stations Mace Head, Ireland, and Zingst, Germany, Atmos. Environ., 39, 7549–7556, https://doi.org/10.1016/j.atmosenv.2005.02.059, 2005.

Kotnik, J., Horvat, M., Tessier, E., Ogrinc, N., Monperrus, M., Amouroux, D., Fajon, V., Gibičar, D., Žižek, S., Sprovieri, F., and Pirrone, N.: Mercury speciation in surface and deep waters of the Mediterranean Sea, Mar. Chem., 107, 13–30, https://doi.org/10.1016/j.marchem.2007.02.012, 2007.

Kuss, J., Zülicke, C., Pohl, C., and Schneider, B.: Atlantic mercury emission determined from continuous analysis of the elemental mercury sea-air con centration difference within transects between 50° N and 50° S, Global Biogeochem. Cy., 25, GB3021, https://doi.org/10.1029/2010GB003998, 2011.

Labuschagne, C., Kuyper, B., Brunke, E-G., Mkololo, T., van der Spuy, D., Martin, L., Mbambalala, E., Parker, B., Khan, A. H., Davies-Coleman, M. T., Schallcross, D. E., and Joubert, W.: A review of four decades of atmospheric trace gas measurements at Cape Point, South Africa, Transactions of the Royal Society of South Africa, 73, 113–132, https://doi.org/10.1080/0035919X.2018.1477854, 2018.

Lan, X., Talbot, R., Castro, M., Perry, K., and Luke, W.: Seasonal and diurnal variations of atmospheric mercury across the US determined from AMNet monitoring data, Atmos. Chem. Phys., 12, 10569–10582, https://doi.org/10.5194/acp-12-10569-2012, 2012.

Lanzillotta, E., and Ferrara, R.: Daily trend of dissolved gaseous mercury concentration in coastal seawater of the Mediterranean basin, Chemosphere, 45, 935–940, https://doi.org/10.1016/S0045-6535(01)00021-2, 2001.

Lamborg, C., Bowman, K., Hammerschmidt, C., Gilmour, C., Munson, K., Selin, N., and Tseng, C. M.: Mercury in the anthropocene ocean, Oceanography, 27, 76–87, https://doi.org/10.5670/oceanog.2014.11, 2014.

Lamborg, C. H., Hansel, C. M., Bowman, K. L., Voelker, B. M., Marsico, R. M., Oldham, V. E., Swarr, G. J., Zhang, T., and Ganguli, P. M.: Dark reduction drives evasion of mercury from the ocean, Front. Environ. Chem., 2, 659085, https://doi.org/10.3389/fenvc.2021.659085, 2021.

Laurier, F. J., Mason, R. P., Whalin, L., and Kato, S.: Reactive gaseous mercury formation in the North Pacific Ocean's marine boundary layer: A potential role of halogen chemistry, J. Geophys. Res.-Atmospheres, https://doi.org/10.1029/2003JD003625, 2003.

Lehnherr, I.: Methylmercury biogeochemistry: a review with special reference to Arctic aquatic ecosystems, Environ. Rev., 22, 229–243, https://doi.org/10.1139/er-2013-0059, 2014.

Lee, C. S. and Fisher, N. S.: Microbial generation of elemental mercury from dissolved methylmercury in seawater, Limnology and oceanography, 64, 679–693, https://doi.org/10.1002/lno.11068, 2019.

Li, C., Sonke, J. E., Le Roux, G., Piotrowska, N., Van der Putten, N., Roberts, S. J., Daley, T., Rice, E., Gehrels, R., Enrico, M., and Mauquoy, D.: Unequal anthropogenic enrichment of mercury in earth's northern and southern hemispheres, ACS Earth and Space Chemistry, 4, 2073–2081, https://doi.org/10.1021/acsearthspacechem.0c00220, 2020.

Li, C., Enrico, M., Magand, O., Araujo, B. F., Le Roux, G., Osterwalder, S., Dommergue, A., Bertrand, Y., Brioude, J., De Vleeschouwer, F., and Sonke, J. E.: A peat core Hg stable isotope reconstruction of Holocene atmospheric Hg deposition at Amsterdam Island (37.8°S), Geochim. Cosmochim. Ac., 341, 62–74, https://doi.org/10.1016/j.gca.2022.11.024, 2023.

Li, L., Wu, P., Zhang, P., Huang, S., and Zhang, Y.: An improved model for air–sea exchange of elemental mercury in MITgcm-ECCOv4-Hg: the role of surfactants and waves, Geosci. Model Dev., 17, 8683–8695, https://doi.org/10.5194/gmd-17-8683-2024, 2024.

Liang, X., Zhu, N., Johs, A., Chen, H., Pelletier, D. A., Zhang, L., Yin, X., Gao, Y., Zhao, J., and Gu, B.: Mercury reduction, uptake, and species transformation by freshwater alga

Chlorella vulgaris under sunlit and dark conditions, Environ. Sci. Technol., 56, 4961–4969, https://doi.org/10.1021/acs.est.1c06558, 2022.

Liss, P. S. and Merlivat, L.: Air–sea gas exchange rates: Introduction and synthesis, in: The role of air–sea exchange in geochemical cycling, edited by: Buat-Ménard, P., Springer, Dordrecht, 113–127, https://doi.org/10.1007/978-94-009-4738-2_5, 1986.

Liu, W. and Wang, W.: The impact of anomalous biomass burning on phytoplankton and surface ocean carbon pool in the Indo-China Peninsula, Journal of Geophysical Research: Oceans, 130, e2024JC022070, https://doi.org/10.1029/2024JC022070, 2025.

Lyman, S. N., Cheng, I., Gratz, L. E., Weiss-Penzias, P., and Zhang, L.: An updated review of atmospheric mercury, Sci. Total Environ., 707, 135575, https://doi.org/10.1016/j.scitotenv.2019.135575, 2020.

Magand, O. and Dommergue, A.: Continuous measurements of atmospheric mercury at Amsterdam Island (L2), Aeris, 2021.

Magand, O., Angot, H., Bertrand, Y., Sonke, J. E., Laffont, L., Duperray, S., Collignon, L., Boulanger, D., and Dommergue, A.: Over a decade of atmospheric mercury monitoring at Amsterdam Island in the French Southern and Antarctic Lands, Scientific Data, 10, 836, https://doi.org/10.1038/s41597-023-02740-9, 2023.

Martin, L. G., Labuschagne, C., Brunke, E. G., Weigelt, A., Ebinghaus, R., and Slemr, F.: Trend of atmospheric mercury concentrations at Cape Point for 1995–2004 and since 2007, Atmos. Chem. Phys., 17, 2393–2399, https://doi.org/10.5194/acp-17-2393-2017, 2017.

Marumoto, K., Suzuki, N., Shibata, Y., Takeuchi, A., Takami, A., Fukuzaki, N., Kawamoto, K., Mizohata, A., Kato, S., Yamamoto, T., and Chen, J.: Long-term observation of atmospheric speciated mercury during 2007–2018 at Cape Hedo, Okinawa, Japan, Atmosphere, 10, 362, https://doi.org/10.3390/atmos10070362, 2019.

Mason, R. P. and Fitzgerald, W. F.: The distribution and biogeochemical cycling of mercury in the equatorial Pacific Ocean, Deep Sea Research Part I: Oceanographic Research Papers, 40, 1897–1924, https://doi.org/10.1016/0967-0637(93)90037-4, 1993.

Mason, R. P., Choi, A. L., Fitzgerald, W. F., Hammerschmidt, C. R., Lamborg, C. H., Soerensen, A. L., and Sunderland, E. M.: Mercury biogeochemical cycling in the ocean and policy implications, Environ. Res., 119, 101–117, https://doi.org/10.1016/j.envres.2012.03.013, 2012.

Mason, R. P., Hammerschmidt, C. R., Lamborg, C. H., Bowman, K. L., Swarr, G. J., and Shelley, R. U.: The air–sea exchange of mercury in the low latitude Pacific and Atlantic Oceans, Deep Sea Research Part I: Oceanographic Research Papers, 122, 17–28, https://doi.org/10.1016/j.dsr.2017.01.015, 2017.

McGillis, W. R., Edson, J. B., Hare, J. E., and Fairall, C. W.: Direct covariance air-sea CO2 fluxes, J. Geophys. Res.-Oceans, 106, 16729–16745, https://doi.org/10.1029/2000JC000506, 2001.

Miller, J. M., Moody, J. L., Harris, J. A., and Gaudry, A.: A 10-year trajectory flow climatology for Amsterdam Island, 1980–1989, Atmos. Environ. Part A. General Topics, 27, 1909-1916, https://doi.org/10.1016/0960-1686(93)90296-B, 1993.

Molepo, K. M., Bieser, J., Koenig, A. M., Hedgecock, I. M., Ebinghaus, R., Dommergue, A., Magand, O., Angot, H., Travnikov, O., Martin, L., and Labuschagne, C.: Constraining elemental mercury air–sea exchange using long-term ground-based observations, EGUsphere [preprint], https://doi.org/10.5194/egusphere-2024-3722, 2024.

NASA Goddard Space Flight Center, Ocean Ecology Laboratory, Ocean Biology Processing Group: MODIS-Aqua Daily Global Sea Surface Chlorophyll-a Concentration Data, NASA OB.DAAC, https://doi.org/10.5067/AQUA/MODIS/L3M/CHL/2022, 2022 [last access: 26 November 2024].

Nerentorp Mastromonaco, M. G., Gårdfeldt, K., and Langer, S.: Mercury flux over West Antarctic Seas during winter, spring and summer, Mar. Chem., 193, 44–54, https://doi.org/10.1016/j.marchem.2016.08.005, 2017.

Nightingale, P. D., Malin, G., Law, C. S., Watson, A. J., Liss, P. S., Liddicoat, M. I., Boutin, J., and Upstill-Goddard, R. C.: In situ evaluation of air-sea gas exchange parameterizations using novel conservative and volatile tracers, Global Biogeochem. Cy., 14, 373–387, https://doi.org/10.1029/1999GB900091, 2000.

Obrist, D., Kirk, J. L., Zhang, L., Sunderland, E. M., Jiskra, M., and Selin, N. E.: A review of global environmental mercury processes in response to human and natural perturbations: Changes of emissions, climate, and land use, Ambio, 47, 116–140, https://doi.org/10.1007/s13280-017-1004-9, 2018.

OECD: Risk Reduction Monography No. 4: Mercury, Background and National Experience with Reducing Risk, Environmental Directorate, Paris, France, 1995.

Osterwalder, S., Nerentorp, M., Zhu, W., Jiskra, M., Nilsson, E., Nilsson, M. B., Rutgersson, A., Soerensen, A. L., Sommar, J., Wallin, M. B., and Wängberg, I.: Critical

Observations of Gaseous Elemental Mercury Air-Sea Exchange, Global Biogeochem. Cy., 35, e2020GB006742, https://doi.org/10.1029/2020GB006742, 2021.

Outridge, P. M., Mason, R. P., Wang, F., Guerrero, S., and Heimburger-Boavida, L. E.: Updated global and oceanic mercury budgets for the United Nations Global Mercury Assessment 2018, Environ. Sci. Technol., 52, 11466-11477, https://doi.org/10.1021/acs.est.8b01246, 2018.

Pereira, R., Ashton, I., Sabbaghzadeh, B., Shutler, J. D., and Upstill-Goddard, R. C.: Reduced air–sea CO2 exchange in the Atlantic Ocean due to biological surfactants. Nature Geoscience, 11(7), 492–496, https://doi.org/10.1038/s41561-018-0136-2, 2018.

Pyle, D. M. and Mather, T. A.: The importance of volcanic emissions for the global atmospheric mercury cycle, Atmos. Environ., 37, 5115–5124, https://doi.org/10.1016/j.atmosenv.2003.07.011, 2003.

R Core Team: R: A Language and Environment for Statistical Computing, R Foundation for Statistical Computing, Vienna, Austria, https://www.R-project.org/, 2025.

Read, K. A., Neves, L.M., Carpenter, L.J., Lewis, A.C., Fleming, Z.L., and Kentisbeer, J.: Four years (2011–2015) of total gaseous mercury measurements from the Cape Verde Observatory Atmospheric Observatory, Atmos. Chem. Phys., 17, 5393–5406, https://doi.org/10.5194/acp-17-5393-2017, 2017.

Revelle, W.: psych: Procedures for Psychological, Psychometric, and Personality Research, Northwestern University, Evanston, Illinois, R package version 2.5.3, https://CRAN.R-project.org/package=psych, 2025.

Saiz-Lopez, A., Sitkiewicz, S. P., Roca-Sanjuán, D., Oliva-Enrich, J. M., Dávalos, J. Z., Notario, R., Jiskra, M., Xu, Y., Wang, F., Thackray, C. P., and Sunderland, E. M.: Photoreduction of gaseous oxidized mercury changes global atmospheric mercury speciation, transport and deposition, Nat. Commun., 9, 4796, https://doi.org/10.1038/s41467-018-07075-3, 2018.

Santos, J. P., Amouroux, D., and Slaveykova, V. I.: Dissolved elemental mercury accumulation by freshwater phytoplankton species: A pilot study, J. Hazard. Mater. Lett., 5, 100128, https://doi.org/10.1016/j.hazl.2024.100128, 2024.

Schery, S. D. and Huang, S.: An estimate of the global distribution of radon emissions from the ocean, Geophys. Res. Lett., 31, L19104, doi: 10.1029/2004GL021051, 2004.Shah, V., Jacob, D. J., Thackray, C. P., Wang, X., Sunderland, E. M., Dibble, T. S., Saiz-Lopez, A., Černušák, I., Kellö, V., Castro, P. J., and Wu, R.: Improved mechanistic

model of the atmospheric redox chemistry of mercury, Environ. Sci. Technol., 55, 14445–14456, https://doi.org/10.1021/acs.est.1c03160, 2021.

Shah, V., Jacob, D. J., Thackray, C. P., Wang, X., Sunderland, E. M., Dibble, T. S., Saiz-Lopez, A., Černušák, I., Kellö, V., Castro, P. J. and Wu, R.: Improved mechanistic model of the atmospheric redox chemistry of mercury. Environ. Sci. Technol., 55, 14445–14456, https://doi.org/10.1021/acs.est.1c03160, 2021.

Slemr, F., Brunke, E. G., Whittlestone, S., Zahorowski, W., Ebinghaus, R., Kock, H. H., and Labuschagne, C.: 222Rn-calibrated mercury fluxes from terrestrial surface of southern Africa, Atmos. Chem. Phys., 13, 6421–6428, https://doi.org/10.5194/acp-13-6421-2013, 2013.

Slemr, F., Angot, H., Dommergue, A., Magand, O., Barret, M., Weigelt, A., Ebinghaus, R., Brunke, E. G., Pfaffhuber, K. A., Edwards, G., and Howard, D.: Comparison of mercury concentrations measured at several sites in the Southern Hemisphere, Atmos. Chem. Phys., 15, 3125–3133, https://doi.org/10.5194/acp-15-3125-2015, 2015.

Slemr, F., Martin, L., Labuschagne, C., Mkololo, T., Angot, H., Magand, O., Dommergue, A., Garat, P., Ramonet, M., and Bieser, J.: Atmospheric mercury in the Southern Hemisphere–Part 1: Trend and inter-annual variations in atmospheric mercury at Cape Point, South Africa, in 2007–2017, and on Amsterdam Island in 2012–2017, Atmos. Chem. Phys., 20, 7683–7692, https://doi.org/10.5194/acp-20-7683-2020, 2020.

Soerensen, A. L., Skov, H., Jacob, D. J., Soerensen, B. T., and Johnson, M. S.: Global concentrations of gaseous elemental mercury and reactive gaseous mercury in the marine boundary layer, Environ. Sci. Technol., 44, 7425–7430, https://doi.org/10.1021/es903839n, 2010a.

Soerensen, A. L., Sunderland, E. M., Holmes, C. D., Jacob, D. J., Yantosca, R. M., Skov, H., Christensen, J. H., Strode, S. A., and Mason, R. P.: An improved global model for air–sea exchange of mercury: High concentrations over the North Atlantic, Environ. Sci. Technol., 44, 8574–8580, https://doi.org/10.1021/es102032g, 2010b.

Soerensen, A. L., Jacob, D. J., Streets, D. G., Witt, M. L., Ebinghaus, R., Mason, R. P., Andersson, M., and Sunderland, E. M.: Multi-decadal decline of mercury in the North Atlantic atmosphere explained by changing subsurface seawater concentrations, Geophysical Research Letters, 39, L21810, https://doi.org/10.1029/2012GL053736, 2012.

Soerensen, A. L., Mason, R. P., Balcom, P. H., and Sunderland, E. M.: Drivers of surface ocean mercury concentrations and air–sea exchange in the West Atlantic Ocean, Environ. Sci. Technol., 47, 7757–7765, https://doi.org/10.1021/es401354q, 2013.

Soerensen, A. L., Mason, R. P., Balcom, P. H., Jacob, D. J., Zhang, Y., Kuss, J., and Sunderland, E. M.: Elemental mercury concentrations and fluxes in the tropical atmosphere and ocean, Environ. Sci. Technol., 48, 11312–11319, https://doi.org/10.1021/es503109p, 2014.

Soerensen, A. L., Jacob, D. J., Schartup, A. T., Fisher, J. A., Lehnherr, I., St. Louis, V. L., Heimbürger, L. E., Sonke, J. E., Krabbenhoft, D. P., and Sunderland, E. M.: A mass budget for mercury and methylmercury in the Arctic Ocean, Global Biogeochem. Cycles, 30, 560–575, https://doi.org/10.1002/2015GB005280, 2016.

Sommar, J., Andersson, M. E., and Jacobi, H. W.: Circumpolar measurements of speciated mercury, ozone and carbon monoxide in the boundary layer of the Arctic Ocean, Atmos. Chem. Phys., 10, 5031–5045, https://doi.org/10.5194/acp-10-5031-2010, 2010.

Sommar, J., Osterwalder, S., and Zhu, W.: Recent advances in understanding and measurement of Hg in the environment: Surface-atmosphere exchange of gaseous elemental mercury (Hg^0), Sci. Total Environ., 721, 137648, https://doi.org/10.1016/j.scitotenv.2020.137648, 2020.

Sonke, J. E., Angot, H., Zhang, Y., Poulain, A., Björn, E., and Schartup, A.: Global change effects on biogeochemical mercury cycling, Ambio, 52, 853–876, https://doi.org/10.1007/s13280-023-01855-y, 2023.

Sprovieri, F., Pirrone, N., Ebinghaus, R., Kock, H. and Dommergue, A.: A review of worldwide atmospheric mercury measurements, Atmos. Chem. Phys., 10, 8245–8265, https://doi.org/10.5194/acp-10-8245-2010, 2010.

Sprovieri, F., Pirrone, N., Bencardino, M., D'Amore, F., Carbone, F., Cinnirella, S., Mannarino, V., Landis, M., Ebinghaus, R., Weigelt, A., and Brunke, E. G.: Atmospheric mercury concentrations observed at ground-based monitoring sites globally distributed in the framework of the GMOS network, Atmos. Chem. Phys., 16, 11915–11935, https://doi.org/10.5194/acp-16-11915-2016, 2016.

Streets, D. G., Devane, M. K., Lu, Z., Bond, T. C., Sunderland, E. M., and Jacob, D. J.: All-time releases of mercury to the atmosphere from human activities, Environ. Sci. Technol., 45, 10485–10491, https://doi.org/10.1021/es202765m, 2011.

Streets, D. G., Horowitz, H. M., Jacob, D. J., Lu, Z., Levin, L., Ter Schure, A. F., and Sunderland, E. M.: Total mercury released to the environment by human activities, Environ. Sci. Technol., 51, 5969–5977, https://doi.org/10.1021/acs.est.7b00451, 2017.

Strode, S. A., Jaeglé, L., Selin, N. E., Jacob, D. J., Park, R. J., Yantosca, R. M., Mason, R. P., and Slemr, F.: Air-sea exchange in the global mercury cycle, Global Biogeochem. Cy., 21, GB1017, https://doi.org/10.1029/2006GB002766, 2007.

Stein, A. F., Draxler, R. R., Rolph, G. D., Stunder, B.J., Cohen, M. D., and Ngan, F.: NOAA's HYSPLIT atmospheric transport and dispersion modeling system, B. Am. Meteorol. Soc., 96, 2059–2077, https://doi.org/10.1175/BAMS-D-14-00110.1, 2015.

Styszko, K., Szramowiat, K., Kistler, M., Kasper-Giebl, A., Samek, L., Furman, L., Pacyna, J., and Gołaś, J.: Mercury in atmospheric aerosols: a preliminary case study for the city of Krakow, Poland, C. R. Chim., 18, 1183–1191, https://doi.org/10.1016/j.crci.2015.05.016, 2015.

Sunderland, E. M. and Mason, R. P.: Human impacts on open ocean mercury concentrations, Global Biogeochem. Cy., 21, GB4022, https://doi.org/10.1029/2006GB002876, 2007.

Takeuchi, T., Morikawa, N., Matsumoto, H., and Shiraishi, Y.: A pathological study of Minamata disease in Japan, Acta Neuropathol., 2, 40–57, https://doi.org/10.1007/BF00685743, 1962.

Tang, Y., Wu, Q., Wang, S., Zhang, M., Zhang, Y., and Qiao, F.: Enhanced daytime atmospheric mercury in the marine boundary layer in the South Oceans, Sci. Total Environ., 892, 164691, https://doi.org/10.1016/j.scitotenv.2023.164691, 2023.

Tang, K., Song, Z., Fu, X., Zhang, Y., Zhang, H., Sun, Y., Zhang, H., Wu, X., Deng, Q., Zhang, L., and Suratman, S.: An interhemispheric difference in atmospheric gaseous elemental mercury isotopes reveals a new insight in oceanic mercury emissions, J. Geophys. Res. Atmos., 130, e2024JD042178, https://doi.org/10.1029/2024JD042178, 2025.

Tassone, A., Magand, O., Naccarato, A., Martino, M., Amico, D., Sprovieri, F., Leuridan, H., Bertrand, Y., Ramonet, M., Pirrone, N., and Dommergue, A.: Seven-year monitoring of mercury in wet precipitation and atmosphere at the Amsterdam Island GMOS station, Heliyon, 9, https://doi.org/10.1016/j.heliyon.2023.e14608, 2023.

Temme, C., Slemr, F., Ebinghaus, R., and Einax, J. W.: Distribution of mercury over the Atlantic Ocean in 1996 and 1999–2001, Atmos. Environ., 37, 1889–1897, https://doi.org/10.1016/S1352-2310(03)00069-4, 2003.

Torres-Rodriguez, N., Yuan, J., Petersen, S., Dufour, A., González-Santana, D., Chavagnac, V., Planquette, H., Horvat, M., Amouroux, D., Cathalot, C., Sun, R., Sonke, J. E., Luther, G. W., and Heimbürger-Boavida, L. E.: Mercury fluxes from hydrothermal venting at mid-ocean ridges constrained by measurements, Nature Geoscience, 17, 51–57, https://doi.org/10.1038/s41561-023-01341-w, 2024.

Travnikov, O.: Contribution of the intercontinental atmospheric transport to mercury pollution in the Northern Hemisphere, Atmos. Environ., 39, 7541–7548, https://doi.org/10.1016/j.atmosenv.2005.07.066, 2005.

Travnikov, O., Angot, H., Artaxo, P., Bencardino, M., Bieser, J., d'Amore, F., Dastoor, A., De Simone, F., Diéguez, M. D. C., Dommergue, A., and Ebinghaus, R.: Multi-model study of mercury dispersion in the atmosphere: atmospheric processes and model evaluation, Atmos. Chem. Phys., 17, 5271–5295, https://doi.org/10.5194/acp-17-5271-2017, 2017.

Tseng, C. M., Liu, C. S., and Lamborg, C.: Seasonal changes in gaseous elemental mercury in relation to monsoon cycling over the northern South China Sea, Atmos. Chem. Phys., 12, 7341–7350, https://doi.org/10.5194/acp-12-7341-2012, 2012.

US EPA: Mercury Study Report To Congress, Volume VII: Characterization Of Human Health And Wildlife Risks From Mercury Exposure In The United States, Office of Air Quality Planning & Standards and Office of Research and Development, Washington, DC, 1997.

Wang, Y., Li, Y., Liu, G., Wang, D., Jiang, G., and Cai, Y.: Elemental mercury in natural waters: occurrence and determination of particulate Hg^0, Environ. Sci. Technol., 49, 9742–9749, https://doi.org/10.1021/acs.est.5b01940, 2015.

Wang, J., Xie, Z., Wang, F., and Kang, H.: Gaseous elemental mercury in the marine boundary layer and air–sea flux in the Southern Ocean in austral summer, Sci. Total Environ., 603, 510–518, https://doi.org/10.1016/j.scitotenv.2017.06.120, 2017.

Wang, C., Wang, Z., Hui, F., and Zhang, X.: Speciated atmospheric mercury and sea–air exchange of gaseous mercury in the South China Sea, Atmos. Chem. Phys., 19, 10111–10127, https://doi.org/10.5194/acp-19-10111-2019, 2019.

Wang, Y., Chen, H. H., Tang, R., He, D., Lee, Z., Xue, H., Wells, M., Boss, E., and Chai, F.: Australian fire nourishes ocean phytoplankton bloom, Sci. Total Environ., 807, 150775, https://doi.org/10.1016/j.scitotenv.2021.150775, 2022.

Wängberg, I., Schmolke, S., Schager, P., Munthe, J., Ebinghaus, R., and Iverfeldt, Å.: Estimates of air–sea exchange of mercury in the Baltic Sea, Atmos. Environ., 35, 5477–5484, https://doi.org/10.1016/S1352-2310(01)00246-1, 2001.

Wanninkhof, R.: Relationship between wind speed and gas exchange over the ocean, J. Geophys. Res. Oceans, 97, 7373–7382, https://doi.org/10.1029/92JC00188, 1992.

Wanninkhof, R., and McGillis, W. R.: A cubic relationship between air–sea CO_2 exchange and wind speed, Geophys. Res. Lett., 26, 1889–1892, https://doi.org/10.1029/1999GL900363, 1999.

Weigelt, A., Ebinghaus, R., Manning, A. J., Derwent, R. G., Simmonds, P. G., Spain, T. G., Jennings, S. G., and Slemr, F.: Analysis and interpretation of 18 years of mercury observations since 1996 at Mace Head, Ireland, Atmos. Environ., 100, 85–93, https://doi.org/10.1016/j.atmosenv.2014.10.050, 2015.

Weigelt, A., Ebinghaus, R., Pirrone, N., Bieser, J., Bödewadt, J., Esposito, G., Slemr, F., van Velthoven, P. F., Zahn, A., and Ziereis, H.: Tropospheric mercury vertical profiles between 500 and 10 000 m in central Europe, Atmos. Chem. Phys., 16, 4135–4146, https://doi.org/10.5194/acp-16-4135-2016, 2016.

Weis, J., Schallenberg, C., Chase, Z., Bowie, A. R., Wojtasiewicz, B., Perron, M. M., Mallet, M. D., and Strutton, P. G.: Southern Ocean phytoplankton stimulated by wildfire emissions and sustained by iron recycling, Geophys. Res. Lett., 49(11), p.e2021GL097538, https://doi.org/10.1029/2021GL097538, 2022.

Wernand, M. R., van der Woerd, H. J., and Gieskes, W. W.: Trends in ocean colour and chlorophyll concentration from 1889 to 2000, worldwide. PLOS one, 8(6), e63766, https://doi.org.10.1088/1748-9326/ab4667, 2013.

Whalin, L., Kim, E. H., and Mason, R.: Factors influencing the oxidation, reduction, methylation and demethylation of mercury species in coastal waters, Mar. Chem., 107, 278–294, https://doi.org/10.1016/j.marchem.2007.04.002, 2007.

Wickham, H.: ggplot2: Elegant Graphics for Data Analysis, 2nd ed., Springer-Verlag New York, https://doi.org.10.21105/joss.01686, 2016.

Wickham, H., Averick, M., Bryan, J., Chang, W., McGowan, L. D. A., François, R., Grolemund, G., Hayes, A., Henry, L., Hester, J., and Kuhn, M.: Welcome to the Tidyverse, Journal of open source software, 4, 1686, https://doi.org/10.21105/joss.01686, 2019.

Ye, H., Chen, C., Sun, Z., Tang, S., Song, X., Yang, C., Tian, L., and Liu, F.: Estimation of the primary productivity in Pearl River Estuary using MODIS data, Estuaries and Coasts, 38, 506–518, https://doi.org/10.1007/s12237-014-9830-5, 2015.

Yin, X., Kang, S., de Foy, B., Ma, Y., Tong, Y., Zhang, W., Wang, X., Zhang, G., and Zhang, Q.: Multi-year monitoring of atmospheric total gaseous mercury at a remote high-altitude site (Nam Co, 4730 m asl) in the inland Tibetan Plateau region, Atmos. Chem. Phys., 18, 10557–10574, https://doi.org/10.5194/acp-18-10557-2018, 2018.

Xia, C., Xie, Z., and Sun, L.: Atmospheric mercury in the marine boundary layer along a cruise path from Shanghai, China to Prydz Bay, Antarctica, Atmos. Environ., 44, 1815–1821, https://doi.org/10.1016/j.atmosenv.2009.12.039, 2010.

El Yazidi, A., Ramonet, M., Ciais, P., Broquet, G., Pison, I., Abbaris, A., Brunner, D., Conil, S., Delmotte, M., Gheusi, F., and Guerin, F.: Identification of spikes associated with local sources in continuous time series of atmospheric CO, CO2 and CH4, Atmos. Meas. Tech., 11, 1599–1614, https://doi.org/10.5194/amt-11-1599-2018, 2018.

Yin, X., Kang, S., de Foy, B., Ma, Y., Tong, Y., Zhang, W., Wang, X., Zhang, G., and Zhang, Q.: Multi-year monitoring of atmospheric total gaseous mercury at a remote high-altitude site (Nam Co, 4730 m asl) in the inland Tibetan Plateau region, Atmos. Chem. Phys., 18, 10557–10574, https://doi.org/10.5194/acp-18-10557-2018, 2018.

Yu, S., Mathur, R., Kang, D., Schere, K., and Tong, D.: A study of the ozone formation by ensemble back trajectory-process analysis using the Eta–CMAQ forecast model over the northeastern US during the 2004 ICARTT period, Atmos. Environ., 43, 355–363, https://doi.org/10.1016/j.atmosenv.2008.09.079, 2009.

Zhang, Y., Jaeglé, L., Thompson, L., and Streets, D. G.: Six centuries of changing oceanic mercury, Global Biogeochem. Cy., 28, 1251–1261, https://doi.org/10.1002/2014GB004939, 2014.

Zhang, Y., Jacob, D. J., Horowitz, H. M., Chen, L., Amos, H. M., Krabbenhoft, D. P., Slemr, F., St. Louis, V. L., and Sunderland, E. M.: Observed decrease in atmospheric mercury explained by global decline in anthropogenic emissions, Proceedings of the National Academy of Sciences, 113, 526–531, https://doi.org/10.1073/pnas.1516312113, 2016.

Zhang, Y., Horowitz, H., Wang, J., Xie, Z., Kuss, J., and Soerensen, A. L.: A coupled global atmosphere-ocean model for air–sea exchange of mercury: insights into wet deposition and atmospheric redox chemistry, Environ. Sci. Technol., 53, 5052–5061, https://doi.org/10.1021/acs.est.8b06205, 2019.

Zhang, Y., Zhang, P., Song, Z., Huang, S., Yuan, T., Wu, P., Shah, V., Liu, M., Chen, L., Wang, X., and Zhou, J.: An updated global mercury budget from a coupled atmosphere-land-ocean model: 40% more re-emissions buffer the effect of primary emission reductions, One Earth, 6, 316–325, https://doi.org/10.1016/j.oneear.2023.02.004, 2023.

Zhou, J. and Obrist, D.: Global mercury assimilation by vegetation, Environ. Sci. Technol., 55, 14245–14257, https://doi.org/10.1021/acs.est.1c03530, 2021.

Zillioux, E. J.: Mercury in fish: history, sources, pathways, effects, and indicator usage, Environmental Indicators, 743–766, https://doi.org/10.1007/978-94-017-9499-2_42, 2015.

List of publications

This thesis comprises two individual scientific papers, one which has been accepted for publication (Chapter 3) and another which is in preparation for submission (Chapter 4):

Molepo, K. M., Bieser, J., Koenig, A. M., Hedgecock, I. M., Ebinghaus, R., Dommergue, A., Magand, O., Angot, H., Travnikov, O., Martin, L., Labuschagne, C., Read, K., and Bertrand, Y.: Constraining elemental mercury air–sea exchange using long-term ground-based observations, EGUsphere [preprint], https://doi.org/10.5194/egusphere-2024-3722, 2024.

Koketso M. Molepo, Ian M. Hedgecock, Alkuin M. Koenig, Francesco Carbone, Ralf Ebinghaus, Aurelien Dommergue: Constraining the influence of sea surface temperature and aquatic primary productivity on gaseous elemental mercury air–sea exchange using ground-based atmospheric observations. *In preparation for submission.*

Beyond my thesis work, the following papers were published during my doctoral studies:

Custódio, D., Pfaffhuber, K. A., Spain, T. G., Pankratov, F. F., Strigunova, I., **Molepo, K.**, Skov, H., Bieser, J., and Ebinghaus, R.: Odds and ends of atmospheric mercury in Europe and over the North Atlantic Ocean: temporal trends of 25 years of measurements, Atmos. Chem. Phys., 22, 3827–3840, https://doi.org/10.5194/acp-22-3827-2022, 2022.

Feinberg, A., Selin, N. E., Braban, C. F., Chang, K.-L., Custódio, D., Jaffe, D. A., Kyllönen, K., Landis, M. S., Leeson, S. R., **Molepo, K. M.**, Murovec, M., Mastromonaco, M. G. N., Pfaffhuber, K. A., Rüdiger, J., Sheu, G.-R., and St. Louis, V. L.: Unexpected anthropogenic emission decreases explain recent atmospheric mercury concentration declines, P. Natl. Acad. Sci. USA, 121, e2401950121, https://doi.org/10.1073/pnas.2401950121, 2024.

Acknowledgements

The number of people, organisations and structures that have made this Ph.D. possible is endless. I can only fill so many pages.

First, I would like to thank my academic supervisors Ralf Ebinghaus, Johannes Bieser, Ian Hedgecock and Aurélien Dommergue. Thank you for your patience with me, your guidance and support; for your immense knowledge and input that have helped shape this work; and for reading countless drafts of my "forever paper".

Thank you to my SICSS supervisory panel members Corinna Schrum and Nedjeljka Žagar, along with Ralf Ebinghaus, for your guidance, your encouragement and most importantly, for helping me set realistic goals. After our last meeting this past February, I started to see light at the end of this long tunnel. I am also grateful to the SICSS graduate school for making the supervisory panel structure possible, and to Berit Hachfeld at SICSS for constantly pushing me to have these crucial panel meetings.

My gratitude also goes out to my colleague and good friend Alkuin Koenig. Thank you for the willingness and enthusiasm you always showed in discussing my work; those "quick questions" that ended up being weeklong discussions over *WhatsApp*. I am also grateful that you introduced me to *dplyr*. What would analysing a million rows of data be without *dplyr*? I often joke that you were my fifth supervisor.

I am grateful to the many other great scientists that I had the pleasure of discussing and collaborating with during this Ph.D.: Oleg Travnikov, Jeroen Sonke, Hélène Angot, Olivier Magand, Danilo Custódio and Jenny Fisher. I hope our journey does not end here.

I am deeply thankful to my partner, Hendrik, and to friends in both South Africa and Germany, Peter, Déborah, Ndapewa, Dalena, Bellinda and Tumelo, who encouraged me, especially at times when I felt like giving up, but also reminded me that there is life beyond doing a Ph.D.

I am forever grateful to my wonderful parents, Tinny and Nkuoaneng Molepo, for always encouraging and supporting my dreams, no matter how unrealistic they seemed, no matter the cost. My mother always said to me, “Just go for it, we can figure out the logistics along the way”. And I did; I got on a plane in the middle of the COVID pandemic to pursue a Ph.D. across the globe, in a country I knew very little about. I am still figuring out the logistics but at least the Ph.D. part is (nearly) done. I am also grateful to my uncle Elleck Nchabeleng, who also encouraged my educational endeavours. Without such a supportive family, I would have never made it this far.

I am also thankful to Helmholtz-Zentrum Hereon and GMOS-Train for giving me this opportunity, and to the countless number of supportive colleagues at these groups. From Hereon, I would like to extend a special thank you to Doris Schnalke, for all the admin you put into my work trips (which I always organised at the last minute), and Christiane Hagemann, for guiding me through all the bureaucracy when I first arrived in Germany.

This research output would have not been possible without the scientists, engineers, data curators and funding agencies that made the data I used openly available. I thank the Irish Environmental Protection Agency, through their Climate Change Research Programme, for their support of the Hg measurement programme at Mace Head, and the Atmospheric Measurement and Observation Facility (AMOF), part of the UK’s National Centre for Atmospheric Science (NCAS), for supporting the Hg measurement programme at Cabo Verde Observatory. Thank you to the South African Weather Service (SAWS), the Global Mercury Observation System (GMOS; a European Community-funded FP7 project, ENV.2010.4.1.3-2) and the South African Department of Science and Innovation, as part of the SA Mercury Network (SAMNet), for supporting the Hg measurement programme at Cape Point. I also acknowledge Dr. Alastair Williams (ANSTO, Australia) for supporting the Radon measurement programme at Cape Point. I thank all overwintering staff at Amsterdam Island, as well as the staff and scientists from the French Polar Institute Paul-Emile Victor (IPEV), for their assistance with the setup and maintenance of the experiment at Amsterdam Island in the framework of the GMOStral-1028 IPEV program from 2012. Amsterdam Island atmospheric Hg data, accessible from the national GMOS-FR website data portal (https://gmos.aeris-data.fr/), were collected via instruments coordinated by the IGE-PTICHA technical platform dedicated to atmospheric chemistry field instrumentation. The GMOS-FR data portal is

maintained by the French national centre for Atmospheric data and services, AERIS (https://www.aeris-data.fr/), which is acknowledged by the authors. I would also like to acknowledge the contribution received from the following projects: Amsterdam Island Hg data, accessible in GMOS-FR national database (https://gmos.aeris-data.fr/), has been collected with funding from the European Union 7th Framework Programme project, GMOS (GMOS 2010-2015), the French Polar Institute (IPEV) via GMOStral-1028 IPEV program since 2012, the LEFE CHAT CNRS/INSU (TOPMMODEL program) and the H2020 ERA-PLANET (689443) iGOSP programme. The MODIS Chlorophyll-*a* concentrations and additional ocean color standard mapped image data, originally obtained from https://oceandata.sci.gsfc.nasa.gov, were provided with time axis and merged into one netCDF file per day / month by the Integrated sClimate Data Center (ICDC), CEN, University of Hamburg, Hamburg, Germany, https://www.cen.uni-hamburg.de/icdc. I am also grateful to the Irish Marine Institute, Met Éireann and the UK Met Office for their provision of the sea surface temperature (SST) through the Irish Marine Data Buoy Observation Network (IMDBON).

Finally, I wish to acknowledge the financial support that made this Ph.D. possible. My work, which was part of the GMOS-Train project that received funding from the European Union's Horizon 2020 research and innovation programme under Marie Skłodowska-Curie grant agreement no. 860497.